INFORMATION TO USERS

This manuscript has been reproduced from the microfilm master. UMI films the text directly from the original or copy submitted. Thus, some thesis and dissertation copies are in typewriter face, while others may be from any type of computer printer.

The quality of this reproduction is dependent upon the quality of the copy submitted. Broken or indistinct print, colored or poor quality illustrations and photographs, print bleedthrough, substandard margins, and improper alignment can adversely affect reproduction.

In the unlikely event that the author did not send UMI a complete manuscript and there are missing pages, these will be noted. Also, if unauthorized copyright material had to be removed, a note will indicate the deletion.

Oversize materials (e.g., maps, drawings, charts) are reproduced by sectioning the original, beginning at the upper left-hand corner and continuing from left to right in equal sections with small overlaps. Each original is also photographed in one exposure and is included in reduced form at the back of the book.

Photographs included in the original manuscript have been reproduced xerographically in this copy. Higher quality 6" x 9" black and white photographic prints are available for any photographs or illustrations appearing in this copy for an additional charge. Contact UMI directly to order.

University of Alberta

Vortex Dynamics at Free Surfaces

by

Bill James Peck   ©

A thesis submitted to the Faculty of Graduate Studies and Research in
partial fulfillment of the requirements for the degree of
Doctor of Philosophy.

Department of Mechanical Engineering

Edmonton, Alberta
Fall 1998

The author has granted a non-exclusive licence allowing the National Library of Canada to reproduce, loan, distribute or sell copies of this thesis in microform, paper or electronic formats.

The author retains ownership of the copyright in this thesis. Neither the thesis nor substantial extracts from it may be printed or otherwise reproduced without the author's permission.

L'auteur a accordé une licence non exclusive permettant à la Bibliothèque nationale du Canada de reproduire, prêter, distribuer ou vendre des copies de cette thèse sous la forme de microfiche/film, de reproduction sur papier ou sur format électronique.

L'auteur conserve la propriété du droit d'auteur qui protège cette thèse. Ni la thèse ni des extraits substantiels de celle-ci ne doivent être imprimés ou autrement reproduits sans son autorisation.

0-612-34820-2

Canada

University of Alberta

Library Release Form

Name of Author: Bill James Peck

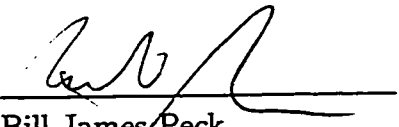Title of Thesis: Vortex Dynamics at Free Surfaces

Degree: Doctor of Philosophy

Year this Degree Granted: 1998

Bill James Peck
Wapoose Ranch
RR2 Innisfail, Alberta
Canada T0M 1A0

Oct 2, 1998

Will and consciousness are our vortex.

—H. Gaudier-Brzeska, 1914

University of Alberta

Faculty of Graduate Studies and Research

The undersigned certify that they have read, and recommend to the Faculty of Graduate Studies and Research for acceptance, a thesis entitled Vortex Dynamics at Free Surfaces submitted by Bill James Peck in partial fulfillment of the requirements for the degree of Doctor of Philosophy.

Dr. L. Sigurdson (Supervisor)

Dr. S. Green (External Examiner)

Dr. E. Lozowski

Dr. D. Steigmann (Via Teleconference)

Dr. A. W. Lipsett

Dr. A. Mioduchowski (Chairman and Examiner)

Date _Oct 2, 1998_

ABSTRACT

Vortex dynamics at fluid interfaces is discussed. Special emphasis is placed on the dynamics near a free surface.

The kinematics required at a free surface is discussed in detail. The level of vorticity required at the interface is calculated from the motion of the surface normal. Previous results restricted to special geometries are generalized and the role of the surface geometry is included.

Geometry effects on vorticity flux from a free surface is addressed. Contrary to previously published work these results show vortex lines may be straight and geometry-induced vorticity flux is produced; conversely vortex lines may be curved and no geometry-induced vorticity flux is produced. A convenient method for assessing vorticity flux from a steady surface based on Gaussian curvature is derived.

The vorticity transport equation is derived for a thin interface with variable density and viscosity. Viscosity gradients add several new terms to the vorticity transport equation. These new terms show vorticity is created not only by baroclinic torques but by torques due to viscosity gradients and a coupling of density gradients with viscosity gradients. These results are compared to those predicting the level of vorticity required at a free surface

discussed earlier.

Observations of vortex rings experimentally produced in two sets of experiments at a free surface are described.

The first set of experiments reports observations of vortex ring motion for the first 70 ms after it is created by the impact of a 2.6 mm dyed water drop upon a pool of clear water: Weber number (We) = 23.2. Precisely controlled multiple exposure photographs were used to measure the position and shape of the vortex ring versus time, and calculate velocity.

Refinements to the apparatus for producing repeatable drop-formed vortex rings are described. Control of parameters leading to reproducible experiments are addressed in detail.

Further experiments with this refined apparatus using 5.18 mm diameter drops with We ranging from 11.4 to 76 are reported. Detailed analysis of the falling drop using image processing techniques are described. Analysis of the vorticity creation process and vortex ring decay are compared with theoretical results.

Dedicated to the memory of Lloyd Graff

PREFACE

This is the second thesis I have written about drops impacting a pool of the same liquid. My first thesis was written for my masters degree; it examined the three-dimensional vortex structure created by a drop at short times after impact. This work was motivated by Professor Sigurdson's observation of similarities between a vortex structure created by an impacting water drop and the nuclear blast.

I began working on this problem with Professor Sigurdson in the summer of 1989 as an undergraduate summer student. Later I continued with my masters degree and first thesis on the subject. At the time, we believed the experiment would be a thrifty way to do research in the area of coherent structures in turbulence. My experience has shown that the experiment is far more complex than we initially thought. Experiments are frustrating and tedious, and the apparatus required was not as inexpensive as we originally hoped. Perseverance and stubbornness paid off with the present apparatus. It was sufficiently unique to have been published in the primary literature.

Our early research left us with many fundamental questions with no answers in the literature. First, how is the vorticity created when the drop coalesces with the pool ? This has been one of the central outstanding issues of our research. Professor Sigurdson raised this question at the 1989 American Physical Society meeting. Since that time a flurry of activity in the literature has addressed this question and the creation of vorticity at fluid interfaces in general. The current rush of papers on the subject reflects the relevance to current research. Unfortunately none of these papers presented a satisfactory explanation of how torques are applied to a fluid element. This area created a profound curiosity in myself and directed my education into the areas of continuum mechanics and elementary differential geometry. In Chapters 2 3 and 4 I feel I have answered this problem with a result which at least satisfies my own curiosity.

I used the *Chicago Manual of Style* as my primary reference for matters of style, although the bibliography was organized using the $\mathcal{AMS}$ conventions. The mathematics were set using the conventions given in the $\mathcal{AMS}$ documentation. The notation used is, wherever possible, consistent with that used by Chadwick (1976).

ACKNOWLEDGEMENT

CONTENTS

LIST OF FIGURES

LIST OF TABLES

LIST OF PLATES

Nomenclature

$\mathbf{e}_i$ . . . . Cartesian basis vectors in a spatial frame

$\mathbf{E}_i$ . . . . Cartesian basis vectors in a fixed reference frame

f . . . . Laser frequency

$\mathbf{F}$ . . . . Deformation tensor

Fr . . . . Froude number

$\mathbf{f}_{\mathscr{I}}$ . . . . Surface body forces

$\mathbf{g}$ . . . . Body force (gravity)

h_i . . . . Fall heights

$\mathbf{I}$ . . . . Hydrodynamic impulse

$\mathscr{H}$ . . . . Total head

$\mathbf{I}$ . . . . Hydrodynamic impulse, Identity tensor

J . . . . Jacobian

$\mathscr{M}$ . . . . Mass within a region

$\boldsymbol{\ell}$ . . . . Unit vector in direction of normal curvature

$\mathbf{L}$ . . . . Velocity gradient tensor

$\boldsymbol{n}$ . . . . Surface normal

p . . . . Pressure

$\mathbf{R}$ . . . . Rotation tensor

R . . . . Vortex ring radius

Re .... Reynolds number

S .... Intrinsic surface stress

$\mathbf{s}$.. Unit vector perpendicular to ℓ

$\mathbf{t}_{(n)}$ .... Surface traction

$\mathbf{t}_{(\mathscr{L})}$ .... Boundary curve surface traction

t_m .... Time to maximum crater penetration depth

$\boldsymbol{u}$ .... Velocity in a bulk region of fluid

$\mathbf{u_i}$ .... Surface unit vector in principal directions of b

$\mathbf{U}$.. Right stretching tensor

U_r.. Vortex ring velocity

$\boldsymbol{v}$ .... Velocity in a surface

$\mathbf{V}$.. Left stretching tensor

$\mathbf{W}$.. Rate-of-rotation tensor

We .... Weber number

$\mathscr{P}$.. A point

$\mathscr{C}$.. A curve or line

$\mathscr{S}$.. A surface

$\mathscr{R}$.. A region

w.. Laser beam width

$\bar{x}$ .... Area centroid of bitmap

x_a .... Depth of vortex rings leading edge

x_b .... Vortex ring depth

GREEK SYMBOLS

α .... Interior angle between viscosity gradient and principal direction of rate-of-strain

δ_t .... Lead time error

ε .... Core radius

ϵ_x .... Error in placement

η .... Coordinate normal to $\mathscr{S}$

Γ .... Circulation

$\Gamma^{\alpha}_{\gamma\beta}$ .... Surface Christöffel symbol

γ .... Surface tension

κ .... Curvature vector

κ_g .... Geodesic curvature

κ_n .... Normal curvature

κ_i .... Curvature in ith direction

κ_π .... Normal curvature on surface parallels

κ_μ .... Normal curvature on surface meridians

CHAPTER 1

INTRODUCTION

1.1 Background

This thesis is written in paper format and is divided into two parts. Each part contains three separate papers. In all, three of these papers have been published in the primary literature and one is in review. Two more are yet to be submitted. The status of each paper is noted at the start of each chapter.

This research was undertaken to understand the birth, evolution and decay of vortex structures produced by impacting water drops. If the drop fluid is dyed, and the drop is released from not too great a height, a vortex ring is formed and its evolution can easily be observed as it travels through the receiving pool.

The first observation of this phenomenon reported in the literature appears to be Ball (1868) and later Thomson and Newall (1885). These papers were published during a time of great advances in vortex dynamics and they reflect a profound interest in the then-developing field. Only ten years before Ball's work, Helmholtz published the seminal paper on vortex dynamics in his native German (Helmholtz, 1858); an English version appeared nine years later (Helmholtz, 1867). The importance of vortex rings to the scientists of this period is reflected in an added note to the English version of Helmholtz's paper. Here, the first appearance of the classic formula giving the speed of a vortex ring in an ideal fluid appears, Eq. (7.5) Chpt. 7. This result was calculated by Kelvin and included without derivation.

Early researchers believed vortex rings represented a fundamental quantity; this view was reflected in the vortex theory of the atom put forward by Thomson. More recently Maxworthy (1972) suggested that vortex rings may represent a fundamental structure within turbulence possibly being responsi-

ble for the sharp demarcation and growth of turbulent boundary layers with the external flow.

The evolution of vortex rings contains an entire range of topics from vortex dynamics. Vortex rings form when an axisymmetric vortex sheet 'rolls up' to form a circular line vortex. This line vortex is the vortex ring core. Instabilities may form on the vortex ring. These instabilities have been the subject of a great deal of attention in the literature. Finally, as Phillips (1956) showed, all flows decay to a Stokes flow of a vortex ring.

The early experimental works on drop-formed vortex rings mentioned earlier were limited, since they had no way of capturing a visual record of the phenomena other than hand-drawn sketches. Remarkably, the sketches in Thomson and Newall (1885) roughly show the complex evolution of the impacting drop into a vortex ring. This was subsequently verified by high-speed photography. Some of these sketches suggested that a complex structure forms at early times, from which a stable vortex ring emerges. High-speed photographs of this phenomena were published by Okabe and Inoue (1961). One of the photographs from this paper which appears in Batchelor (1967, Fig. 7.2.3 (1)) was to become the inspiration for Sigurdson's comparison of the atomic blast to the structure visible in the structure created by an impacting drop (Sigurdson, 1991).

Sigurdson suggested a similar large-scale vortex structure could be constructed to model both flows, despite the huge difference in Reynolds numbers. Here, the structure is modelled from a series of line-vortices, the dominant structure being a central vortex ring. In the larger view this reflects Sigurdson's pursuit of a 'periodic table of turbulence': a table of coherent turbulent structures, with which complex turbulent flows may be understood.

Constructing a vortex model of the structure created shortly after drop impact was the topic of my M.Sc. thesis (Peck, 1993) and (Peck and Sigurdson, 1991, 1992, 1994). While several new results were presented, several questions remained unanswered. The present work addresses outstanding fundamental questions raised in these works. New insights into observations not noticed before are also given.

Part I presents general analytical results on the creation of vorticity at free surfaces. A critical question was how vorticity was created by the coalescing drop. This is important not only for this specific problem of impacting drops but also for the general area of flows involving fluid interfaces. Knowing how vorticity enters a flow or is created within a region gives insight into the physics of the problem. For example, in a homogeneous, initially irrotational

flow, vorticity can only be created at the boundaries from which it then diffuses into the flow (Truesdell, 1954).

Part II presents experimental work on the specific case of an impacting drop.

Five appendices are included with this thesis. Appendix E includes several useful formulae used in many of the derivations in Part I.

The three chapters comprising Part I, Chapters 2, 3 and 4, discuss the creation of vorticity at a free surface in three different ways: the state of stress at a free surface, the Navier-Stokes equations and the vorticity equation. Each of these chapters are a self-contained journal paper that may be read individually. Useful results and comments on the notation used can be found in Appendix E.

The first two chapters of Part I view the interface as a singular surface (sharp interface) which possesses no thickness. Chpt. 2 looks at the level of vorticity required by the state of stress imposed by the free surface condition where the surface is assumed to be a sharp interface. The free surface condition is that tangential surface tractions are assumed to vanish and only a constant pressure is exerted on the interface. This work discovers new interpretations of the kinematics required to satisfy this boundary condition. The derivation is done from the most fundamental assumptions possible and worked through in its entirety. Although thought to be excessively verbose by some, paying extra attention to the details of this derivation yielded important new results previously overlooked in briefer analyses.

Chpt. 3 still uses a sharp interface model but now looks at the effect of the free surface condition and geometry on the flux of vorticity from the free surface using the momentum equation. Special attention is paid to situations where curvature-dependent contributions to the vorticity flux may be neglected. The topology of vortex lines embedded in the surface is discussed in this context. These results show that vortex lines may be straight and geometry-induced vorticity flux is produced; conversely vortex lines may be curved and no geometry-induced vorticity flux is produced. A convenient method for assessing vorticity flux from a steady surface based on Gaussian curvature is derived. There is significant redundancy between the introduction to Chpt. 3 and Chpt. 2, Sec. 3.3 may well be skipped by those familiar with results from Chpt. 2.

Creation of vorticity at fluid interfaces is discussed in the context of the vorticity transport equation in Chpt. 4. Here, an interface is modelled as a thin region across which density and viscosity vary rapidly but smoothly. Vis-

cosity gradients in this region add an extra term to the usual Navier-Stokes equation. Calculating the curl of this equation reveals curvature-dependent vorticity production terms. These new terms show vorticity is created not only by baroclinic torques but by torques due to viscosity gradients and a coupling of density gradients with viscosity gradients. These results are compared to those predicting the sign and level of vorticity required at a free surface discussed earlier.

The second part of this thesis Part II presents experimental results: Chpt. 5, Chpt. 6 and Chpt. 7.

Chpt. 5 presents experiments where a scaling law is proposed. Several measurements of the early-time vortex ring evolution were taken and compared with scaling arguments. The data presented here were acquired after completeing my M.Sc. and the scaling analysis was not addressed at all in my M.Sc.. This chapter respesents both new work when compared to my M.Sc. thesis and original inspiration in the scientific community. These experiments exposed several deficiencies in the apparatus which motivated the construction of a new apparatus.

Chpt. 6 describes the new apparatus in detail. Recently, several authors have suggested sophisticated optical measurement techniques such as Particle Image Velicometry (PIV) would be required to further understand the dynamics of impacting drops (Durst, 1996; Dooley et al., 1997). Before considering these expensive experiments, we chose to address the quality of the experiment itself rather than the sophistication of the measurement technique. We showed in Chpt. 6 that several parts of this experiment have gone overlooked even though they could be addressed with ingenuity and patience.

Experiments using this latest apparatus are reported in Chpt. 7. The experimental observations reported in this chapter were acquired using high-speed photography. A detailed record of the falling drop is recorded using image-processing techniques. The vorticity creation ideas developed in Chpt. 2 and Chpt. 4 were used to explain the creation of vorticity by drop impact and subsequent formation of vortex rings. Release heights were chosen to span the range of We where vortex rings were known to form. Also, a release height was examined outside of the range where vortex rings are known to form. Here early-time vorticity creation is observed and is contrasted with previous results.

A summary of the conclusions from the six chapters forming the body of this thesis appears in Chpt. 8.

Bibliography

Robert Ball. On vortex rings in air. *Philos. Mag.*, 36:12–14, 1868.

G. K. Batchelor. *An Introduction to Fluid Dynamics.* Cambridge University, New York, 1967.

B. S. Dooley, A. E. Warncke, M. Gharib, and G. Tryggvason. Vortex ring generation due to the coalescence of a water drop with a free surface. *Exp. in Fluids*, 22:369–374, 1997.

F. Durst. Penetration length and diameter development of vortex rings generated by impacting water drops. *Exp. in Fluids*, 21:110–117, 1996.

H. Helmholtz. Uber integrale der hydrodynamischen gleichungen welche den wirbelbewegungen entsprechen. *Crelles J.*, 55:25, 1858.

H. Helmholtz. On integrals of the hydrodynamical equations, which express vortex-motion. *Phil. Mag.*, 33(226):485–512, 1867.

T. Maxworthy. The structure and stability of vortex rings. *J. Fluid Mech.*, 51(part 1):15–32, 1972.

J. Okabe and S. Inoue. The generation of vortex rings, II. *Rept. Res. Inst. Appl. Mech.*, 9(36):147–161, 1961.

Bill Peck and Lorenz Sigurdson. Impacting water drop. *Phys. Fluids A*, 3 (9):2032, September 1991.

Bill Peck and Lorenz Sigurdson. Impacting water drops. *Phys. Fluids A*, 4 (9):1872, September 1992.

Bill Peck and Lorenz Sigurdson. The three-dimensional vortex structure of an impacting water drop. *Phys. Fluids*, 6(2):564–576, February 1994.

Bill J. Peck. The three-dimensional vortex structure of an impacting water drop. Master's thesis, University of Alberta, January 1993.

O. M. Phillips. The final period of decay of non-homogeneous turbulence. *Proc. Cambridge Phil. Soc.*, 52:135–151, 1956.

Lorenz Sigurdson. Atom Bomb/Water drop. *Phys. Fluids A*, 3(9):2034, September 1991.

J. J. Thomson and H. F. Newall. On the formation of vortex rings by drops falling into liquids, and some allied phenomena. *Proc. Roy. Soc. London Ser. A*, 39:417–436, 1885.

C. Truesdell. *The Kinematics of Vorticity*. Indiana University, Bloomington, Indiana, 1954.

PART I

ANALYSIS OF VORTEX MECHANICS AT FLUID INTERFACES

CHAPTER 2

ON THE KINEMATICS AT A FREE SURFACE† ·

2.1 Introduction

In this paper we describe the kinematics required to satisfy the dynamics of an interface where tangential surface tractions vanish. This assumption is often used to model air-water interfaces. If the air is assumed to only exert a constant pressure on the surface, the interface is called a free surface. Several papers have recently appeared which discuss the presence of vorticity required at free surfaces (Longuet-Higgins, 1992; Creswell and Morton, 1995; Rood, 1995; Wu, 1995; Sarpkaya, 1996). In these papers interpretation of the kinematics at the free surface are either restricted to simple geometries or left in very general tensor notation. In our work we will carefully examine and interpret the kinematics near the surface using results from differential geometry. Our results are especially relevant because of considerable recent research into complex three-dimensional flow interactions with free surfaces (Sarpkaya, 1996).

The vanishing tangential surface traction leads to equations that require one of the principal axes of rate-of-strain to be aligned with the surface normal n. Longuet-Higgins (1992) and, later, Sarpkaya (1996) interpret this boundary condition as a requirement for solid rotation of elements on the surface. In general, there is no requirement for this to be so whether the flow is two or three-dimensional, Sec. 2.2.1. However, the lack of tangential surface tractions does set the rotation rate, in the material sense, of the principal axis of rate-of-strain aligned with n. From this, the level of tangential vorticity that must be present at the surface can be calculated, Sec. 2.2.2.

---

†This chapter is the text of a paper accepted for publication in the IMA Journal of Applied Mathematics, (Peck and Sigurdson, 1998)

For two-dimensional plane-flow in a frame of reference that makes the surface stationary,

$$\omega = -2\kappa v_t, \tag{2.1}$$

where ω is the vorticity normal to the plane of the flow (Longuet-Higgins, 1953; Batchelor, 1967). The velocity component tangential to the plane curve $\mathscr{C}$ is v_t, where $\mathscr{C}$ is formed by the intersection of the flow's plane and the surface. When interpreting Eq. (2.1), κ has been referred to as merely the 'curvature', the normal curvature of the surface, or the curvature of the streamline on the surface. We will clarify these definitions and discuss the significance of the Gaussian and mean curvatures.

We use the convention that the curvature and the radius of curvature r have opposite signs so that $\kappa = -\frac{1}{r}$. If the surface normal at some point is chosen to be pointed upward, a surface which curves upward at that point will have positive curvature, Fig. 2.1.

In a recent paper by Wu (1995) the result

$$\omega = -2\kappa_m v_t \tag{2.2}$$

appears (Wu's Eq.(3)), where that paper defines the mean curvature κ_m to be the sum of the principal values of curvature. That paper claims this result is correct for steady, two-dimensional surfaces and later in the same paper qualifies this to only include two-dimensional flows. Although Eq. (2.2) is valid on surfaces of translation when the velocity is directed along the curve which generates the surface of translation, we will show it does not apply to general two-dimensional axisymmetric flows; Eq. (2.1) is correct for all two-dimensional flows where the surface is stationary.

We will extend Eq. (2.1) to include arbitrary two-dimensional surfaces and unsteady three-dimensional flows. In three-dimensional flow, components of vorticity not accounted for in Eq.(2.1) may exist which are directed along the streamline. We will show that vorticity must exist at a curved surface in a steady flow if the Gaussian curvature and tangential velocity are nonzero, Sec. 2.2.3. The discussion is concluded with brief comments on the use of streamline curvature, Sec. 2.2.4.
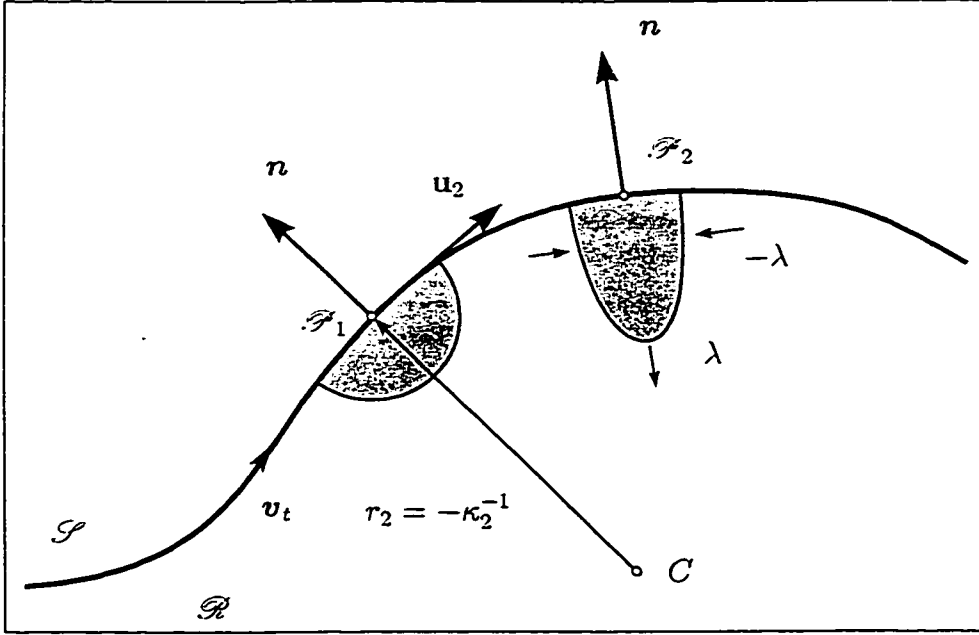
Figure 2.1: Deformation of an initially semi-circular fluid element in a two-dimensional plane flow near the free surface $\mathscr{S}$ of a region $\mathscr{R}$. Here it is understood that u_1 is directed out of the page. At $\mathscr{S}_1$ and $\mathscr{S}_2$ the surface is concave down and our sign convention gives negative curvature for an outwardly directed surface normal n.

2.2 Free surface kinematics

2.2.1 Jump conditions

The interface is modeled as a two-dimensional material surface $\mathscr{S}$ embedded in three-dimensional Euclidian space $\mathbb{R}^{31}$. Two regions of $\mathbb{R}^3$, $\mathscr{R}^+$ and $\mathscr{R}^-$ have $\mathscr{S}$ as their common boundary. The jump in surface tractions on $\mathscr{S}$ is given by

$$[\![t_{(n)}]\!] = -\rho_{\mathscr{S}}(\dot{v} - f_{\mathscr{S}}) + \mathrm{div}S, \qquad (2.3)$$

(Kosiński, 1986)[2]. Here, $t_{(n)} = \sigma n$ is the surface traction and $[\![\ ]\!]$ denotes the jump in a quantity on $\mathscr{S}$ with surface normal n. For fluids in $\mathscr{R}^+$

---

[1]For a discussion of the validity of this assumption see Meyer (1982)

[2]A complete derivation of jump conditions on $\mathscr{S}$ has been included in Appendix A

and $\mathscr{R}^-$, the Cauchy stress tensor σ is assumed to follow the Newtonian constitutive relation for an isochoric fluid: $\sigma = -p\mathbf{I} + 2\mu\mathbf{D}$. The identity tensor is denoted with $\mathbf{I}$, p is the pressure and μ is the dynamic viscosity. The symmetric, rate-of-strain tensor is represented by $\mathbf{D} = \frac{1}{2}(\mathbf{L} + \mathbf{L}^\mathsf{T})$, where $\mathbf{L} = \mathrm{grad}(u)$. We will use u to represent the velocity in the bulk regions and v to represent the velocity of particles embedded in the surface. v is a space vector and has components tangential and normal to $\mathscr{S}$: $v = v_t + vn$. The density of the surface per unit area is denoted $\rho_{\mathscr{S}}$; the surface body forces are $f_{\mathscr{S}}$. Eq. (2.3) also includes the effects of intrinsic surface stress S. In this paper we will only consider S to be the two-dimensional analogue of a stress in a three-dimensional ideal fluid. As such, S will be independent of surface rate-of-strain or dilation. In this case the constitutive relation for the surface stress is $S = \gamma a^\alpha \otimes a_\alpha$, a^α and a_α are the contravariant and covariant basis vectors on $\mathscr{S}$ (Scriven, 1960; Aris, 1962). Calculating the divergence, we obtain

$$\mathrm{div}S = 2H\gamma n + \mathrm{grad}_{\mathscr{S}}\gamma, \qquad (2.4)$$

where the mean curvature H is defined in Eq. (2.21a) and $\mathrm{grad}_{\mathscr{S}}$ is the surface gradient. The coefficient γ is the surface tension coefficient and is the two-dimensional equivalent of pressure in $\mathbb{R}^3$.

We resolve $\mathbf{t}_{(n)}$ into components tangential and normal to the surface:

$$\begin{aligned}
\mathbf{t}_{(n)} &= \mathbf{t}_{(n)} - (n \cdot \mathbf{t}_{(n)})n + (n \cdot \mathbf{t}_{(n)})n \\
&= \underbrace{(\mathbf{I} - n \otimes n)\sigma n}_{\text{tangential}} + \underbrace{(n \otimes n)\sigma n}_{\text{normal}}.
\end{aligned} \qquad (2.5)$$

Substituting Eq. (2.5), Eq. (2.4), and the constitutive relation into Eq. (2.3) we get two equations. For tangential components we have the vector valued equation

$$\begin{aligned}
\mathbf{D}^- n - [n \cdot (\mathbf{D}^- n)]n &= \frac{\mu^+}{\mu^-}\{\mathbf{D}^+ n - [n \cdot (\mathbf{D}^+ n)]n\} \\
&\quad - \frac{\rho_{\mathscr{S}}}{2\mu^-}[a^\alpha \cdot (\dot{v} - f_{\mathscr{S}})]a_\alpha \\
&\quad + \frac{1}{2\mu^-}\,\mathrm{grad}_{\mathscr{S}}\gamma.
\end{aligned} \qquad (2.6)$$

Superscripts $\{+, -\}$ have been affixed to represent the relevant quantities in $\mathscr{R}^+$ and $\mathscr{R}^-$. Equating the normally directed components we arrive at the

scalar valued equation

$$n \cdot \mathbf{D}^- n = \frac{p^- - p^+}{2\mu^-} + \frac{\mu^+}{\mu^-} n \cdot \mathbf{D}^+ n$$

$$+ \frac{\rho_{\mathscr{S}}}{2\mu^-}[n \cdot (\dot{v} - \mathbf{f}_{\mathscr{S}})] \qquad (2.7)$$

$$+ \frac{H\gamma}{\mu^-}.$$

We introduce the nondimensionlization:

$$\tilde{\mathbf{D}} \sim \frac{\mathbf{D}}{(U/L)}$$

$$\tilde{p} \sim \frac{p}{(\rho^- U^2)}$$

$$\tilde{\dot{v}} \sim \frac{\dot{v}}{(U^2 L)}$$

$$\tilde{H} \sim HL^2, \qquad (2.8)$$

where the tilde denotes a nondimensional variable. L is a characteristic length scale and U is a characteristic velocity. We have assumed p^+ is constant. In nondimensional form Eq. (2.6) becomes

$$\tilde{\mathbf{D}}^- n - [n \cdot (\tilde{\mathbf{D}}^- n)]n = \left(\frac{\mu^+}{\mu^-}\right) \{\tilde{\mathbf{D}}^+ n - [n \cdot (\tilde{\mathbf{D}}^+ n)]n\}$$

$$- \left(\frac{\rho_{\mathscr{S}} U}{\mu^-}\right) \frac{[\mathbf{a}^\alpha \cdot (\tilde{\dot{v}} - \mathbf{f}_{\mathscr{S}})]\mathbf{a}_\alpha}{2} \qquad (2.9)$$

$$+ \left(\frac{\gamma}{L\mu^-}\right) \frac{\widetilde{\mathrm{grad}_{\mathscr{S}}\gamma}}{2},$$

and Eq. (2.7) is now

$$n \cdot \tilde{\mathbf{D}}^- n = \left(\frac{\rho^- UL}{\mu}\right) \frac{\widetilde{p^- - p^+}}{2} + \left(\frac{\mu^+}{\mu^-}\right) n \cdot \tilde{\mathbf{D}}^+ n$$

$$+ \left(\frac{\rho_{\mathscr{S}} U}{\mu^-}\right) \frac{[n \cdot (\tilde{\dot{v}}) - \mathbf{f}_{\mathscr{S}}]}{2} \qquad (2.10)$$

$$+ \left(\frac{\gamma}{UL\mu^-}\right) \tilde{H}.$$

If $\mu^+ \ll \mu^-$ the contributions from the rate-of-strain terms in $\mathscr{R}^+$ — the second term on the right of Eq. (2.10) — are neglected. If $\rho_y U/\mu^-$ is assumed to be small, contributions from the second term on the right of Eq. (2.9) are neglected. Also, at present, we will assume that no surface tension gradients are present which may arise due to thermal gradients, contamination or dynamical means. We will return to examine the effects of surface tension gradients later in the text. With these assumptions Eq. (2.6) becomes

$$(\tilde{D} - \lambda I)n = 0, \qquad (2.11)$$

where $\lambda = n \cdot (\tilde{D}n)$ (the superscripts have been dropped since we will only be concerned with $\mathscr{R}^-$). This means λ is a principal value of the rate-of-strain and is directed along n. The value of λ is calculated from Eq. (2.7). With our supposition of vanishing viscosity in $\mathscr{R}^+$, $\lambda = Re\,\widetilde{\Delta p}/2\mu + \frac{1}{UL\mu^-}\tilde{H}$, where $\widetilde{\Delta p}$ is the jump in pressure across the interface and $Re = \frac{\rho^- UL}{\mu}$. The other two principal axes of strain will lie in the surface tangent plane.

From this discussion we see that the jump condition Eq. (2.3) and the assumptions which lead to Eq. (2.11) requires one principal axis of rate-of-strain to be aligned with n. This does not imply that the motion of fluid elements at the surface is locally solid. Longuet-Higgins (1992) suggested fluid elements at the free surface of purely two-dimensional plane flow were in solid rotation . For a solid rotation, $\tilde{D} = 0$. However, Eq. (2.11) shows that an element is free to deform along an axis, which will be a principal axis of rate-of-strain, aligned with n at a rate λ, Fig. 2.1 . In two-dimensional flow, the principal axes of strain will remain in the plane and orthogonal; one axis normal to the surface and one tangential. $\tilde{D}$ takes the form $\tilde{D} = -\lambda u_2 \otimes u_2 + \lambda n \otimes n$ due to the continuity restriction for an isochoric fluid $\text{div}\,\tilde{u} = \text{tr}(\tilde{L}) = \text{tr}(\tilde{D}) = D_{22} + D_{33} = 0$ where $D_{33} = \lambda$. Here we have assigned the subscript 2 with reference to the unit vector u_2 and the subscript 3 to n. Thus, even in a purely two-dimensional flow, fluid elements at the surface will not be in solid rotation unless the rate-of-strain directed along the surface normal is zero. Longuet-Higgins observation that the tangential shears vanish only assures us that off diagonal terms of $\tilde{D}$ are zero and the direction of one principal axes of rate-of-strain will remain aligned with n. Thus, the other principal axis of rate-of-strain will remain tangent to the surface. We can say the direction of the axes themselves will be in a state of continuous solid rotation – not necessarily the fluid element however. We note that while Longuet-Higgins' physical interpretation was misleading it

does not affect any of the calculations in that paper.

In three-dimensional flows, there may be components of vorticity normal to the surface. Also, there are no restrictions on the deformation of an element along the principal axes of rate-of-strain in the tangent plane. A solid rotation $D = 0$ would imply that any vorticity intensification due to stretching of vortex lines would vanished as the vortex-lines approach the surface. This is clearly not so.

2.2.2 Vorticity

To calculate the vorticity, we use the decomposition $L = D + W$, where $W = \frac{1}{2}(L - L^T)$ is the spin tensor. We solve for D and substitute into Eq. (2.11):

$$Ln - Wn - n \cdot (Ln)n + n \cdot Wn = 0. \tag{2.12}$$

Adding and subtracting $L^T n$ to Eq. (2.12) gives the convenient form

$$\underbrace{Ln - L^T n}_{2Wn} - Wn + \underbrace{L^T n - [n \cdot (Ln)]n}_{-\dot{n}} = 0. \tag{2.13}$$

Now, the material derivative of the surface normal $\dot{n}$ appears. We refer the reader to Appendix B for a derivation of $\dot{n}$ (Chadwick, 1976). Since W is skew-symmetric $Wn = \frac{\omega}{2} \times n$. Eq. (2.13) is rewritten

$$\omega \times n = 2\dot{n}. \tag{2.14}$$

Crossing Eq. (2.14) with n gives the expression for the vorticity:

$$\underbrace{\omega - (n \cdot \omega)n}_{\omega_t} = 2n \times \dot{n}. \tag{2.15}$$

The left side of Eq. (2.15) is the tangential component of vorticity ω_t. The right represents the surface normal's angular velocity.

We can interpret these equations in terms of the Cauchy-Stokes decomposition, where a fluid motion is described as a translation, a deformation along three mutually orthogonal axes and a rotation of these axes (Aris, 1962). In our case the translation of a fluid element will be constrained by the material nature of the interface so that particles of the element in contact with the surface will remain so. From Eq. (2.11) we know that one of the principal

axes of deformation will remain aligned with the surface normal. The rate-of-rotation of this axis is given by Eq. (2.15); thus, the tangential vorticity is given by twice the angular velocity of n. Likewise, the normal vorticity would be given by twice the instantaneous rate of rotation of the principal axes of strain which must necessarily lie in the tangent plane. This is an example of the elegant interpretation of vorticity attributed to Boussinesq by Truesdell (1954), which is, that vorticity is twice the instantaneous rate of rotation of the principal axes of strain; see Appendix C for details.

The curvature-independent surface gradient term may need to be included in Eq. (2.6) if the surface tension gradients are of similar magnitude to the bulk dynamic viscosity. The vorticity becomes

$$\omega_t = 2n \times \dot{n} + \frac{1}{\mu} n \times \text{grad}_{\mathscr{S}} \gamma, \tag{2.16}$$

so that even when $\dot{n} = 0$ a gradient in surface tension will require the presence of vorticity (Brøns, 1994; Tryggvason et al., 1992). The presence of a surface tension gradient invalidates Eq. (2.11) and we can no longer calculate the vorticity from the rotation rate of the surface normal.

2.2.3 Geometric interpretation

To interpret Eq. (2.15) in terms of the surface geometry, we use an expression for $\dot{n}$ in terms of surface coordinates (a^α, n):

$$\dot{n} = -\text{grad}_{\mathscr{S}} v - b_\alpha^\beta v_\beta a^\alpha = -\text{grad}_{\mathscr{S}} v - \mathbf{b} v_t, \tag{2.17}$$

where a^α are the contravariant basis vectors and v_β are the covariant components of the tangential velocity v_t. For this derivation, we refer the reader to Naghdi (1972) and Kosiński (1986). In Eq. (2.17)) $\text{grad}_{\mathscr{S}} v$ is the surface gradient of the normal velocity v, b_α^β are the mixed components of the curvature tensor $\mathbf{b}$. Also, Greek indices take the value $\{1, 2\}$ and summation on repeated indices is implied. The curvature tensor is related to the surface normal:

$$\text{grad}(n) = n_{,\alpha} \otimes a^\alpha = -b_\alpha^\beta a_\beta \otimes a^\alpha = -\mathbf{b}, \tag{2.18}$$

where we have used Weingarten's equation $n_{,\alpha} = -b_\alpha^\beta a_\beta$. The curvature tensor is a symmetric surface tensor which ensures the existence of two extremal - values. The extremal values are the maximum and minimum values of the
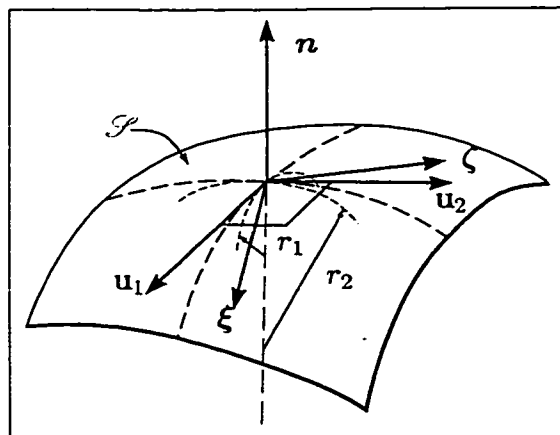
Figure 2.2: Definition sketch of the surface coordinates on $\mathscr{S}$

normal curvatures at a point. These are the principal values of curvature $\kappa_1 = -\frac{1}{r_1}$ and $\kappa_2 = -\frac{1}{r_2}$. The planes which contain these curvatures are orthogonal. The unit vectors $\mathbf{u}_1$, $\mathbf{u}_2$ are aligned with the planes containing the principal values of curvature and, with n, form an orthonormal basis, Fig. 2.2. These are called lines-of-curvature coordinates. In these coordinates,

$$\mathbf{b} = \kappa_1 \mathbf{u}_1 \otimes \mathbf{u}_1 + \kappa_2 \mathbf{u}_2 \otimes \mathbf{u}_2. \tag{2.19}$$

We may choose another orthonormal basis $(\boldsymbol{\xi}, \boldsymbol{\zeta}, \boldsymbol{n})$ such that $\boldsymbol{\xi} \times \boldsymbol{\zeta} = \boldsymbol{n}$. Off-diagonal terms appear in $\mathbf{b}$ if the unit vectors $\boldsymbol{\xi}, \boldsymbol{\zeta}$ are not aligned with the principal axes of curvature. The off-diagonal terms represent the surface twist τ. In this case Eq. (2.19) becomes

$$\mathbf{b} = \kappa_\xi \boldsymbol{\xi} \otimes \boldsymbol{\xi} + \kappa_\zeta \boldsymbol{\zeta} \otimes \boldsymbol{\zeta} + \tau(\boldsymbol{\xi} \otimes \boldsymbol{\zeta} + \boldsymbol{\zeta} \otimes \boldsymbol{\xi}), \tag{2.20}$$

where κ_ζ and κ_ξ are the normal curvatures in the $\boldsymbol{\zeta}$ and $\boldsymbol{\xi}$ planes. If the surface is locally umbilic—locally spherical or planar—the principal directions of $\mathbf{b}$ are not unique and $\tau = 0$ in all directions.

We note two scalar measures of a surface's curvature. The mean curvature H which is the arithmetic mean of κ_1 and κ_2, and the Gaussian curvature K

which is their product:

$$2H = \text{div}(n) = \text{tr}[\text{grad}(n)] = \kappa_1 + \kappa_2 = \kappa_\zeta + \kappa_\xi, \qquad (2.21a)$$

$$K = \det(\mathbf{b}) = \kappa_1\kappa_2 = \kappa_\zeta\kappa_\xi - \tau^2. \qquad (2.21b)$$

Substituting Eq. (2.20) into Eq. (2.17), we obtain

$$\dot{n} = -\text{grad}_{\mathscr{S}}v - \kappa_\zeta v_{<\zeta>}(\zeta \cdot \zeta)\zeta - \kappa_\xi v_{<\xi>}(\xi \cdot \xi)\xi$$
$$- \tau v_{<\zeta>}(\zeta \cdot \zeta)\xi - \tau v_{<\xi>}(\xi \cdot \xi)\zeta. \qquad (2.22)$$

Using Eq. (2.22) in Eq. (2.15), we get the general expression for ω_t at an unsteady free surface:

$$\omega_t = 2\,\text{grad}_{\mathscr{S}}v \times n + 2\mathbf{b}v_t \times n \qquad (2.23a)$$

$$= 2\,\text{grad}_{\mathscr{S}}v \times n + 2(\kappa_\zeta v_{<\zeta>} + \tau v_{<\xi>})\xi - 2(\kappa_\xi v_{<\xi>} + \tau v_{<\zeta>})\zeta. \qquad (2.23b)$$

Here the twist of the surface now contributes to the vorticity. We have not seen the terms involving τ in the literature before. In lines-of-curvature components, Eq. (2.23a) becomes

$$\omega_t = 2\,\text{grad}_{\mathscr{S}}v \times n + 2(\kappa_2 v_{<2>})\mathbf{u}_1 - 2(\kappa_1 v_{<1>})\mathbf{u}_2. \qquad (2.24)$$

It is important to note that since the coordinate systems used in Eq. (2.23b) and Eq. (2.24) are both orthonormal bases, the velocity components in both equations are physical components which are denoted with angle braces, $<>$. These are values which could actually be measured in experiments. These are not to be confused with contravariant or covariant components which may not even have the same physical dimension as their physical counterparts.

Eq. (2.23) shows that ω_t is made of two components: (1) local rotation of the surface in three-dimensional space given by $2\,\text{grad}_{\mathscr{S}}v \times n$, (2) rotation of the fluid element as it traverses regions of normal curvature and surface twist represented by $2(\kappa_\zeta v_{<\zeta>} + \tau v_{<\xi>})\xi$ and $2(\kappa_\xi v_{<\xi>} + \tau v_{<\zeta>})\zeta$. The terms containing τ represent the rotation of the principal axis of strain aligned with n as the tangent plane rotates about the axis directed along the path of travel. If the reference basis falls on the principal directions of curvature, $\tau = 0$ and the vorticity is given by the tangential velocities and principal curvatures alone.

As a simple example, we consider a flow on a steady surface where the local fluid velocity q is directed along ξ so that $v_{<\xi>} = q$. In such a case, we

may wish to know the components of vorticity in terms of components along u_1, u_2 or components along ξ, ζ. For the first case, we simply rewrite $v_{<1>}$ and $v_{<2>}$ in terms of q and the angle α between u_1 and ξ:

$$v_{<1>} = q\cos(\alpha)$$
$$v_{<2>} = q\sin(\alpha). \tag{2.25}$$

Substituting Eq. (2.25) into Eq. (2.24) gives

$$\omega_t = 2q(\kappa_2 \sin \alpha u_1 - \kappa_1 \cos \alpha u_2). \tag{2.26}$$

The vorticity components in terms of ξ, ζ can also be expressed using the principal curvatures and α. After substituting q for $v_{<\xi>}$ in Eq. (2.23b) we are left with,

$$\omega_t = -2\kappa_\xi q\zeta + 2\tau q\xi. \tag{2.27}$$

Expressions for $\kappa_{<\xi>}$ and τ in terms of κ_1, κ_2 and α can be calculated as follows. Using Euler's theorem ((Kreyszig, 1991), p. 132) $\kappa_{<\xi>}$ can be written as:

$$\kappa_\xi = \kappa_1 \cos^2 \alpha + \kappa_2 \sin^2 \alpha. \tag{2.28}$$

From Eq. (2.21a), the invariance of H requires

$$\kappa_\zeta = \kappa_1 \sin^2 \alpha + \kappa_2 \cos^2 \alpha. \tag{2.29}$$

The invariance of K is invoked to obtain an expression for τ. Substituting Eq. (2.28) and Eq. (2.29) into Eq. (2.21b) and solving for τ gives

$$\tau^2 = (\kappa_1 - \kappa_2)^2 \cos^2 \alpha \sin^2 \alpha. \tag{2.30}$$

In view of our sign convention, we choose the negative root of τ:

$$\tau = (\kappa_2 - \kappa_1)\sin\alpha\cos\alpha = \frac{(\kappa_2 - \kappa_1)}{2}\sin(2\alpha). \tag{2.31}$$

Substituting these results into Eq. (2.27) gives

$$\omega_t = -2q(\kappa_2 \cos^2 \alpha + \kappa_1 \sin^2 \alpha)\zeta + q(\kappa_2 - \kappa_1)\sin(2\alpha)\xi. \tag{2.32}$$

The component of vorticity directed along ζ represents the vorticity due to normal curvature while that directed along ξ is due to the surface twist. The surface twist vanishes along the principal directions $\alpha = 0, \frac{\pi}{2}$. Eq. (2.32) nicely demonstrates how τ vanishes at umbilic points. At such a point, $\kappa_1 = \kappa_2$, and the last term of Eq. (2.32) is zero. This is expected since b has no distinct principal directions at umbilics and $\tau = 0$ for all orientations.

To illustrate the geometry of the deformation near a free surface we consider the surface given by the hyperbolic paraboloid in Fig. 2.3. The lower half of the figure is assumed to be filled with the bulk fluid. If an initially hemispherical fluid element at $\mathscr{P}_1$ travels along $\mathscr{C}_1$ the vorticity will be given by the normal curvature alone since $\mathscr{C}_1$ is a line-of-curvature. If the element moves from $\mathscr{P}_1$ along $\mathscr{C}_3$ – a rule of $\mathscr{S}$, so there is no normal curvature – the vorticity will be given by the surface twist alone. This component of vorticity will be directed along $\mathscr{C}_3$.

We can now show that a steady surface may have normal curvature with $\omega_t = 0$. On a steady surface there will be no local rotation and the first term on the right of Eq. (2.23a) is zero. If we assume the vorticity is zero Eq. (2.23a) becomes

$$\mathbf{b}v_t = 0, \tag{2.33}$$

since $\mathbf{b}v_t$ is a surface vector. For a nonzero v_t, we must have $\det(\mathbf{b}) = K = 0$ to satisfy Eq. (2.33). Thus, for no vorticity at the interface, the Gaussian curvature must vanish which implies at least one of the principal curvatures must vanish. Such surfaces are referred to as developable. If both principal curvatures vanish the surface is locally planar and v_t can take on any value. If only one principal curvature is zero, say κ_1, and the velocity is directed along $\mathbf{u}_1$, the vorticity will be zero but the surface will be curved. If we choose an orthonormal basis not aligned with the lines-of-curvature basis the terms containing the normal curvature and surface twist will sum to zero for each component of vorticity; $\kappa_\zeta v_{<\zeta>} + \tau v_{<\xi>} = 0$ and $\kappa_\xi v_{<\xi>} + \tau v_{<\zeta>} = 0$.

In Longuet-Higgins (1992) we find the statement and theorem: "any curved surface in a steady flow, irrotational or not, is necessarily a source of vorticity". These results were derived in Longuet-Higgins for two-dimensional plane flow bounded by a free surface. We only need to slightly modify this result and theorem to cover general three-dimensional cases. Longuet-Higgins' statement is always true if $K \neq 0$. If $K = 0$, a special case can exist where
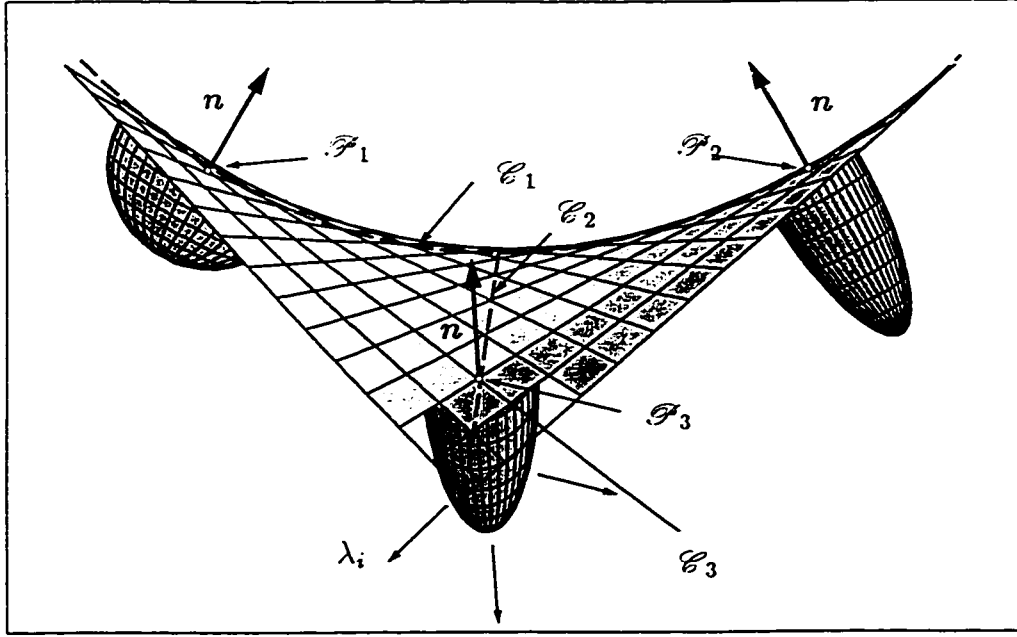
Figure 2.3: The deformation of an initially hemispherical element at $\mathscr{F}_1$. The curves $\mathscr{C}_1$ and $\mathscr{C}_2$ are lines-of-curvature. Fluid elements traveling along these curves have their vorticity determined by the normal curvatures alone. The unbroken lines on $\mathscr{S}$ including $\mathscr{C}_3$ are rules of the hyperbolic paraboloid and have no normal curvature. The vorticity of fluid elements traveling along $\mathscr{C}_3$ is given by the surface twist and directed along the path of travel. λ_i are the principal stretches at $\mathscr{F}_3$, one of which must be directed along the surface normal.

the velocity is in the direction of the zero-valued principal curvature. In this case, a zero value of vorticity is required on the surface although the surface is still curved.

Wu (1995) states that Eq. (2.2) is valid for stationary two-dimensional surfaces. This can include all surfaces embedded in three-dimensional space which means that any steady three-dimensional flow would be admissible. From Eq. (2.24) we see that the normal curvatures determine the vorticity; the mean curvature has no direct influence on the vorticity. Later in the same paper, the applicability of Eq. (2.2) is limited to two-dimensional flow. This limits the bounding surfaces to either surfaces of revolution or surfaces
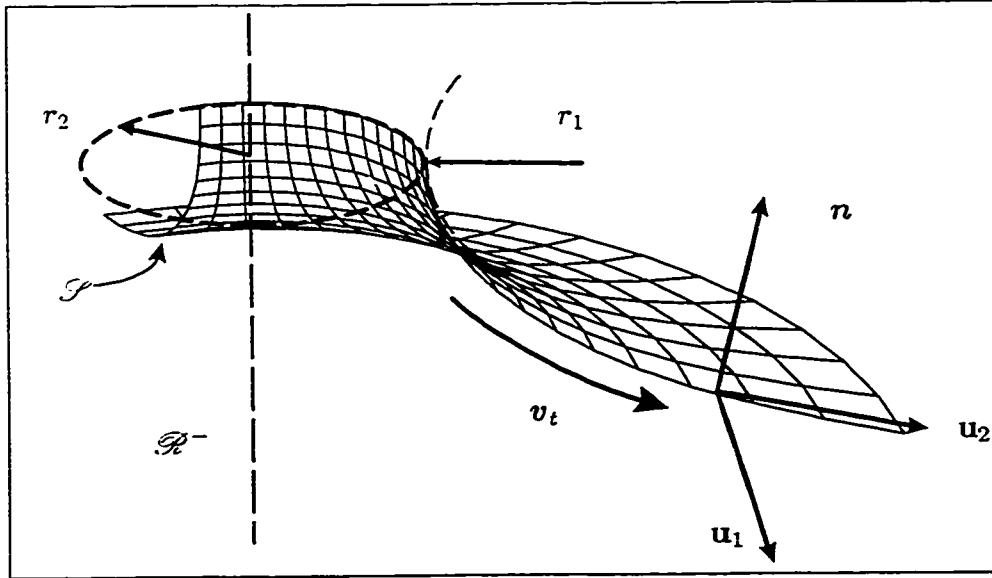
Figure 2.4: A surface which is locally a catenoid. The catenoid is a minimal surface defined by $H = 0$.

of translation – both are one-dimensional. Since the flow is two-dimensional the plane of the flow will contain a principal value of curvature. The only situation which satisfies Eq. (2.2) is two-dimensional flow bounded by a surface of translation.

Eq. (2.2) is not correct for general two-dimensional axisymmetric flows (although the correct calculation must have been done to obtain Eq. 81 in Wu (1995) for a spherical bubble). An example is flow on a locally minimal surface such as a catenoid (Kreyszig, 1991). A minimal surface is defined by $H = 0$ implying $\kappa_1 = -\kappa_2$, (see Fig. 2.4). The velocity is assumed to be directed along the meridians of the catenoid and $\mathscr{R}^-$ contains the axis of symmetry. In this case Eq. (2.2) predicts the vorticity to be zero although the correct value is $\omega_{<1>} = 2\kappa_2 v_{<2>}$.

The only axisymmetric geometry which satisfies Eq. (2.2) is a locally cylindrical surface if v_t is in the plane of the cylinder's radius R so that $\omega = 2v_t/R$. This can also be viewed as a surface of translation. If the flow is directed along the axis of the cylinder with the same velocity Eq. (2.2) would still predict the same value for the vorticity. The correct value is zero. This also serves as an example of a steady flow which requires zero vorticity at

a curved surface. In general, the mean curvature has no direct relationship with the vorticity because it is a scalar that has no direction associated with it. The normal curvatures and surface twist are assigned directions through b.

Eq. (2.24) and Eq. (2.23) have consequences for experiments. To measure vorticity at a surface we don't need to know the tangential velocity's gradients. We do need to know the angular velocity of the surface normal affixed to a certain particle, the particle's velocity and the surface geometry.

2.2.4 Streamline curvature

We must be careful when interpreting Eq. (2.1) in terms of streamline curvature. If a streamline follows a curve $\mathscr{C}$ embedded in $\mathscr{S}$ we may define a curvature vector along the streamline $\kappa = \kappa_n \ell + \kappa_g s$ where κ_n is the normal curvature of $\mathscr{S}$ in the direction of the unit vector ℓ directed along $\mathscr{C}$. The geodesic curvature κ_g is directed along s which is normal to ℓ and in the tangent plane of $\mathscr{S}$. Thus, in general, the vorticity normal to the direction of flow is only given by the streamline curvature if κ_g vanishes. If this is the case $\mathscr{C}$ is a geodesic curve and κ in Eq. (2.1) corresponds to the streamline curvature.

Most examples in the literature are steady, two-dimensional flows with the flow restricted to a plane. The plane of the flow intersects the free surface $\mathscr{S}$ normally. The bounding streamline follows a curve formed by the intersection of the flow's plane and $\mathscr{S}$. In these cases, the bounding streamline lies on a geodesic of $\mathscr{S}$; therefore, the streamline curvature and normal curvature are the same. For example, consider axisymmetric flow bounded by a surface of revolution. Here, streamlines either follow meridians or parallels of the surface which are geodesics.

Circular streamlines on plane surfaces are examples of curves which have only geodesic curvature. In this case, the flow is still in a two-dimensional plane, but the flow's plane coincides with $\mathscr{S}$. Using streamline curvature in Eq. (2.1) would predict an incorrect nonzero value.

2.3   Conclusions

The results discussed in this paper only tell us what level of vorticity must be present to satisfy the dynamics imposed by the continuous surface tractions. They do not tell us how the local torques are applied to fluid elements. These

results are valid for any interface between immiscible fluids with disparate dynamic viscosities. Thus, the surface tractions at an interface between two fluids with equal densities and different viscosities must satisfy Eq.(2.3) also. Since the density is constant there are no baroclinic torques and the torques will be applied by viscous forces. We will be addressing this issue in a forthcoming paper which is presently the body of Chpt. 4.

Bibliography

Rutherford Aris. *Vectors, Tensors and the Basic Equations of Fluid Mechanics.* Prentice-Hall, Englewood Cliffs, New Jersey, 1962.

G. K. Batchelor. *An Introduction to Fluid Dynamics.* Cambridge University, New York, 1967.

M. Brøns. Topological fluid dynamics of interfacial flows. *Phys. Fluids*, 6: 2730–2737, 1994.

P. Chadwick. *Continuum Mechanics.* John Wiley and Sons, New York, 1976.

R. W. Creswell and B. R. Morton. Drop-formed vortex rings–the generation of vorticity. *Phys. Fluids*, 7(6):1363–1370, June 1995.

W Kosiński. *Field Singularities and Wave Analysis in Continuum Mechanics.* John Wiley and Sons, New York, 1986.

Erwin Kreyszig. *Differential Geometry.* Dover, New York, 1991.

Michael S. Longuet-Higgins. Capillary rollers and bores. *J. Fluid Mech.*, 240: 659–679, 1992.

M.S. Longuet-Higgins. Mass transport in water waves. *Proc. Roy. Soc. London Ser. A*, 245:535–581, March 1953.

Richard E. Meyer. *Introduction to Mathematical Fluid Dynamics.* Dover, 1982.

P. M. Naghdi. *S. Flugge's Handbuch der Physik*, volume VIa/2, chapter The theory of plates and shells, pages 425–640. Springer, Berlin, 1972.

Bill Peck and Lorenz Sigurdson. On the kinematics at a free surface. *IMA J. of Appl. Math.*, 60:1–13, 1998.

Edwin P. Rood. *Fluid Vorticies*, chapter Vorticity Interactions with a Free-Surface. Kluwer Academic, 1995.

Turgut Sarpkaya. Vorticity, free-surface and surfactants. *Annu. Rev. Fluid Mech.*, 28:83–128, 1996.

L. E. Scriven. Dynamics of a fluid interface. *Chem Engrg. Sci.*, 12:98–108, 1960.

C. Truesdell. *The Kinematics of Vorticity*. Indiana University, Bloomington, Indiana, 1954.

Grétar Tryggvason, Javad Abdollahi-Ailbeik, William W. Willmarth, and Amir Hirsa. Collision of a vortex pair with a contaminated free-surface. *Phys. Fluids*, 4(6):1215–1229, June 1992.

Jie-Zhi Wu. A theory of three-dimensional interfacial vorticity. *Phys. Fluids*, 7(10):2375–2395, October 1995.

Chapter 3

Geometry Effects on Free Surface Vorticity Flux †

3.1 Introduction

This paper discusses effects of complex surface geometries on vorticity flux Φ from an arbitrary two-dimensional free surface embedded in three-dimensional Euclidian space $\mathbb{R}^3$. Most previous analyses of free surface vorticity flux have been restricted to one-dimensional surfaces. By one-dimensional we mean surfaces which vary in only one parameter. Examples are the free surfaces of plane waves and axisymmetric flows such as rising bubbles. Recent advances in experimental techniques have allowed analysis of complicated two-dimensional surface geometries Dabiri (1997). In these experiments, complete understanding of geometric effects are essential for correct interpretation of vorticity levels at free surfaces and vorticity flux from free surfaces.

The idea of a vorticity flux was introduced by Lighthill (1963) to describe introduction of vorticity into a bulk fluid from rigid boundaries. Here, diffusion of linear momentum was written in terms of vorticity gradients normal to the boundary. Since vorticity is diffused in the same manner as momentum, the smoothing action of viscosity will try to equalize the level of vorticity where a gradient exists. This results in a flux of vorticity either from or to the surface.

Prediction of vorticity flux was extended to free surfaces by Lugt (1987) who used local series expansion about points on the free surface. More recently, Rood (1995, 1994) and Wu (1995) have interpreted the vorticity flux

---

†A version of this chapter has been submitted to the Journal of Fluids Engineering for publication

from free surfaces in a more general sense. Lundgren and Koumoutsakos (1997) have constructed numerical schemes to predict the creation of vorticity at a free surface using the vorticity flux. For a review of recent work on the dynamics of free surfaces we refer the reader to Sarpkaya (1996).

Our paper is organized as follows. Several formulae used in this paper's derivations are presented in Sec. 3.2. The level of vorticity required to satisfy free surface boundary conditions is reviewed in Sec. 3.3. General expressions for the vorticity flux are derived in Sec. 3.4. Some results in this section are useful for calculating Φ from a rigid boundary. Here we also discuss the topology of vortex lines at the surface. A vorticity flux equation specialized for steady surfaces is derived in Sec. 3.4.3.

3.2 Preliminary formulae

We begin by presenting definitions and deriving formulae used to describe two-dimensional surfaces embedded in three-dimensional Euclidian space $\mathbb{R}^3$. Equations requiring results from differential geometry are derived with added detail.

3.2.1 Geometry

The tensor product of two arbitrary vectors $\mathbf{a}$, $\mathbf{b}$ is defined as $(\mathbf{a} \otimes \mathbf{b})\mathbf{c} = \mathbf{a}(\mathbf{b} \cdot \mathbf{c})$. Spatial forms of $\nabla \cdot (\ )$, $\nabla \times (\ )$, $\nabla(\ )$ are denoted div( ), curl( ) and grad( ).

We construct a convected coordinate system $\theta^i = (\theta^\alpha)$ that maintains fixed correspondence with particles embedded in the material surface $\mathcal{S}$. Here Latin indices are understood to range over $(1, 2, 3)$ and Greek indices $(1, 2)$; summation on repeated indices is implied.

A point on $\mathcal{S}$ is located relative to a fixed basis in $\mathbb{R}^3$ with the position vector $\mathbf{r} = \mathbf{r}(\theta^\alpha, t)$. Partial derivatives of $\mathbf{r}$ with respect to surface coordinates θ^α give the covariant basis vectors $\mathbf{a}_\alpha$ along θ^α; $\mathbf{r}_{,\alpha} = \mathbf{a}_\alpha$. Partial differentiation with respect to surface coordinates is represented with a comma and Greek subscript. The subscript 3 is reserved for differentiation with respect to θ^3. The covariant derivative will be denoted with a vertical bar and subscript $(\ )|_\beta$. For arbitrary contravariant components of a vector $\mathbf{c}$ the covariant derivative is

$$c^\alpha|_\beta = c^\alpha{}_{,\beta} + \Gamma^\alpha_{\gamma\beta} c^\gamma. \tag{3.1}$$
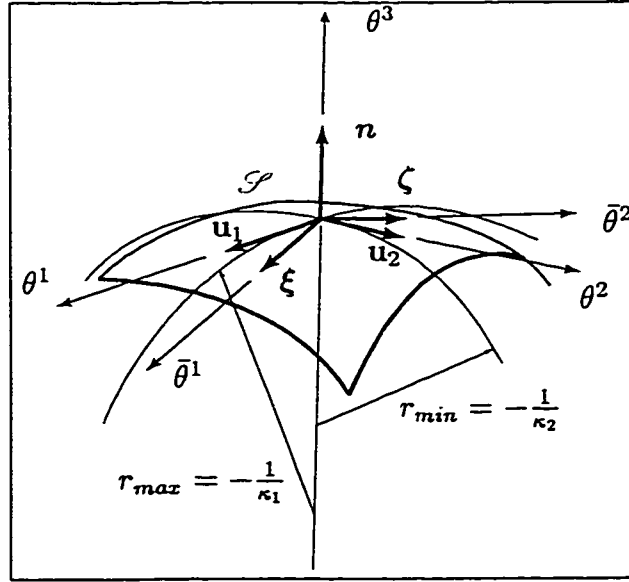
Figure 3.1: Two orthonormal coordinate systems embedded in $\mathscr{S}$, (θ^1, θ^2) and $(\bar{\theta}^1, \bar{\theta}^2)$.

The surface Christoffel symbol appears in Eq. (3.1) and is defined by

$$\Gamma^{\alpha}_{\gamma\beta} = a^{\alpha} \cdot a_{\gamma,\beta} \,. \tag{3.2}$$

For further details we refer the reader to Kreyszig (1991).

The vectors a_{α} span the tangent plane and can be used to calculate the surface normal $n = (a_1 \times a_2)/|a_1 \times a_2|$. The gradient of n gives the symmetric curvature tensor b,

$$\text{grad}\, n = -n_{,\alpha} \otimes a^{\alpha} = -b^{\beta}_{\alpha} a_{\beta} \otimes a^{\alpha} = -b = -b^{\mathrm{T}}, \tag{3.3}$$

where we have used Weingarten's equation,

$$n_{,\alpha} = -b^{\beta}_{\alpha} a_{\beta}. \tag{3.4}$$

The contravariant basis vector a^{β} has been introduced in Eq. (3.2) and Eq. (3.3). This is related to a_{α} through the surface metric $a_{\alpha\beta} = a_{\alpha} \cdot a_{\beta}$ by $a_{\alpha} = a_{\alpha\beta} a^{\beta}$.

We will find it useful to define an orthonormal basis embedded in $\mathscr{S}$, (ξ, ζ, n) where ξ and ζ are orthogonal unit vectors in the tangent plane

such that $\xi \times \zeta = n$, Fig. 3.1. This coordinate system has the advantage that quantities referenced to it will be physical components of that quantity. Quantities referenced to a contravariant or covariant basis may not even have the same physical dimensions as their physical counterpart.

In orthogonal coordinates b takes on the form,

$$b = \kappa_\xi \xi \otimes \xi + \kappa_\zeta \zeta \otimes \zeta + \tau(\xi \otimes \zeta + \zeta \otimes \xi). \tag{3.5}$$

Here, $\kappa_\xi = -1/r_\xi$, $\kappa_\zeta = -1/r_\zeta$ are the normal curvatures and τ represents the surface twist. In lines-of-curvature coordinates, κ_ξ and κ_ζ correspond to principal curvatures of b so that $\tau = 0$ and,

$$b = \kappa_1 u_1 \otimes u_1 + \kappa_2 u_2 \otimes u_2, \tag{3.6}$$

where κ_1, κ_2 are the principal curvatures and u_1 and u_2 are the principal directions. We will also use the two scalar invariants of b, the mean curvature $H = \operatorname{div} b/2 = (\kappa_1 + \kappa_2)/2 = (\kappa_\xi + \kappa_\zeta)/2$ and the Gaussian curvature, $K = \det b = \kappa_1\kappa_2 = \kappa_\xi\kappa_\zeta - \tau^2$.

3.3 Vorticity at a free surface

In this section we briefly discuss the level of vorticity required to satisfy boundary conditions at a free surface. Complete derivations of these results are available in Peck and Sigurdson (1998).

We assume a two-dimensional material surface $\mathscr{S}$ separates two regions of fluid, $\mathscr{R}^1$ and $\mathscr{R}^2$. Surface tractions $t_{(n)}$ in one region, say $\mathscr{R}^1$, are assumed to be negligible except for a constant pressure p_o. The level of vorticity at $\mathscr{S}$ can be calculated by considering the jump in $t_{(n)}$ across $\mathscr{S}$. Thus, on $\mathscr{S}$, the following boundary conditions must be satisfied:

$$[t_{(n)}] = -\rho_{\mathscr{S}}(\dot{v} - f_{\mathscr{S}}) + \operatorname{div} S. \tag{3.7}$$

Here, [] denotes a jump in a quantity across $\mathscr{S}$. Body forces acting on surface elements are denoted $f_{\mathscr{S}}$. An intrinsic surface stress S is assumed to depend on surface tension γ through the constitutive equation $S = \gamma a^\alpha \otimes a_\alpha$. The fluid velocity of particles embedded in $\mathscr{S}$ is represented with v. The velocity of particles in the bulk fluid is denoted u. If the surface density $\rho_{\mathscr{S}}$ is assumed small Eq. (3.7) becomes

$$Dn - [n \cdot (Dn)]n = \frac{1}{2\mu} \operatorname{grad}_{\mathscr{S}} \gamma. \tag{3.8}$$

The symmetric portion of the velocity gradient tensor $\mathbf{L}$ is the rate-of-strain tensor $\mathbf{D} = (\mathbf{L} + \mathbf{L}^{\mathrm{T}})/2$. A surface gradient operator is represented with $\mathrm{grad}_{\mathscr{S}}$. Eq. (3.8) can be rearranged as,

$$\mathbf{W}n = \dot{n} + \frac{1}{2\mu}\,\mathrm{grad}_{\mathscr{S}}\gamma, \tag{3.9}$$

where $\mathbf{W} = (\mathbf{L} + \mathbf{L}^{\mathrm{T}})/2$ is the spin tensor and $\dot{n}$ is the material derivative of the surface normal. $\mathbf{W}$ is a skew symmetric tensor so that an axial vector ω exists given by $2\mathbf{W}n = \omega \times n$; in this case $\omega = \mathrm{curl}\,u$ is the vorticity. Substituting this relation into Eq. (3.9) gives the following expression for the tangential component of vorticity ω_t on $\mathscr{S}$:

$$\omega_t = 2n \times \dot{n} + \frac{1}{\mu}n \times \mathrm{grad}_{\mathscr{S}}\gamma. \tag{3.10}$$

Here, and for the remainder of this text the subscript $(\ )_t$ denotes components of a vector tangential to $\mathscr{S}$. The material derivative of n in surface coordinates is

$$\dot{n} = -\mathrm{grad}_{\mathscr{S}}(v) - b_\alpha^\beta v_\beta a^\alpha = -\mathrm{grad}_{\mathscr{S}}(v) - \mathbf{b}v_t. \tag{3.11}$$

We refer the reader to Naghdi (1972) for this derivation of $\dot{n}$. Substituting Eq. (3.6) into Eq. (3.11) gives the level of tangential vorticity on $\mathscr{S}$ in lines-of-curvature components,

$$\omega_t = 2\,\mathrm{grad}_{\mathscr{S}}(v) \times n + 2(\kappa_2 v_2)\mathbf{u}_1 - 2(\kappa_1 v_1)\mathbf{u}_2. \tag{3.12}$$

Alternatively, we can express ω_t with the basis used in Eq. (3.5) where the influence of the surface twist on the level of vorticity is now represented:

$$\omega_t = 2\,\mathrm{grad}_{\mathscr{S}}(v) \times n + 2(\kappa_\zeta v_\zeta + \tau v_\xi)\boldsymbol{\xi} - 2(\kappa_\xi v_\xi + \tau v_\zeta)\boldsymbol{\zeta}. \tag{3.13}$$

3.4   Vorticity flux

Until now, we have only examined the level of vorticity required to satisfy boundary conditions on $\mathscr{S}$. We can gain insight into the rate at which vorticity enters or leaves the bulk fluid from the surface through expressions for the vorticity flux. In the derivations that follow, most of the equations are valid for any material surface embedded in a fluid. The case of a free surface

is examined by directly substituting values required by boundary conditions into the momentum equation.

In this paper's context, the vorticity flux Φ is defined by,

$$\Phi = \nu \operatorname{grad} \omega \, n = \nu \frac{\partial \omega_t}{\partial \theta^3} + \nu \frac{\partial(\omega n)}{\partial \theta^3}. \tag{3.14}$$

The first term on the right of Eq. (3.14) represents normal gradients of vorticity tangent to $\mathscr{S}$. The second term on the right represents the normal gradients of vorticity normal to the surface. ω will be used to represent the scalar component of vorticity normal to $\mathscr{S}$ so that ωn is the normal vector component of ω.

3.4.1 Flux of normal vorticity

The vorticity flux of normal vorticity ωn is readily derived from the vorticity field's solenoidal property:

$$\operatorname{div} \omega = \operatorname{tr}(\operatorname{grad} \omega) = 0. \tag{3.15}$$

To calculate the surface divergence, the vorticity gradient tensor is first calculated in terms of surface coordinates,

$$\operatorname{grad} \omega = \omega_{,\alpha} \otimes \mathbf{a}^\alpha + (\omega)_{,3} \otimes n. \tag{3.16}$$

After differentiating and grouping terms we obtain

$$\begin{aligned}\operatorname{grad} \omega = {}& (\omega^\alpha|_\beta - b^\alpha_\gamma \omega) \mathbf{a}_\alpha \otimes \mathbf{a}^\beta + \omega^\alpha{}_{,3} \, \mathbf{a}_\alpha \otimes n \\ &+ (\omega_{,\beta} + b^\alpha_\beta \omega_\alpha) n \otimes \mathbf{a}^\beta + \omega_{,3} \, n \otimes n.\end{aligned} \tag{3.17}$$

Taking the trace of the vorticity gradient tensor yields,

$$\begin{aligned}\operatorname{tr}(\operatorname{grad} \omega) &= \operatorname{tr}[\omega_{,\alpha} \otimes \mathbf{a}^\alpha + (\omega n)_{,3} \otimes n] \tag{3.18}\\ &= \omega^\alpha|_\alpha - b^\alpha_\alpha \omega + \omega_{,3} \\ &= \omega^\alpha|_\alpha - 2H\omega + \omega_{,3} = 0\end{aligned}$$

The mean curvature H appears in Eq. (3.18) which is the arithmetic mean of any two orthogonal normal curvatures at a point on $\mathscr{S}$.

Obtaining an expression for the flux of normally directed vorticity is a simple matter of rearranging Eq. (3.18) and multiplying by ν,

$$\nu \frac{\partial(\omega n)}{\partial \theta^3} = \nu(2H\omega - \omega^\alpha|_\alpha)n \tag{3.19}$$

It is important to note that the mean curvature is dependent on surface orientation. This means the sign of H is dependent on the direction of the unit normal to $\mathscr{S}$. In the present context n is assumed to point away from the bulk fluid.

3.4.2 Flux of tangential vorticity

Tangential components of $\boldsymbol{\Phi}$ represent the flux of ω_t from $\mathscr{S}$. An expression for this can be derived from the momentum equation

$$\rho(a - g) = \operatorname{div} \sigma. \tag{3.20}$$

Here $\sigma = -p\mathbf{I} + 2\mu\mathbf{D}$ is the Cauchy stress, a is the fluid acceleration and g is the body force; for our purposes g will only be assumed to represent gravity. We decompose Eq. (3.20) into normal and tangential components as follows,

$$\rho\tilde{a} = [n \cdot (\rho\tilde{a})]n + n \times (\rho\tilde{a} \times n) = [n \cdot (\operatorname{div} \sigma)]n + n \times (\operatorname{div} \sigma \times n) \tag{3.21}$$

For convenience $\tilde{a}$ will be used to represent $(a - g)$. Using the constitutive equation given above and equating tangential components of Eq. (3.20) gives,

$$\rho\tilde{a}_t = -\operatorname{grad}_{\mathscr{S}} p - n \times (\mu \operatorname{curl} \omega \times n), \tag{3.22}$$

where we have used the identity $\operatorname{div} \operatorname{grad} u = \operatorname{grad}(\operatorname{div} u) - \operatorname{curl} \operatorname{curl} u$. Placing our attention on the last right hand side term of Eq. (3.22) we recognize $\operatorname{curl} \omega$ as the axial vector of a skew-symmetric tensor formed from $(\operatorname{grad} \omega - \operatorname{grad} \omega^{\mathrm{T}})$ so that $(\operatorname{grad} \omega - \operatorname{grad} \omega^{\mathrm{T}})n = \operatorname{curl} \omega \times n$. Substituting into Eq. (3.22) gives

$$\rho\tilde{a}_t = -\operatorname{grad}_{\mathscr{S}} p - \mu n \times (\operatorname{grad} \omega n - \operatorname{grad} \omega^{\mathrm{T}} n), \tag{3.23}$$

or, in terms of the vorticity flux:

$$\nu \operatorname{grad} \omega n = n \times \tilde{a}_t + n \times \frac{\operatorname{grad}_{\mathscr{S}} p}{\rho} + \nu \operatorname{grad} \omega^{\mathrm{T}} n. \tag{3.24}$$

For our purposes, the last term on the right of Eq. (3.24) is expressed more conveniently using the identity

$$\operatorname{grad} \omega^{\mathrm{T}} n = \operatorname{grad}(\omega \cdot n) - \operatorname{grad} n^{\mathrm{T}} \omega = \operatorname{grad}(\omega) + b\omega_t. \tag{3.25}$$

Since b is purely a surface tensor it will only operate on a surface vector so $b\omega$ can be replaced with $b\omega_t$. Also

$$\text{grad}(\omega) = \text{grad}_{\mathscr{S}}(\omega) + \frac{\partial \omega}{\partial \theta^3} n \qquad (3.26)$$

Substituting this result in Eq. (3.25), Eq. (3.24) becomes

$$\nu \frac{\partial \omega_t}{\partial \theta^3} = n \times \tilde{a}_t + n \times \frac{\text{grad}_{\mathscr{S}} p}{\rho} + \nu \, \text{grad}_{\mathscr{S}}(\omega) + \nu b\omega_t \qquad (3.27)$$

The first term on the right represents tangential acceleration of material elements on $\mathscr{S}$, the second term the tangential pressure gradient. The normal gradients of normal vorticity in Eq. (3.26) cancel those within $\text{grad}\,\omega n$ so we are left with the third term on the right of Eq. (3.27) which is the surface gradient of the normally directed vorticity. The curvature tensor appears in the last term of Eq. (3.27). This term represents the vorticity flux due to surface curvature acting on the component of vorticity tangential to $\mathscr{S}$.

At this point Eq. (3.27) is simply an alternate expression of the momentum equation tangential to any arbitrary material surface embedded in $\mathbb{R}^3$. No boundary conditions have been imposed to reflect the presence of a free surface. If a vortex ring were to approach this surface there would be no reason for the vortex ring to be deflected from its path. Thus, the wide variety of phenomena associated with vortex-free surface interactions such as vortex ring rebound and vortex reconnection are not predicted using this equation without imposing suitable boundary conditions (Sarpkaya, 1996; Bernal and Kwon, 1989).

We introduce Φ_κ to represent the last term on the right of Eq. (3.27)

$$\Phi_\kappa = \nu b\omega_t. \qquad (3.28)$$

Interpretation of Φ_κ has caused some confusion in the literature (Rood, 1994). The primary purpose of the present paper is to clarify the conditions under which this term may be neglected.

On a free surface, the level of tangential vorticity is set as derived in Sec. 3.3. Introducing this boundary condition into Eq. (3.27) provides insight into Φ_κ. If surface tension gradients are negligible or the ratio γ/μ is negligible we write ω_t on $\mathscr{S}$ as,

$$\omega_t = 2n \times \dot{n}. \qquad (3.29)$$

Substituting into Eq. (3.27) gives

$$\nu \frac{\partial \omega_t}{\partial \theta^3} = n \times \bar{a}_t + n \times \frac{\text{grad}_{\mathscr{S}} p}{\rho} + \nu \, \text{grad}_{\mathscr{S}}(\omega) + \underbrace{2\nu \mathbf{b}(n \times \dot{n})}_{\Phi_\kappa}. \tag{3.30}$$

We may also write Φ_κ as

$$2\nu \mathbf{b} \left(n \times \frac{\dot{n}}{\|\dot{n}\|} \|\dot{n}\| \right) = 2\nu \|\dot{n}\| \mathbf{b} \mathbf{t} \tag{3.31}$$

where $\mathbf{t}$ is a unit vector directed along the tangential vorticity. $\mathbf{t}$ is calculated from the vector product of n and the normalized $\dot{n}$; $\mathbf{t} = n \times \dot{n}/\|\dot{n}\|$.

Writing $\mathbf{b}$ in terms of lines-of-curvature components Eq. (3.31) becomes,

$$2\nu \|\dot{n}\| [\kappa_1 (\mathbf{u}_1 \cdot \mathbf{t}) \mathbf{u}_1 + \kappa_2 (\mathbf{u}_2 \cdot \mathbf{t}) \mathbf{u}_2] \tag{3.32}$$

Hence, if $\mathbf{t}$ is directed along a zero-valued principal curvature, Φ_κ vanishes. This does not imply that vortex lines along $\mathbf{t}$ are straight however. As an example, consider the surface shown in Fig. 3.2. For this example we have chosen a surface of revolution. The profile curve is a Bessel function, the surface being formed by revolving this curve shown in Fig. 3.3 around the vertical axis. The precise function which describes the surface is unimportant, rather the overall qualitative analysis is what we are interested in. On this surface the parallels and meridians are lines-of-curvature so that at each point on $\mathscr{S}$ the principal curvatures are directed along these curves. We denote the principal curvature directed along the surface parallel as κ_π and that directed along the meridians as κ_μ. In the present case $\kappa_\pi = \kappa_1$ and $\kappa_\mu = \kappa_2$. A plot of κ_π, κ_μ and the Gaussian curvature K for the surface in Fig. 3.2 is shown in Fig. 3.4. We will see the significance of the Gaussian curvature in Sec. 3.4.3. From Fig. 3.2 and Fig. 3.4 we see that κ_π, the normal curvature in the direction of the vortex lines vanishes at the local maxima and minima of the generating curves which means that Φ_κ necessarily vanishes at these points. However, the vortex lines at these points are not straight but form a set of concentric circles about the vertical axis. Hence, the result given in Rood (1994) does not hold: vortex lines may be curved with $\Phi_\kappa \neq 0$.

Further complication arises if $\mathbf{t}$ is not directed along a principal direction of curvature. If this is the case Φ_κ becomes

$$2\nu \|\dot{n}\| [\kappa_\xi (\xi \cdot \mathbf{t}) \xi + \tau (\zeta \cdot \mathbf{t}) \zeta]. \tag{3.33}$$
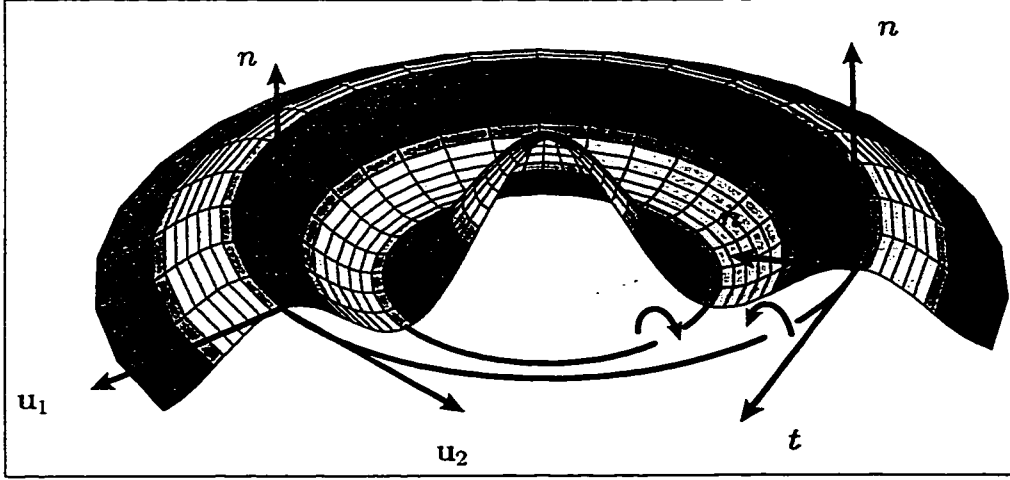
Figure 3.2: A surface of revolution formed by rotating a Bessel function around the vertical axis. Radially directed lines are surface meridians, the circular lines are surface parallels. Lines-of-curvature correspond to meridians and parallels. Surface shading indicates the Gaussian curvature's sign. Darkly shaded regions denote hyperbolic regions $K < 0$, lightly shaded regions are parabolic $K = 0$. Unshaded regions are elliptic $K > 0$. The two dark lines are representative vortex lines. The sign of the vorticity is indicated in the figure

This shows that even if the normal curvature vanishes along t a component of vorticity flux due to surface twist would still exist

$$\Phi_\kappa = 2\nu \|\dot{n}\| \tau \zeta. \tag{3.34}$$

For illustration we consider the surface shown in Fig. 3.5. Here we assume vortex lines are directed along rules of the hyperbolic paraboloid shown. The rules of $\mathscr{S}$ are straight lines embedded in $\mathscr{S}$, hence they have no normal curvature and the surface has no normal curvature in that direction. In this case, even though the vortex lines are straight Φ_κ is nonzero.

3.4.3 The vorticity flux equation at a steady surface

This section describes a convenient means for assessing effects of surface curvature on Φ_κ from a steady surface. By a steady surface we mean a surface where $\mathrm{grad}_{\mathscr{S}}(v) = 0$. This implies that there is no local rotation of
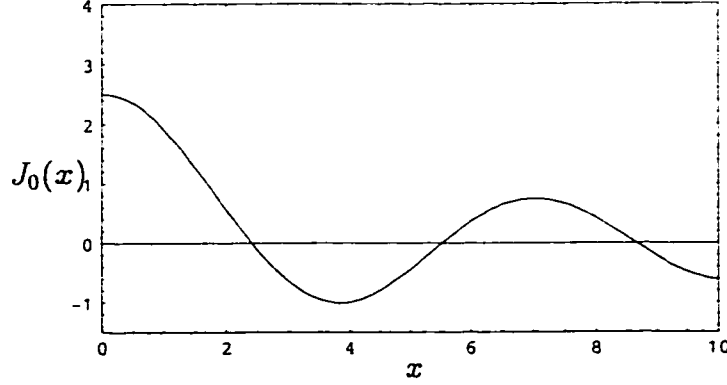
Figure 3.3: A Bessel function of the first kind $f(x) = J_0(x)$. This is the generating curve used for the surface of revolution shown in Fig. 3.2.

$\mathscr{S}$ in the chosen reference frame. We may also view this analysis as being that for the steady component of Φ_κ on an unsteady surface.

With this steady surface simplification Eq. (3.12) becomes,

$$\begin{aligned}
\omega_t &= 2\mathbf{b}v_t \times \mathbf{n} \\
&= 2b_\beta^\alpha v_\alpha \mathbf{a}^\beta \times \mathbf{n} \\
&= -2b_\beta^\alpha v_\alpha \varepsilon^{\beta\rho} \mathbf{a}_\rho
\end{aligned} \tag{3.35}$$

Substituting Eq. (3.35) into the last term on the right of Eq. (3.27) gives

$$\begin{aligned}
\Phi_\kappa &= -2\nu b_\lambda^\gamma b_\beta^\alpha v_\alpha \varepsilon^{\beta\rho} \mathbf{a}_\gamma \otimes \mathbf{a}^\lambda \mathbf{a}_\rho, \\
&= -2\nu b_\beta^\alpha b_\rho^\gamma v_\alpha \varepsilon^{\beta\rho} \mathbf{a}_\gamma, \\
&= -2\nu K v_\alpha \varepsilon^{\alpha\gamma} \mathbf{a}_\gamma \\
&= 2\nu K v \times \mathbf{n},
\end{aligned} \tag{3.36}$$

after noting $b_\beta^\alpha b_\rho^\gamma \varepsilon^{\beta\rho} = K\varepsilon^{\alpha\gamma}$. We can also rewrite Eq. (3.36) in the convenient form

$$\Phi_\kappa = 2\nu K q\hat{t}, \tag{3.37}$$

where $q = \|v\|$ and $\hat{t} = m \times n$ is a unit vector normal-to the plane containing the surface normal and the unit vector m directed along v.
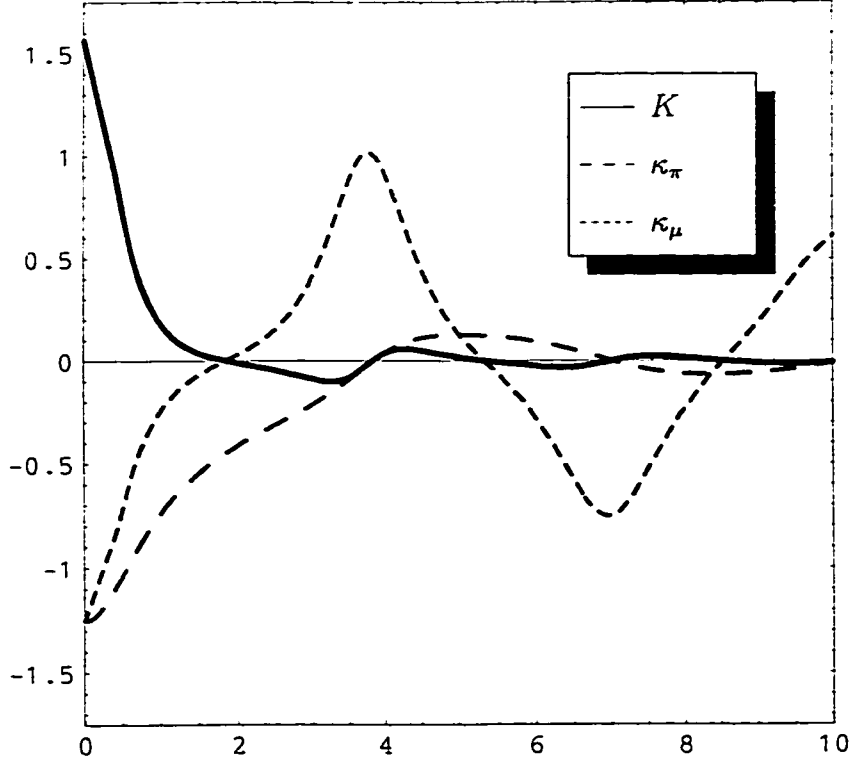
Figure 3.4: The value of the principal curvatures κ_π and κ_μ on the surface shown in Fig. 3.2 as a function of radial distance x from the axis of revolution.The Gaussian curvature K is also shown.

In Eq. (3.36) and Eq. (3.37) the Gaussian curvature K appears. K is a scalar invariant independent of direction on $\mathscr{S}$. The sign of K characterizes regions of a surface as elliptic $K > 0$, parabolic $K = 0$ or hyperbolic $K < 0$. A developable surface is a surface which is parabolic everywhere.

From Eq. (3.37) we see that determining the sign of Φ_κ is a matter of assessing the sign of K and knowing the direction of v. Hence if the flow passes from an elliptic region to a hyperbolic region the sign of Φ_κ will change. This is a convenient method since we do not need knowledge of ω_t. Nor do we require knowledge of the normal curvatures or surface twist beyond what is necessary for calculating K.

Thus we have a convenient method of determining if the -curvature-dependent term will contribute to the vorticity flux in a steady flow. If the
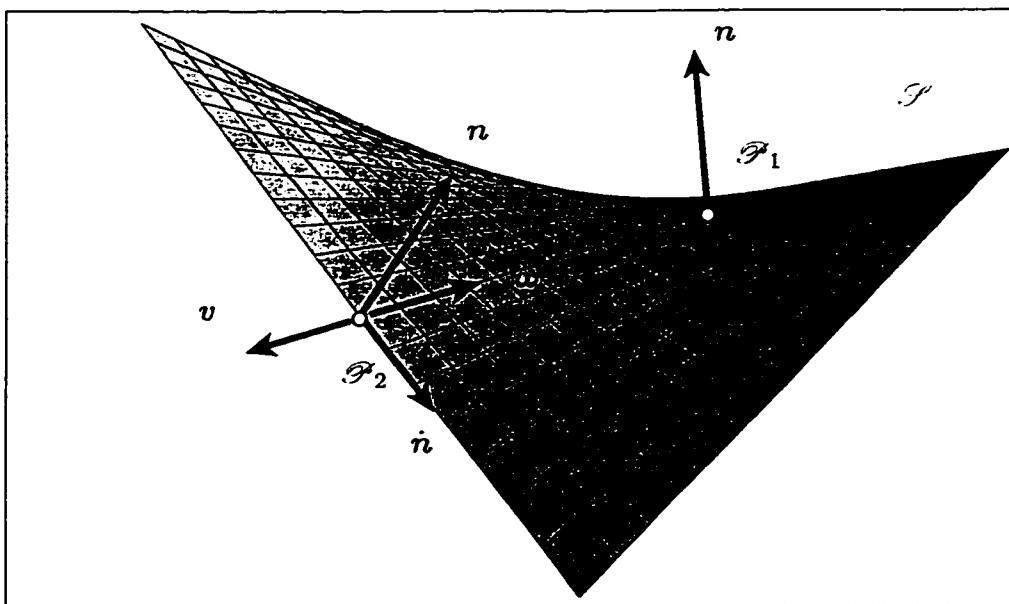
Figure 3.5: Local flow on a hyperbolic paraboloid. The fluid velocity v is assumed directed along a rule of the surface. Hence, as a fluid element travels from $\mathscr{F}_1$ to $\mathscr{F}_2$ n rotates due to the surface twist implying the sign of vorticity indicated. In this case the vortex line is straight.

Gaussian curvature is nonzero and $\|v\| \neq 0$ there will be a contribution. If the surface is developable or is locally parabolic there will be no contribution regardless of the flow's direction: $\Phi_\kappa = 0$.

We consider steady two-dimensional plane waves as an example. Here $\mathscr{S}$ is a surface of translation and the flow is assumed directed along the generating curve. A nonzero level of vorticity occurs at points of inflection on the generating curve where the normal curvature directed along the curve vanishes. Since the principal curvature normal to the generating curve is always zero, the surface is developable and Φ_κ vanishes. Indeed the direction of the flow is irrelevant to Φ_κ. No matter which way the flow is directed $K = 0$ and $\Phi_\kappa = 0$.

The sign of K on surfaces with more complex geometry—even one-dimensional surfaces such as a torus—is not always so obvious. As an example we have illustrated the Gaussian curvature of a torus by shading the surface as shown in Fig. 3.6. This could represent the geometry of a toroidal
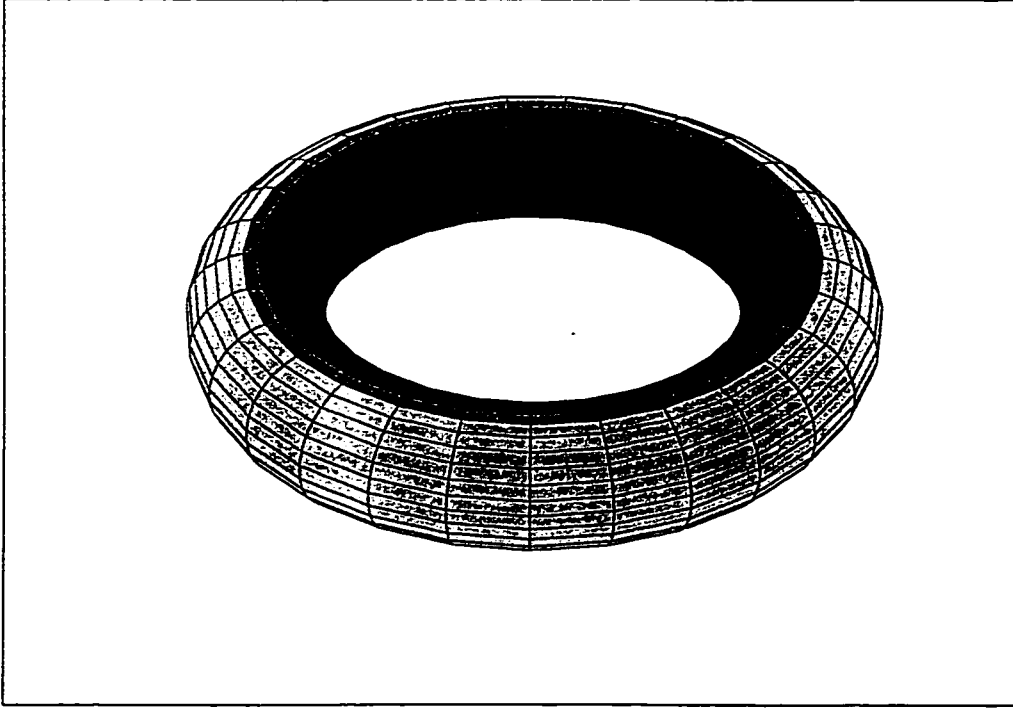
Figure 3.6: A torus colored with Gaussian curvature. As with Fig. 3.2 hyperbolic points are colored with a dark shade, elliptic points with a light shade. Intermediate shades represent parabolic regions

bubble rising in water. Here the inner regions of the torus are hyperbolic while the outer regions are elliptic, the dividing region being parabolic. The parabolic region is caused by a vanishing principal curvature directed along the surface parallel. Hence in the parabolic regions Φ_κ will vanish. Also, if the direction of the flow does not change, the sign of Φ_κ will change as we move form hyperbolic to elliptic regions.

A still more complex one-dimensional surface shown in Fig. 3.2 is colored with Gaussian curvature. As in Fig. 3.6, K vanishes at the local minima and maxima of the generating curve due to vanishing κ_π. The Gaussian curvature is also zero at points of inflection on the generating curve since at these points κ_μ vanishes.

Further simplification of tangential vorticity flux equation is possible if both the surface and flow are steady. First, we rewrite the kinematic expres-

sion for the fluid acceleration,

$$\tilde{a} = a - g = \frac{\partial u}{\partial t} + Lu - g. \tag{3.38}$$

Since the flow is assumed steady, $\frac{\partial u}{\partial t} = 0$. Now a becomes $Lu = L^T u + 2Wu$ so that

$$a = \frac{1}{2} \operatorname{grad}(u^2) + \omega \times u. \tag{3.39}$$

after using the relation $L^T u = \operatorname{grad}(u^2)/2$. If we assume there is no normal vorticity the vector product of n with the Lamb vector $\omega \times u$ vanishes as does the surface gradient of normal vorticity so that Eq. (3.27) becomes

$$\nu \frac{\partial \omega_t}{\partial \theta^3} = -\operatorname{grad}_{\mathscr{S}} \mathscr{H} \times n - 2\nu K(q\hat{t}) \tag{3.40}$$

where the surface streamline is assumed directed along m. The total head is $\mathscr{H} = \frac{1}{2}u^2 + p/\rho + \Omega$ and $\operatorname{grad}\Omega = -g$. This gives a simple extension to Lugt's result (Lugt, 1987). Hence, Lugt's result holds for all developable steady surface's and is valid at all parabolic points on a free surface.

Bibliography

L. P. Bernal and J. T. Kwon. Vortex ring dynamics at a free-surface. *Phys. Fluids A*, 1(3):449–451, March 1989.

Dana Dabiri. On the correlation of the free-surface roughness with the near-surface turbulence. In *Bull. Am. Phys Soc.*, page 2162. American Physical Society, November 1997.

Erwin Kreyszig. *Differential Geometry*. Dover, New York, 1991.

M. J. Lighthill. *Laminar Boundary Layers*, chapter Introduction, pages 46–113. Oxford University, 1963.

Hans J. Lugt. Local flow properties at a viscous free-surface. *Phys. Fluids*, 30(12):3647–3652, December 1987.

Thomas Lundgren and Petros Koumoutsakos. On the generation of vorticity at a free-surface. In *Bull. Am. Phys Soc.*, page 2163. American Physical Society, November 1997.

P. M. Naghdi. *S. Flugge's Handbuch der Physik*, volume VIa/2, chapter The theory of plates and shells, pages 425–640. Springer, Berlin, 1972.

Bill Peck and Lorenz Sigurdson. On the kinematics at a free surface. *IMA J. of Appl. Math.*, 60:1–13, 1998.

Edwin P. Rood. Interpreting vortex interactions with a free-surface. *J. Fluids Engineering*, 116:91–93, March 1994.

Edwin P. Rood. *Fluid Vorticies*, chapter Vorticity Interactions with a Free-Surface. Kluwer Academic, 1995.

Turgut Sarpkaya. Vorticity, free-surface and surfactants. *Annu. Rev. Fluid Mech.*, 28:83–128, 1996.

Jie-Zhi Wu. A theory of three-dimensional interfacial vorticity. *Phys. Fluids*, 7(10):2375–2395, October 1995.

CHAPTER 4

CREATION OF VORTICITY AT A THIN INTERFACE

4.1 Introduction

This chapter describes how torques are applied to material elements at a fluid interface to generate vorticity. This discussion is very different from that in the preceding two chapters. In Chpt. 2, only the level of vorticity was calculated for an interface where the tangential surface tractions vanished. In that case we would only surmise that vorticity of sufficient strength was created by some means to satisfy the boundary condition. In Chpt. 3 the flux of vorticity was calculated but no dynamical means were suggested for the application of torques to the fluid elements. In both cases vorticity creation could only be inferred; the process which created vorticity could not be deduced.

The evolution of the vorticity field can be predicted with the vorticity equation. This equation is derived by calculating the curl of Cauchy's equation:

$$\rho \mathbf{a} = \text{div}\,\boldsymbol{\sigma} + \rho \mathbf{g}. \tag{4.1}$$

Here ρ is the fluid density, a is the acceleration and $\boldsymbol{\sigma}$ is the Cauchy stress. In a homogeneous viscous fluid the vorticity equation becomes

$$\frac{\partial \boldsymbol{\omega}}{\partial t} + \text{grad}\,\boldsymbol{u}\,\boldsymbol{\omega} = \text{grad}\,\boldsymbol{\omega}\,\boldsymbol{u} + \nu\,\text{div}\,\text{grad}\,\boldsymbol{\omega}. \tag{4.2}$$

---

†Much of this work was presented at the 1996 meeting of the American Physical Society (Peck and Sigurdson, 1996) and the 13th Canadian Symposium on Fluid Mechanics. A version of this chapter is to be submitted to the Philosophical Transactions of the Royal Society, Series A.

Morton (1984) points out that there is no true production term in this equation. For an initially irrotational flow vorticity will not be created from where there was none before. Chorin (1994) describes this as vorticity being unable to be created *ab nihilo* (from nothing). A more thorough discussion is available in Batchelor (1967) and Truesdell (1954). As both authors point out vorticity can only be created at the boundaries and diffused inward.

The effect of variable density and viscosity on circulation was investigated by Jeffreys (1928) and later by Truesdell (1949). Here they concluded in a very general way that vorticity must be created in a circuit initially encompassing a region of irrotational flow since the integral giving the rate of change of circulation

$$\frac{d\Gamma}{dt} = \oint (\frac{\mathrm{div}\,\sigma}{\rho} - \mathbf{g}) \cdot d\mathbf{x} \neq 0. \tag{4.3}$$

Truesdell (1949) identifies a mechanism whereby circulation is created due to viscous gradients alone.

The vorticity equation Eq. (4.1) becomes much more complex if fluid viscosity and density are both allowed to vary. This form of the equation has received very little attention in the literature. A general result is available in Dutton (1995) where the vorticity equation is derived in the context of atmospheric motions. Green (1995) derives a similar equation in a general form but provides some explanation of the terms produced in the analysis. Mueller (1996) and Mueller et al. (1997) derive the vorticity equation with variable density and viscosity to investigate vorticity creation in combustion processes. These results are in very general form and the authors conclude that viscosity gradients in their problem are small enough to be neglected. All of the results mentioned so far are left in a very general form which does not provide any further insight into the problem of vorticity creation at a thin interface especially the effect of surface curvature on vorticity creation.

To predict the evolution of vorticity at an interface we derive the vorticity transport equation for a fluid body where density and viscosity are allowed to vary rapidly but smoothly across a thin zone separating two regions of otherwise constant material properties. In one region the viscosity and density are both large while in the other, density and viscosity are assumed small. We assume the direction of the viscosity and density gradients are normal to the surface which allows us to take the derivation further than those cited above. As a result we discover terms predicting vorticity creation which are consistent with the levels of vorticity in Chpt. 2.

This scheme is similar in spirit to that used by Dahm et al. (1989) to calculate the vorticity creation at a thin density interface. In that paper, only the density was allowed to vary across a thin interface whereas the viscosity was held fixed over the entire domain. With these assumptions they predicted the creation of vorticity by baroclinic torques. The baroclinic torque is created by net pressure forces on a fluid element not acting through the element's mass centroid, thus creating a torque on the element. The effect of baroclinic torques at free-surfaces has been widely studied in a variety of papers. Most have been the basis for boundary-integral numerical schemes, (Zarodny and Greenberg, 1973; Baker, 1983; Baker et al., 1980, 1984). These methods modify the strength of a vortex sheet separating two masses of inviscid fluid with different densities. Once the vortex-sheet strength is known at the boundary a velocity potential in each region can be deduced from which the velocity field follows.

A model which only includes baroclinic torques is not satisfactory for the case of a viscous free-surface model. As pointed out in Chpt. 2, the level of vorticity predicted by equation Eq. (2.16) is independent of the density jump across the interface—the vorticity level is only dependent on the viscosity jump. If there is no density jump baroclinic torques cannot exist. We must look for other means to explain the generation of torques.

The thin region used in our analysis is a simple model of a real fluid interface. This model differs greatly from that used in the previous two chapters where the interface was modeled as a singular surface with no thickness. The thin interface model assumes that the continuum assumption applies through this region. Analyses based on such assumptions appears in previous articles such as Antanovskii (1995); Dunn and Serrin (1983); Blinowski (1973b,a). More complete references can be found in these papers. The validity of applying such a continuum assumption to a fluid interface was addressed by Koplik and Banavar (1994). Here they concluded through numerical analysis that the continuum model may not be appropriate for a fluid-air interface. However, this area is still a very active area of ongoing research.

The thin interface model does not include surface tension effects. Unlike a sharp-interface analysis, including surface tension effects requires modification of the constitutive response in the interface. We address this in Sec. 4.2.6.

-

4.2 Vorticity transport equation

4.2.1 General Form

In this section we derive the vorticity equation for a fluid with varying density and viscosity. We begin by rearranging Eq. (4.1) into a form convenient for derivations to follow:

$$\rho \left(\frac{du}{dt} - g \right) = \text{div } \sigma. \tag{4.4}$$

We assume ρ can vary in space but the fluid is still volume-preserving (isochoric), hence div $u = 0$. Taking the curl of Eq. (4.4) and rearranging gives,

$$\rho \, \text{curl} \left(\frac{du}{dt} \right) = - \text{grad } \rho \times \left(\frac{du}{dt} - g \right) + \text{curl}(\text{div } \sigma) \tag{4.5}$$

. We have assumed g to be the gradient of a scalar so that curl g $= 0$. Using Eq. (4.4) we replace $du/dt - g$ with the equivalent expression div σ/ρ:

$$\rho \, \text{curl} \left(\frac{du}{dt} \right) = - \frac{1}{\rho} \text{grad } \rho \times (\text{div } \sigma) + \text{curl}(\text{div } \sigma). \tag{4.6}$$

Now a very general form of the vorticity becomes,

$$\frac{d\omega}{dt} = \underbrace{\text{L}\omega}_{\text{Stretching and tilting}} - \underbrace{\frac{1}{\rho^2} \text{grad } \rho \times \text{div } \sigma}_{\text{Density gradient-net force}} + \underbrace{\frac{1}{\rho} \text{curl}(\text{div } \sigma)}_{\text{Surface forces}}. \tag{4.7}$$

In this compact form, we can interpret the physical significance of the three terms on the right hand side of Eq. (4.7). The first term on the right represents vorticity production from stretching and tilting of vorticity. The second term represents modification and creation of vorticity due to the misalignment of the vector div σ and the density gradient vector. Physically this means that vector representing the net surface forces per unit volume responsible for imparting linear acceleration to a fluid element, div σ are not aligned with the density gradient. The third term represents the net torque imparted on a fluid element due to surface forces alone. This term does not require a density gradient to affect the vorticity. Whether the second and third term create vorticity from an irrotational flow or not depends on the constitutive hypothesis we choose to model the response of the fluid. For

example in a homogeneous, isochoric Newtonian fluid, the divergence of the Cauchy stress becomes

$$\text{div}\,\sigma = -\,\text{grad}\,p + \mu\,\text{div}\,\text{grad}\,u. \tag{4.8}$$

which when substituted into Eq. (4.1) yields the Navier-Stokes equation for a homogeneous fluid:

$$\rho\frac{du}{dt} = -\,\text{grad}\,p + \mu\,\text{div}\,\text{grad}\,u + \rho g. \tag{4.9}$$

As discussed earlier the curl of this equation results in Eq. (4.2) from which vorticity cannot be created *ab nihilo*.

For non constant μ an extra term appears in Eq. (4.9):

$$\text{div}\,\sigma = -\,\text{grad}\,p + \mu\,\text{div}\,\text{grad}\,u + 2\mathbf{D}\,\text{grad}\,\mu. \tag{4.10}$$

In terms of the vorticity Eq. (4.10) becomes,

$$\text{div}\,\sigma = -\,\text{grad}\,p - \mu\,\text{curl}\,\omega + 2\mathbf{D}\,\text{grad}\,\mu. \tag{4.11}$$

The variable viscosity adds a new term when compared to the usual Navier-Stokes equations given for homogeneous fluids:

$$\rho\frac{du}{dt} = -\,\text{grad}\,p + \mu\,\text{div}\,\text{grad}\,u + 2\mathbf{D}\,\text{grad}\,\mu + \rho g. \tag{4.12}$$

D. D. Joseph and T. Y. Liao (1994) suggests the curl of this new term imparts a local torque by surmising that since the equation of motion in this form will not admit a potential flow solution, local torques must be imparted to create vorticity.

Density gradient viscosity gradient coupling: general case

In the following two sections we will substitute the general form of the Cauchy stress divergence into Eq. (4.7) and discuss the vorticity equation in a general sense. That is, we will not specialize the equations to a thin interface.

We begin the derivation by examining the second term on the right of Eq. (4.7). Substituting Eq. (4.11) into Eq. (4.7) gives

$$\frac{1}{\rho^2} \operatorname{grad} \rho \times \operatorname{div} \boldsymbol{\sigma} = \frac{\operatorname{grad} \rho \times \operatorname{grad} p}{\rho^2}$$

$$+ \frac{\operatorname{grad} \rho \times \nu \operatorname{curl} \boldsymbol{\omega}}{\rho}$$

$$- \frac{2 \operatorname{grad} \rho \times (\mathbf{D} \operatorname{grad} \mu)}{\rho^2}. \qquad (4.13)$$

The first term of Eq. (4.13) represents baroclinic torques, which have been well studied in the literature (Green, 1995; Saffman, 1992). The second term represents a modification to the viscous diffusion of momentum. The last term is a coupling of the density and dynamic viscosity gradients through the rate-of-strain tensor. This is a true production term in the sense that its kinematics are only dependent on the irrotational portion of the velocity gradient decomposition $\mathbf{D}$. Thus, even for an initially irrotational flow $\mathbf{D}$ will have a nonzero value and vorticity may be created.

To illustrate the coupling effect of this term we consider the following simple example. For simplicity we will use rectangular Cartesian coordinates chosen in such a way that the basis vectors $(\mathbf{e}_1, \mathbf{e}_2, \mathbf{e}_3)$ are instantaneously aligned with the principal axes of $\mathbf{D}$. Writing $\mathbf{D}$ in spectral form,

$$\mathbf{D} = \sum_{i=1}^{3} \lambda_i \mathbf{e}_i \otimes \mathbf{e}_i. \qquad (4.14)$$

The viscosity gradient is assumed to be directed along a unit vector $\mathbf{t}$ which makes an angle α with $\mathbf{e}_1$. The viscous density gradient coupling term now becomes,

$$= 2 \frac{\operatorname{grad} \rho}{\rho^2} \times \left(\sum_{i=1}^{3} \lambda_i \mathbf{e}_i \otimes \mathbf{e}_i \right) \operatorname{grad} \mu$$

$$= 2 \frac{1}{\rho^2} \left(\sum_{i=1}^{3} \lambda_i (\mathbf{e}_i \cdot \operatorname{grad} \mu) \operatorname{grad} \rho \times \mathbf{e}_i \right). \qquad (4.15)$$

This equation shows that if the density gradient is aligned with a principal axis of strain this term will vanish since $\mathbf{e}_i \times \operatorname{grad} \rho = \pm \| \operatorname{grad} \rho \| \mathbf{e}_i \times \mathbf{e}_i = 0$.

The baroclinic torque has often been interpreted with a physical model showing how the net pressure force will not act through the mass centre of a fluid element creating a torque. We can construct an analogous example for the viscous-density coupling condition as follows. Consider a case where the viscosity gradient in an initially irrotational flow is aligned with a principal axis of rate-of-strain. If we draw a small rectangular element, the net viscous force will act through the volume centroid. If the density gradient is not aligned with the principal axis of strain, and hence is not aligned with the direction of grad μ, the mass centroid will be offset from the line of action of the force. This will create a torque. For the case where the viscosity gradient is not aligned with a principal axis of strain, an example cannot be so easily interpreted physically.

For cases where viscosity is only a function of density the coupling term becomes,

$$-2\frac{d\mu}{d\rho}\frac{\partial u}{\partial x}\frac{\|\operatorname{grad}\rho\|^2}{\rho^2}\cos\alpha\sin\alpha \qquad (4.16)$$

Curl of surface forces: general case

We must also account for the curl of the forces acting on the surface of material elements. In a homogeneous fluid this only amounts to spatial diffusion of vorticity in a manner analogous to linear momentum (Batchelor, 1967). The situation is much more complex with variable viscosity. Substituting the divergence of the Cauchy stress into the third term on the right of Eq. (4.7) gives

$$\frac{1}{\rho}\operatorname{curl}(\operatorname{div}\boldsymbol{\sigma}) = -\nu\operatorname{curl}(\operatorname{curl}\boldsymbol{\omega}) + \frac{1}{\rho}\operatorname{grad}\mu \times \operatorname{curl}\boldsymbol{\omega} + 2\operatorname{curl}(\mathbf{D}\operatorname{grad}\mu)$$

$$= \nu\operatorname{div}(\operatorname{grad}\boldsymbol{\omega}) + \frac{1}{\rho}\operatorname{grad}\mu \times \operatorname{curl}\boldsymbol{\omega} + 2\operatorname{curl}(\mathbf{D}\operatorname{grad}\mu)$$

$$(4.17)$$

after noting that curl grad p vanishes. I have not been able to work Eq. (4.7) into a simpler general form than that given above. Eq. (4.17) has been included for completeness. As noted before, D. D. Joseph and T. Y. Liao (1994) suggested the presence of viscosity gradients imparts local torques. Although not expanded upon in that paper, this mechanism must lie within the terms shown above since their paper was only in reference to fluids with viscosity gradients and no density gradients.

Vorticity equation: general case

Combining results from Eq. (4.13) and Eq. (4.17) and substituting these into Eq. (4.7) gives the general result for the vorticity equation with viscosity and density gradients:

$$\frac{d\omega}{dt} = \mathbf{L}\omega$$

$$+ \frac{\operatorname{grad}\rho \times \operatorname{grad}p}{\rho^2} + \frac{\operatorname{grad}\rho \times \nu\operatorname{curl}\omega}{\rho} - \frac{2\operatorname{grad}\rho \times (\mathbf{D}\operatorname{grad}\mu)}{\rho^2} +$$

$$+ \nu\operatorname{div}(\operatorname{grad}\omega) + \frac{1}{\rho}\operatorname{grad}\mu \times \operatorname{curl}\omega + 2\operatorname{curl}(\mathbf{D}\operatorname{grad}\mu) \qquad (4.18)$$

A similar equation appears in Mueller (1996); Green (1995) and Dutton (1995). As it stands however, these equations do provide further insight into the problem of vorticity creation at fluid interfaces. To proceed, we will make assumptions relevant to a thin interface which will let us take the calculations further. Also, we will use equations from differential geometry to assist in interpreting these equations with reference to a two dimensional surface.

4.2.2   Equations for a thin interface

Results presented in this section are necessary for the discussion to follow. Here we give results required to express our results with reference to a coordinate frame embedded in a two-dimensional surface.

Gradients of μ and ρ are needed in terms of surface coordinates. With our assumptions, the gradients of ρ and μ will only be directed normally to the surface; tangential gradients are assumed to vanish.

Both μ and ρ are scalars and their gradients can be calculated in similar ways. Since we will require higher order derivatives of μ than ρ we will only show the calculation of $\operatorname{grad}\mu$ and $\operatorname{grad}\operatorname{grad}\mu$:

$$\operatorname{grad}\mu = \frac{\partial\mu}{\partial\theta^\alpha}\mathbf{a}^\alpha + \frac{\partial\mu}{\partial\theta^3}\mathbf{n}. \qquad (4.19)$$

Remembering that tangential gradients vanish Eq. (4.19) simply becomes

$$\operatorname{grad}\mu = \frac{\partial\mu}{\partial\theta^3}\mathbf{n}. \qquad (4.20)$$

For convenience the θ^3 coordinate will be represented by η in the remaining text. This will avoid confusion between superscripts and second derivatives.

We also need an expression for grad (grad μ) in terms of surface coordinates:

$$\left(\frac{\partial \mu}{\partial \eta} n\right)_{,\alpha} \otimes a^\alpha + \left(\frac{\partial \mu}{\partial \eta} n\right)_{,3} \otimes n = \frac{\partial \mu}{\partial \eta} n_{,\alpha} \otimes a^\alpha + \frac{\partial^2 \mu}{\partial \eta^2} n \otimes n$$

$$= -\frac{\partial \mu}{\partial \eta} b^\beta_\alpha a_\beta \otimes a^\alpha + \frac{\partial^2 \mu}{\partial \eta^2} n \otimes n = -\frac{\partial \mu}{\partial \eta} b + \frac{\partial^2 \mu}{\partial \eta^2} n \otimes n \qquad (4.21)$$

where we have used Weingarten's equation once again.

We are now in a position to substitute these expressions into the general form of the vorticity equation.

4.2.3 Density gradient viscosity gradient coupling

First, we analyze the fourth term on the left of Eq. (4.18) which is a term affected by the combined effects of density and viscosity gradients. This term is converted to a form which we can analyze using the thin-interface results given above. With the aid of the identity $D = W + L^T$ the third term on the right of Eq. (4.13) becomes

$$2 \, \text{grad} \, \rho \times D \, \text{grad} \, \mu$$
$$= [\text{grad} \, \rho \times (\omega \times \text{grad} \, \mu)] + 2 \, \text{grad} \, \rho \times \left(L^T \, \text{grad} \, \mu\right)$$
$$= \omega(\text{grad} \, \rho \cdot \text{grad} \, \mu) - \text{grad} \, \mu(\omega \cdot \text{grad} \, \rho)$$
$$+ 2 \, \text{grad} \, \rho \times [\text{grad}(u \cdot \text{grad} \, \mu) - \text{grad}(\text{grad} \, \mu)u]. \qquad (4.22)$$

In terms of surface coordinates:

$$2 \, \text{grad} \, \rho \times D \, \text{grad} \, \mu = \frac{\partial \rho}{\partial \eta} \frac{\partial \mu}{\partial \eta} [(\omega - \omega n) - 2(u_{,\alpha} a^\alpha + bu)] \times n$$

$$= \frac{\partial \rho}{\partial \eta} \frac{\partial \mu}{\partial \eta} [\omega_t + 2(n \times \dot{n})] \qquad (4.23)$$

We now write Eq. (4.13) as

$$\frac{1}{\rho^2} \text{grad} \, \rho \times \text{div} \, \sigma =$$

$$\boxed{\frac{\partial \rho}{\partial \eta} \frac{n \times \text{grad}_{\mathscr{S}} p}{\rho^2} + \frac{\nu}{\rho} \text{grad} \, \rho \times \text{grad} \, \omega + \frac{1}{\rho} \frac{\partial \rho}{\partial \eta} \frac{\partial \mu}{\partial \eta} [\omega_t + 2(n \times \dot{n})]} \qquad (4.24)$$

Here we see the appearance of the baroclinic torques in terms of density gradients through the surface and tangential pressures gradients. Also the rotation rate of the surface normal is evident.

4.2.4 Curl of surface forces

It remains to calculate the third term on the right of Eq. (4.7) which represents local torques created by viscosity gradients alone. We begin this derivation by writing the Cauchy stress in the convenient form

$$\text{div } \sigma = -\text{grad } p + \mu \text{ div grad } u + 2\mathbf{W} \text{ grad } \mu + 2\mathbf{L}^{\mathbf{T}} \text{ grad } \mu. \tag{4.25}$$

Here we have used the identity $\mathbf{D} = \mathbf{W} + \mathbf{L}^{\mathbf{T}}$ once more. Also, the last term on the right of Eq. (4.25) may be rewritten as,

$$2\,\text{grad}(u \cdot \text{grad } \mu) - 2\,[\text{grad}(\text{grad } \mu)]^{\mathbf{T}}\, u. \tag{4.26}$$

Using the identity

$$2\mathbf{W}\mathbf{a} = \omega \times \mathbf{a} \tag{4.27}$$

and Eq. (E.15) we rewrite Eq. (4.25) as

$$
\begin{aligned}
\text{div } \sigma &= \text{grad}[2(u \cdot \text{grad } \mu) - \text{p}] &\qquad \text{Term I} \\
&\quad - \mu \,\text{curl}\,\omega &\qquad \text{Term II} \\
&\quad + \omega \times \text{grad } \mu &\qquad \text{Term III} \\
&\quad - 2[\text{grad}(\text{grad } \mu)]^{\mathbf{T}}u &\qquad \text{Term IV.}
\end{aligned} \tag{4.28}
$$

Term I

The first term is the gradient of a scalar hence by Eq. (E.12) the curl of this term vanishes.

Term II

The second term is calculated as follows. Using Eq. (E.13), Eq. (E.15) and the solenoidal property of the vorticity field we arrive at,

$$-\text{curl}(\mu \,\text{curl}\,\omega) = \text{curl}\,\omega \times \text{grad } \mu + \mu \,\text{div grad}\,\omega \tag{4.29}$$

To gain further insight into the character of the first term on the right of Eq. (4.29) we note that $\operatorname{grad}\mu$ is the axial vector of the skew symmetric tensor formed by the tensor gradient of ω and its transpose. So with an obvious change in notation to Eq. (4.27) we can write,

$$\operatorname{curl}\frac{\omega}{2} \times \operatorname{grad}\mu = \frac{1}{2}(\operatorname{grad}\omega\operatorname{grad}\mu - \operatorname{grad}\omega^{\mathrm{T}}\operatorname{grad}\mu). \tag{4.30}$$

Now with,

$$(\operatorname{grad}\omega)^{\mathrm{T}}\operatorname{grad}\mu = \operatorname{grad}(\omega\cdot\operatorname{grad}\mu) - \operatorname{grad}(\operatorname{grad}\mu)^{\mathrm{T}}u \tag{4.31}$$

Term II becomes,

$$-\mu\operatorname{curl}\omega =$$

$$\boxed{\frac{\partial\mu}{\partial\eta}(\operatorname{grad}\omega)n - \frac{\partial\mu}{\partial\eta}\operatorname{grad}(\omega\cdot n) - \frac{\partial\mu}{\partial\eta}b\omega + \frac{\partial^2\mu}{\partial\eta^2}(n\cdot\omega)n + \mu\operatorname{div}\operatorname{grad}\omega}$$

$$\tag{4.32}$$

Term III

We turn our attention to the third term. With use of Eq. (E.14) and $\operatorname{div}\omega = 0$ Term III becomes

$$\operatorname{curl}(\omega\times\operatorname{grad}\mu) = \frac{\partial\mu}{\partial\eta}\operatorname{grad}\omega n - [\operatorname{grad}(\operatorname{grad}\mu)]\omega + \operatorname{div}\operatorname{grad}\mu\omega. \tag{4.33}$$

Now substituting Eq. (4.21) yields,

$$\operatorname{curl}(\omega\times\operatorname{grad}\mu) = \frac{\partial\mu}{\partial\eta}(\operatorname{grad}\omega)n + \frac{\partial\mu}{\partial\eta}b\omega - \frac{\partial^2\mu}{\partial\eta^2}(n\cdot\omega)n + (\operatorname{div}\operatorname{grad}\mu)\omega$$

$$\tag{4.34}$$

Calculating $\operatorname{div}\operatorname{grad}\mu$ is straightforward since $\operatorname{div}\operatorname{grad}\mu = \operatorname{tr}\operatorname{grad}\operatorname{grad}\mu$. Carrying out this manipulation with the aid of Eq. (4.21) gives the following:

$$\operatorname{div}\operatorname{grad}\mu = -2H\frac{\partial\mu}{\partial\eta} + \frac{\partial^2\mu}{\partial\eta^2}, \tag{4.35}$$

see for example Kosiński (1986). Now Eq. (4.34) becomes

$$\operatorname{curl}(\omega\times\operatorname{grad}\mu) =$$

$$- \boxed{\frac{\partial\mu}{\partial\eta}(\operatorname{grad}\omega)n + \frac{\partial\mu}{\partial\eta}b\omega - 2H\frac{\partial\mu}{\partial\eta}\omega + \frac{\partial^2\mu}{\partial\eta^2}\omega - \frac{\partial^2\mu}{\partial\eta^2}(n\cdot\omega)n.} \tag{4.36}$$

Term IV

The fourth term is the by far the most difficult to manipulate into a useful form. The most convenient method seems to be to write this term in summation notation and calculate the curl directly. Note that we have temporarily omitted the leading factor of 2 here for simplicity during the calculation. This factor is reintroduced in the final form of the equations which appear in boxes.

$$\text{curl}[\text{grad}(\text{grad}\,\mu)u] = \text{curl}\left[\left(-\frac{\partial\mu}{\partial\eta}b^{\alpha}_{\beta}u_{\alpha}\right)a^{\beta} + \text{curl}\left(\frac{\partial^2\mu}{\partial\eta^2}u\right)n\right] \quad (4.37)$$

Directly taking the curl of Eq. (4.37) gives the following four terms to differentiate:

$$a^{\gamma} \times \left(-\frac{\partial\mu}{\partial\eta}b^{\alpha}_{\beta}u_{\alpha}a^{\beta}\right)_{,\gamma} \qquad\qquad \text{Term IV(a)}$$

$$+\, n \times \left(-\frac{\partial\mu}{\partial\eta}b^{\alpha}_{\beta}u_{\alpha}a^{\beta}\right)_{,\eta} \qquad\qquad \text{Term IV(b)}$$

$$+\, a^{\gamma} \times \left(\frac{\partial^2\mu}{\partial\eta^2}un\right)_{,\gamma} \qquad\qquad \text{Term IV(c)}$$

$$+\, n \times \left(\frac{\partial^2\mu}{\partial\eta^2}un\right)_{,\eta} \qquad\qquad \text{Term IV(d)} \qquad (4.38)$$

Term IV(a)

We begin with

$$-a^{\alpha} \times \left(\frac{\partial\mu}{\partial\eta}b^{\alpha}_{\beta}u_{\alpha}a^{\beta}\right)_{,\gamma}$$

$$= \frac{\partial\mu}{\partial\eta}\left[\left(b^{\alpha}_{\beta}u_{\alpha,\gamma}\right) - b^{\alpha}_{\delta}u_{\alpha}\Gamma^{\delta}_{\beta\gamma}\right]a^{\beta} \times a^{\gamma}$$

$$-\frac{\partial\mu}{\partial\eta}\left(b^{\beta}_{\gamma}b^{\alpha}_{\beta}u_{\alpha}\right)a^{\gamma} \times n \quad (4.39)$$

where we have used Gauss's equation and have continued the assumption $(\frac{\partial \mu}{\partial \eta})_{,\gamma} = 0$. We can rewrite Eq. (4.39) as

$$- \mathbf{a}^\alpha \times \left(\frac{\partial \mu}{\partial \eta} b_\beta^\alpha u_\alpha \mathbf{a}^\beta \right)_{,\gamma} =$$

$$\frac{\partial \mu}{\partial \eta} \left[(b_\beta^\alpha u_\alpha) \big|_\gamma \right] \varepsilon^{\beta\gamma} \mathbf{n} - \frac{\partial \mu}{\partial \eta} \mathbf{b}(\mathbf{b}\mathbf{u}) \times \mathbf{n} \quad (4.40)$$

We may simplify this expression somewhat by expanding the covariant derivative $(b_\beta^\alpha u_\alpha)|_\gamma = b_\beta^\alpha|_\gamma u_\alpha + b_\beta^\alpha u_\alpha|_\gamma$ and using the Mainardi-Codazzi formulae $b_{\alpha\beta}|_\gamma = b_{\alpha\gamma}|_\beta$ (Kreyszig, 1991, p. 226) We are left with a form useful for our final result,

$$- \mathbf{a}^\alpha \times \left(\frac{\partial \mu}{\partial \eta} b_\beta^\alpha u_\alpha \mathbf{a}^\beta \right)_{,\gamma} =$$

$$\boxed{2 \frac{\partial \mu}{\partial \eta} \varepsilon^{\beta\gamma} \left(b_\beta^\alpha u|_\gamma \right) \mathbf{n} - 2 \frac{\partial \mu}{\partial \eta} \mathbf{b}(\mathbf{b}\mathbf{u}) \times \mathbf{n}.} \quad (4.41)$$

Term IV(b)

Calculating Term IV(b) is straightforward differentiation of the following term,

$$\mathbf{n} \times \left(-\frac{\partial \mu}{\partial \eta} b_\beta^\alpha u_\alpha \mathbf{a}^\beta \right)_{,\eta} \quad (4.42)$$

After noting $b_{\beta,\eta}^\alpha = \mathbf{a}^\beta_{,\eta} = 0$ we arrive at,

$$\mathbf{n} \times \left(-\frac{\partial \mu}{\partial \eta} b_\beta^\alpha u_\alpha \mathbf{a}^\beta \right)_{,\eta} = \boxed{-2 \left(\frac{\partial^2 \mu}{\partial \eta^2} b_\beta^\alpha u_\alpha - \frac{\partial \mu}{\partial \eta} b_\beta^\alpha u_{\alpha,3} \right) \mathbf{n} \times \mathbf{a}^\beta} \quad (4.43)$$

Term IV(c)

This is another straightforward calculation which follows,

$$\mathbf{a}^\alpha \times \left(\frac{\partial^2 \mu}{\partial \eta^2} u \mathbf{n} \right)_{,\gamma} = \frac{\partial^2 \mu}{\partial \eta^2} u_{,\gamma} \mathbf{a}^\gamma \times \mathbf{n} - \frac{\partial^2 \mu}{\partial \eta^2} u b_{\alpha\beta} \mathbf{a}^\gamma \times \mathbf{a}^\alpha \quad (4.44)$$

After noticing

$$b_{\alpha\beta}\mathbf{a}^\gamma \times \mathbf{a}^\alpha = \varepsilon^{\gamma\alpha}b_{\alpha\gamma}\mathbf{n} = 0 \qquad (4.45)$$

since $b_{\alpha\beta}$ is symmetric. This leaves

$$\mathbf{a}^\alpha \times \left(\frac{\partial^2\mu}{\partial\eta^2}u\mathbf{n}\right)_{,\eta} = \boxed{2\frac{\partial^2\mu}{\partial\eta^2}u_{,\gamma}\mathbf{a}^\gamma \times \mathbf{n}} \qquad (4.46)$$

Term IV(d)

Finally the last term of Term IV produces a trivial result,

$$\mathbf{n} \times \left(\frac{\partial^2\mu}{\partial\eta^2}u\mathbf{n}\right)_{,\eta} = \mathbf{n} \times \mathbf{n}\left(\frac{\partial^2\mu}{\partial\eta^2}u\right)_{,\eta} + \mathbf{n} \times \mathbf{n}_{,\eta}\left(\frac{\partial^2\mu}{\partial\eta^2}u\mathbf{n}\right) = 0 \quad (4.47)$$

since $\mathbf{n} \times \mathbf{n} = 0$ and $\mathbf{n}_{,\eta} = 0$.

4.2.5 The vorticity equation at a thin interface

The terms in their final form for our use, have been enclosed by boxes: Eq. (4.24),Eq. (4.32),Eq. (4.36), Eq. (4.41),Eq. (4.43),Eq. (4.46). Making the appropriate substitution of these results into Eq. (4.7) we arrive at a general expression for the vorticity equation where a thin interface of viscosity and

density exists. We are left with:

$$\frac{d\omega}{dt} = L\omega \qquad \text{Tilting and stretching}$$

$$+ \nu \operatorname{div} \operatorname{grad} \omega \qquad \text{Vorticity diffusion}$$

$$+ \frac{\partial \rho}{\partial \eta} \frac{n \times \operatorname{grad}_{\mathscr{S}} p}{\rho^2} \qquad \text{Baroclinic torque}$$

$$- \frac{\nu}{\rho} \frac{\partial \rho}{\partial \eta} \operatorname{curl} \omega \times n \qquad \text{Density gradient momentum diffusion}$$

$$- \frac{\partial \rho}{\partial \eta} \frac{\partial \mu}{\partial \eta} \frac{\omega_t}{\rho^2} \qquad \text{Viscosity/density gradients—tangential vorticity}$$

$$+ 2\frac{\partial \rho}{\partial \eta} \frac{\partial \mu}{\partial \eta} \frac{n \times \dot{n}}{\rho^2} \qquad \text{Viscosity/density gradient coupling}$$

$$+ \frac{2}{\rho} \frac{\partial \mu}{\partial \eta} \operatorname{grad} \omega n \qquad \text{Normal derivatives of vorticity (flux)}$$

$$- \frac{1}{\rho} \frac{\partial \mu}{\partial \eta} H\omega \qquad \text{Mean curvature effect}$$

$$+ \frac{1}{\rho} \frac{\partial^2 \mu}{\partial \eta^2} \omega_t \qquad \text{Viscosity gradients—tangential vorticity}$$

$$- \frac{1}{\rho} \operatorname{grad}(\omega \frac{\partial \mu}{\partial \eta}) \qquad \text{Gradients of normal vorticity}$$

$$+ \frac{2}{\rho} \frac{\partial \mu}{\partial \eta} [n \times \mathbf{b}(\omega_t - \operatorname{grad}_{\mathscr{S}} u)] \qquad \text{First order viscosity derivatives and curvature}$$

$$- \frac{2}{\rho} \frac{\partial^2 \mu}{\partial \eta^2} (n \times \dot{n}) \qquad \text{Viscosity derivatives and rotation}$$

$$- \frac{2}{\rho} \frac{\partial \mu}{\partial \eta} b^{\alpha}_{\beta} u_{\alpha}|_{\gamma} \epsilon^{\beta\gamma} n \qquad \text{Curvature effects on normal vorticity .}$$

$$\text{(4.48)}$$

There are of course, several new terms which appear when compared to Eq. (4.2). We note that in the absence of viscosity gradients we are left with

$$\frac{d\omega}{dt} = L\omega + \nu \operatorname{div} \operatorname{grad} \omega + \frac{\partial \rho}{\partial \eta} \frac{n \times \operatorname{grad}_{\mathscr{S}} p}{\rho^2} - \frac{\nu}{\rho} \frac{\partial \rho}{\partial \eta} \operatorname{curl} \omega \times n. \qquad \text{(4.49)}$$

This differs from Dahm et al. (1989) by the last term on the right hand side which seems to be an oversight. This oversight does not seem to have

affected the accuracy of their numerical results, which compared well with experimental observations.

If there are no density gradients Eq. (4.48) simply becomes Eq. (4.2). This is the standard form of the vorticity equation, which would of course apply to regions removed from the thin interface, where the density and viscosity gradients are negligible.

We are primarily interested in the means by which tangential vorticity can be created from an initially irrotational flow. In this case $\omega = 0$ and Eq. (4.48) reduces to:

$$\frac{\partial \omega}{\partial t} =$$

$$\underbrace{+\frac{\partial \rho}{\partial \eta}\frac{n \times \mathrm{grad}_{\mathscr{S}}\, p}{\rho^2} + \frac{2}{\rho}\frac{\partial \mu}{\partial \eta}(n \times b\,\mathrm{grad}_{\mathscr{S}} u) + 2\frac{\partial \rho}{\partial \eta}\frac{\partial \mu}{\partial \eta}\frac{n \times \dot{n}}{\rho^2} - \frac{2}{\rho}\frac{\partial^2 \mu}{\partial \eta^2}(n \times \dot{n})}_{\text{tangential}}$$

$$\underbrace{- \frac{2}{\rho}\frac{\partial \mu}{\partial \eta}b_\beta^\alpha u_\alpha|_\gamma \varepsilon^{\beta\gamma} n}_{\text{normal}} \quad (4.50)$$

Once again, terms involving $n \times \dot{n}$ enter the equation as it did in our analysis of the sharp interface. Especially important is that one of the terms does not involve any density gradients; this was one of the criteria needed for a successful model. That is, even at a sharp interface where there is no density jump, but where there is a viscosity jump, the level of vorticity must still satisfy Eq. (2.14). In the present model, creation of vorticity is predicted for surfaces with $n \neq 0$.

We must also consider whether the sign of the vorticity predicted is consistent with the sharp interface model. To do this we will need a model of the density and viscosity profile through the interface.

Previously Dahm et al. (1989) have used a step function to model the abrupt change in density across the interface . The derivative of the step function is the Dirac delta function. This is not suitable in the present case because substitution of the step function in Eq. (4.50) yields products of Dirac delta functions. The product of the delta function is undefined (Kaplan, 1984, Pg. 528). This difficulty did not arise in Dahm et al. (1989) since the authors' model of the interface did not include the effect of variable viscosity. This meant that no products of delta functions were needed. In the present case we avoid this difficulty by using a smooth function to represent

the change in μ and ρ through the interface.

To determine the relative importance of the terms in Eq. (4.50) we assign a function to describe the variation in fluid properties ρ, μ across the interface. Suitable functions for our purpose are:

$$\mu(\eta) = \frac{1}{2}\left[(\mu^- + \mu^+) - (\mu^- - \mu^+)\tanh(\delta\eta)\right] \qquad (4.51)$$

$$\rho(\eta) = \frac{1}{2}\left[(\rho^- + \rho^+) - (\rho^- - \rho^+)\tanh(\delta\eta)\right] \qquad (4.52)$$

These functions represent monotonically changing fluid properties through the interface. Here, δ gives a measure of the surface thickness. Specifying very large values of δ gives a very abrupt interface.

Material continuity is automatically satisfied by our choice of the density distribution since the fluid is assumed isochoric and the density of a material particle is assumed fixed: $\dot{\rho} = 0$.

Derivatives of Eq. (4.51) with respect to η, the coordinate perpendicular to the surface, become

$$\frac{\partial\mu}{\partial\eta} = -\frac{1}{2}(\mu^- - \mu^+)\delta\,\mathrm{sech}^2(\delta\,\eta) \qquad (4.53)$$

$$\frac{\partial^2\mu}{\partial\eta^2} = (\mu^- - \mu^+)\delta^2\,\mathrm{sech}^2(\delta\,\eta)\tanh(\delta\,\eta) \qquad (4.54)$$

A plot of the fluid properties is given in Fig. 4.1 as well as the first and second derivatives. The sign of the derivatives is what is of primary interest. Eq. (4.50) is non-dimensionalized as follows. Nondimensionalized variables are denoted with a tilde.

Vorticity is nondimensionalized with a characteristic velocity U and length L:

$$\tilde{\omega} = \frac{\omega}{U/L} \qquad (4.55)$$

and time:

$$\tilde{t} = \frac{t}{L/U}. \qquad (4.56)$$

Here we assume that L and U are characteristic of the flow on a scale much larger than the interfacial thickness. Similarly for $\dot{n}$ we have

$$-\tilde{\dot{n}} = \frac{\dot{n}}{U/L}. \qquad (4.57)$$
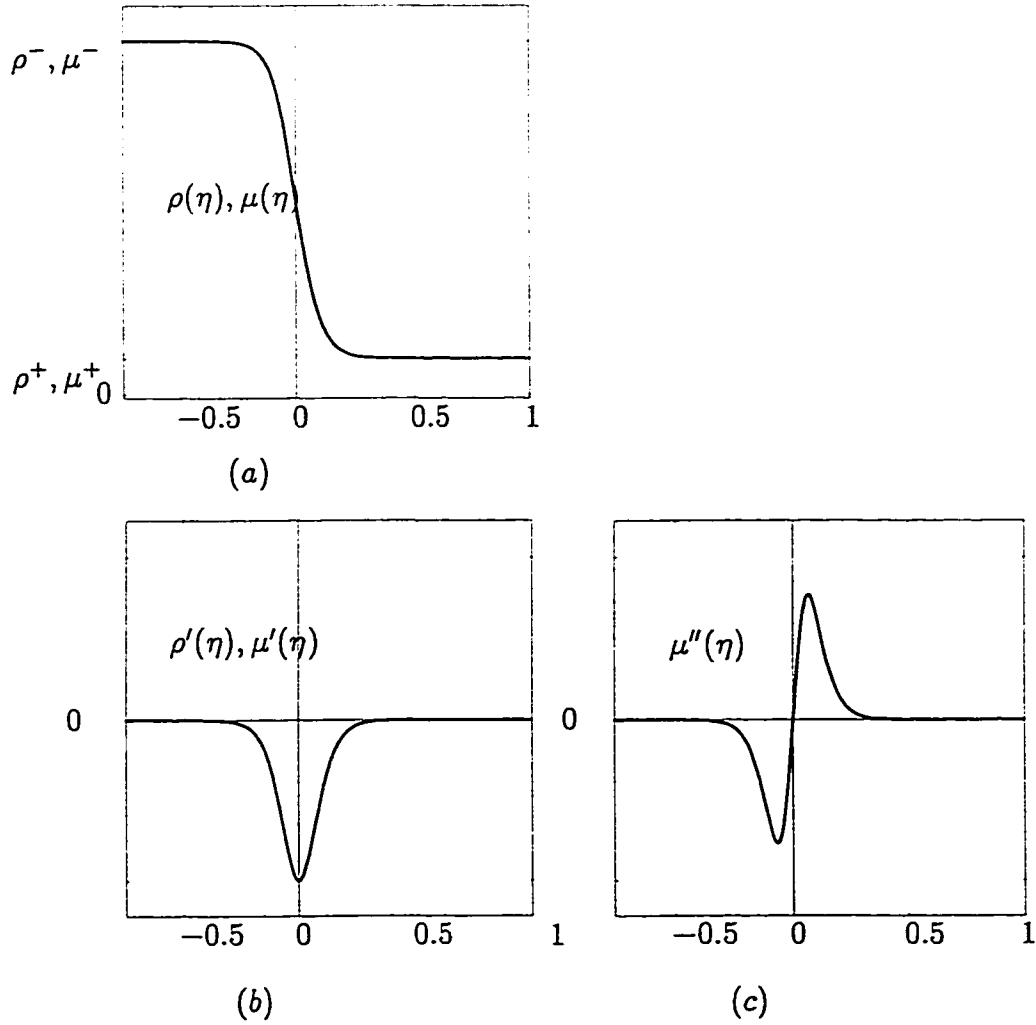
Figure 4.1: Plots of the function describing the density and viscosity through the interface.

The pressure gradient is nondimensionalized with

$$\widetilde{\mathrm{grad}_{\mathscr{S}}\, p} = \frac{\mathrm{grad}_{\mathscr{S}}\, p}{(\rho^+ + \rho^-)U^2/L}. \tag{4.58}$$

The surface gradient of u becomes:

$$\widetilde{\operatorname{grad}_{\mathscr{S}} u} = \frac{\operatorname{grad}_{\mathscr{S}} u}{U/L}. \tag{4.59}$$

Also, the following nondimensional groups are introduced:

$$A = \frac{\rho^- - \rho^+}{\rho^- + \rho^+} \qquad \text{Atwood number}$$

$$V_i = \frac{\mu^- - \mu^+}{\mu^- + \mu^+} \qquad \text{Viscosity ratio}$$

$$\varepsilon_t = \delta L \qquad \text{Thickness ratio}$$

$$Re = \frac{(\rho^- + \rho^+)UL}{\mu^- + \mu^+} \qquad \text{Reynolds number} \tag{4.60}$$

Substituting these results in Eq. (4.50) gives the following expression after a considerable amount of algebra,

$$\frac{\partial \tilde{\omega}_t}{\partial t} = \varepsilon_t \left\{ \frac{2\operatorname{sech}^2(\delta\,\eta)}{1 + A\tanh(\delta\,\eta)} \left[\frac{1}{1 + A\tanh(\delta\,\eta)} n \times \widetilde{\operatorname{grad}_{\mathscr{S}} p} + \frac{V_i}{Re} n \times \widetilde{\operatorname{grad}_{\mathscr{S}} u} \right] \right\}$$
$$\varepsilon_t^2 \left\{ \frac{2V_i \operatorname{sech}^2(\delta\eta)}{Re\,(1 + A\tanh(\delta\,\eta))} \left[\frac{A\operatorname{sech}^2(\delta\eta)}{1 + A\tanh(\delta\,\eta)} - 2\tanh(\delta\,\eta) \right] n \times \tilde{n} \right\}$$
$$\tag{4.61}$$

The first term on the right is $O(\varepsilon_t)$ while the second is $O(\varepsilon_t^2)$ and hence will dominate in view of the magnitude of ε_t. Assuming $\varepsilon_t \gg Re$, the two most important terms are the coupling of viscosity gradients and density gradients acting on n and the second derivatives of viscosity acting on n. To examine the sign of the vorticity produced by these terms we assign the functions f_1 to the coefficient of the density gradient viscosity gradient term and f_2 to the coefficient of the term involving second order viscosity gradients

$$f_1 = \frac{\varepsilon_t^2 V_i A \operatorname{sech}^4(\delta\eta)}{Re\,[1 + A\tanh(\delta\eta)]^2}$$

$$f_2 = -2\frac{\varepsilon_t^2 V_i \operatorname{sech}^2(\delta\eta)\tanh(\delta\eta)}{Re\,[1 + A\tanh(\delta\eta)]}. \tag{4.62}$$

In this form these functions nicely show the effects of net density and viscosity changes through the interface. For vanishing viscosity gradients $V_i = 0$ and
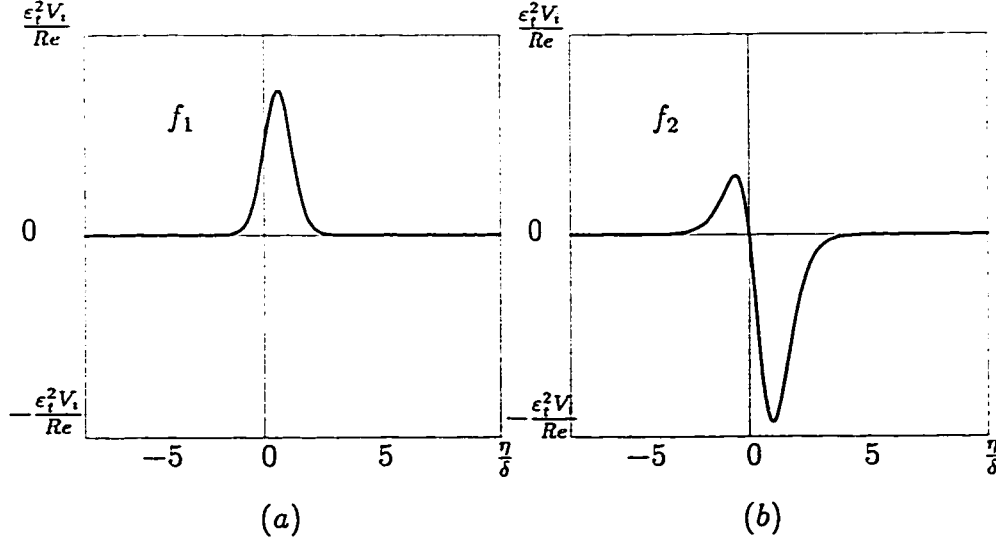
Figure 4.2: The functions f_1 and f_2. In these plots $A = V_i = 0.818$. This corresponds to $\rho^-/\rho^+ = \mu^-/\mu^+ = 10$.

both functions go to zero. For vanishing density gradient $A = 0$ so that $f_1 = 0$. The second function survives however and reduces to

$$f_2 = -2\frac{\epsilon_t^2 V_i}{Re}\,\mathrm{sech}^2(\delta\eta)\,\tanh(\delta\eta). \tag{4.63}$$

f_1 and f_2 are plotted in Fig. 4.2 for $A = V_i = 0.818$. This value was chosen arbitrarily and is not meant to represent a particular physical example. We note that f_1 is symmetric about its maxima which is slightly to the right of $\eta/\delta = 0$. This is caused by the varying value of density at each point through the interface, not the value of the density gradient which is symmetric about $\eta/\delta = 0$. f_2 is asymmetric about this point having a greater magnitude on the less viscous side of the interface. Physically this represents the greater effect of viscous torques on less dense fluid. Fig. 4.3 illustrates the effect of various A on the sum $f_1 + f_2$ which we simply refer to as f. The viscosity ratio was set to reflect that for an air-water interface so that $V_i = 0.981$. All the plots in Fig. 4.3 are symmetric about the inflection point, which shifts to the right with increasing A. Most importantly the sign of f is positive in the more dense, more viscous region. This result is consistent with what we would expect from the sharp interface analysis in Chpt. 2. Indeed f_1 and f_2 are the same sign and will act cooperatively. This also means that even
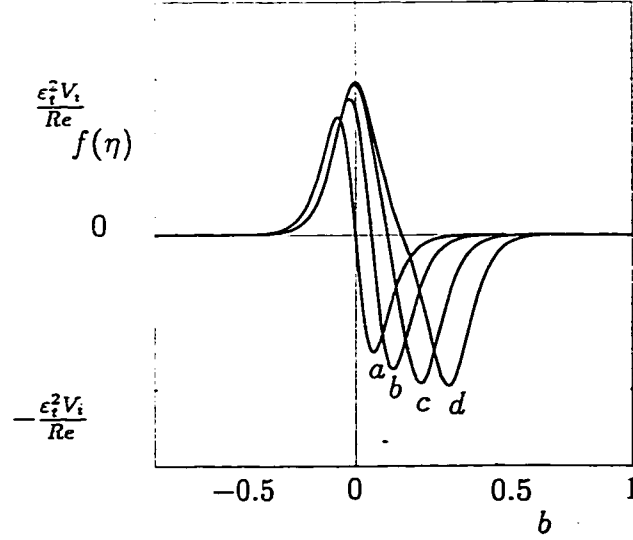
Figure 4.3: A plot of the functions from Eq. (4.61) with the following A: (a) $A = 1$; $\frac{\rho^-}{\rho^+} = 1$, (b) $A = 0.818$; $\frac{\rho^-}{\rho^+} = 10$, (c) $A = 0.980$; $\frac{\rho^-}{\rho^+} = 100$, (d)$A = 0.997$; $\frac{\rho^-}{\rho^+} = 1000$. V_i was held constant at 0.981 for all curves

if $A = 0$ the correct sign of ω_t production is predicted. This means that vorticity production of the correct sign is predicted even at the interface of two fluids of the same density but differing viscosity.

4.2.6 Conclusion

The vorticity transport equation has been derived for a thin interface through which density and viscosity are allowed to vary. This analysis yields terms that predict vorticity creation of a sign consistent with the sign of vorticity observed in experiments and predicted by the sharp-interface model Chpt. 2. These results shows that, in general, vorticity creation results from a combination of the curl of viscous forces and viscosity-gradient density-gradient coupling. The analysis leading to Eq. (4.61) shows that baroclinic torques are likely secondary to the viscosity-dependent contributions.

This analysis also successfully fulfills another criterion stated at the outset: The creation of vorticity is predicted at an interface where there is solely

a viscosity gradient. As discussed in Chpt. 2, the sharp interface model with vanishing tangential surface tractions—the free-surface model—requires a prescribed level of vorticity to match this boundary conditions independent of the density jump across the surface.

A deficiency in this chapter's analysis is the absence of surface tension effects. This may not be such a bad assumption however. As Saffman (1992) points out, the effect of a constant surface tension is an application of a force normal to the surface. He states, without analysis, that such a force will not create a local torque on fluid elements at the surface. As we saw in Chpt. 2 the effects of constant surface tension did not appear—only the presence of surface tension gradients altered the level of vorticity. The effects of intrinsic surface stress on the vorticity equation remains to be calculated. Papers recently brought to my attention (Mavrovouniotis and Brenner, 1993; Mavrovouniotis et al., 1993) may offer future directions for this work which I hope to pursue.

Since we are assuming the interface to be a thin region we cannot include a singular surface with an intrinsic surface stress such as surface tension. Modelling surface tension in the thin interface context would require an alternative constitutive response to include this effect. Some models of surface tension effects in the context of a thin interface do exist (Dunn and Serrin, 1983; Blinowski, 1973b,a). Here, they find that surface tension arises as a manifestation of steep density gradients through the interface. It would be worthwhile to investigate the implications of these equations in the future.

Bibliography

Leonid K. Antanovskii. A phase field model of capillarity. *Phys. Fluids*, 7 (4):747–753, April 1995.

G.R. Baker. *Waves on Fluid Interfaces*, chapter Generalized Vortex Methods for Free-Surface Flows, pages 53–81. Academic Press, 1983.

Gregory. R. Baker, Daniel I. Meiron, and Steven A. Orszag. Vortex simulations of the Rayleigh-Taylor instability. *Phys. Fluids*, 23(8):1485–1490, August 1980.

Gregory. R. Baker, Daniel I. Meiron, and Steven A. Orszag. Boundary integral methods for axisymmetric and three-dimensional Rayleigh-Taylor instability problems. *Physica*, 12:19–31, 1984.

G. K. Batchelor. *An Introduction to Fluid Dynamics*. Cambridge University, New York, 1967.

A. Blinowski. On the order of magnitude of the gradient-of-density dependent part of the elastic potential in liquids. *Arch. Mech.*, 25, 1973a.

A. Blinowski. On the surface behaviour of gradient-sensitive liquids. *Arch. Mech.*, 25:259–268, 1973b.

Alexandre J. Chorin. *Vorticity and Turbulence*. Springer-Verlag, New York, 1994.

D. D. Joseph and T. Y. Liao. Potential flows of viscous and viscoelastic fluids. *J. Fluid Mech.*, 265:1–23, 1994.

Werner J. A. Dahm, Christine M.Scheil, and Grétar Tryggvason. Dynamics of vortex interaction with a density interface. *J. Fluid Mech.*, 205:1–43, 1989.

J. E. Dunn and J. Serrin. On the thermomechanics of interstitial working. *Institute for Mathematics and its Application*, 1983.

John A. Dutton. *Dynamics of Atmospheric Motion*. Dover, 1995.

Sheldon I. Green. *Fluid Vortices*, chapter Introduction to Vorticity. Kluwer Academic, 1995.

Harold Jeffreys. The equations of viscous motion and the circulation theorem. *Proc. Cambridge Phil. Soc.*, 24:477–479, 1928.

Wilfred Kaplan. *Advanced Calculus*. Addison Wesley, 1984.

J. Koplik and J. R. Banavar. Continuum deductions from molecular hydrodynamics. *Annu. Rev. Fluid Mech.*, 27:1–50, 1994.

W Kosiński. *Field Singularities and Wave Analysis in Continuum Mechanics*. John Wiley and Sons, New York, 1986.

Erwin Kreyszig. *Differential Geometry*. Dover, New York, 1991.

G. M. Mavrovouniotis and H. Brenner. A micromechanical investigation of interfacial transport processes: I. interfacial conservation equations. *Phil. Trans. Roy. Soc.*, A345:165–207, 1993.

G. M. Mavrovouniotis, H. Brenner, D. A. Edwards, and L. Ting. A micromechanical investigation of interfacial transport processes: II. interfacial constitutive equations. *Phil. Trans. Roy. Soc.*, A345:209–228, 1993.

B. R. Morton. The generation and decay of vorticity. *Geophys. Astrophys. Fluid Dynamics*, 28:277–308, 1984.

Charles J. Mueller, James Driscoll, David L. Reuss, Michael C. Drake, and Martin E. Rosalik. Generation and attenuation of vorticity by flames: Measured vorticity field time evolution during a premixed flame-vortex interaction'. *Submmitted to: Combustion and Flame*, 1997.

Charles Jeffrey Mueller. *Measurements of Flame-Vortex Interaction Dynamics and Chemistry*. PhD thesis, University of Michigan, Aerospace Engineering, 1996.

Bill Peck and Lorenz Sigurdson. The creation of vorticity at fluid interfaces. In *Proceedings of the American Physical Society*. American Physical Society, 1996.

P. G. Saffman. *Vortex Dynamics*. Cambridge University Press, New York, 1992.

C. Truesdell. The effect of viscosity on circulation. *J. Meteorol.*, 6:61–62, February 1949.

C. Truesdell. *The Kinematics of Vorticity*. Indiana University, Bloomington, Indiana, 1954.

Serge J. Zarodny and Michael D. Greenberg. On a vortex sheet approach to the numerical calculation of water waves. *J. Comput. Phys.*, 11:440–446, 1973.

PART II

DROP-FORMED VORTEX RING EXPERIMENTS

CHAPTER 5

THE VORTEX RING VELOCITY DUE TO AN IMPACTING DROP

5.1 Introduction

The experiment studied here is a result of a remarkably simple and ubiquitous event. A water drop falls freely through air and strikes a pool of the same liquid. If the Weber number (We) and Froude number (Fr) are not too great, a vortex ring forms within the pool, (Hsiao et al., 1988). We and Fr are defined as follows,

$$We = \frac{\rho U^2 d_e}{\gamma}, \quad Fr = \frac{U^2}{g d_e}.$$

Here γ is the surface tension, ρ the density of water, g is the acceleration due to gravity, U the velocity of the drop and d_e is the drop's effective diameter (d_e will be defined in section Sec. 5.3).

The purpose of the present chapter is to investigate the properties of the vortex ring resulting from two cases. In the first case (Case 1) the drop impacts the pool with a We of 23.2 and Fr of 25.2. In the second case (Case 2) the drop's We is 16.6 and the Fr is 18. In this regime the impacting drop was found to produce an intricate three-dimensional vortex structure, (Peck and Sigurdson, 1994). It was the study of this structure which led to the present experiments. This phenomena was studied experimentally using dyed water drops falling into an un-dyed test cell of water. The evolution of the vortex ring was examined for short times after its formation. This corresponds to

---

†This chapter has appeared in Experiments in Fluids: Peck and Sigurdson (1995)

times less than 70 ms after the drop and cell first come into contact with each other. The specific topics to be addressed in this chapter will be:

1. The position of the vortex ring relative to the undisturbed free-surface during the times mentioned.

2. The growth of the vortex ring's spatial dimensions.

3. The velocity of the vortex ring.

Previously published data, (Rodriguez and Mesler, 1988), are compared to the present data to investigate the validity of a major proposition of the present chapter; the appropriate time-scale is the time for the impact crater to reach its maximum depth. This endeavour makes use of a scaling for this time suggested by Pumphrey's experiments, reported and developed in Oḡuz and Prosperetti (1990).

5.1.1   An Introduction to the Problem

The experiment begins with a water drop freely falling through air. During its fall the drop will oscillate as a result of the separation of the pendant drop from the tip used to form it. If the primary mode is excited the drop will oscillate about spherical, between vertically prolate and vertically oblate. The shape of the drop at impact has been shown to influence the depth to which the vortex ring penetrates into the pool before stopping, (Thomson and Newall, 1885; Keedy, 1967; Chapman and Critchlow, 1967; Rodriguez and Mesler, 1988).

As the drop strikes the pool a vortex sheet must exist to match the discontinuous velocity potentials. In this way an axisymmetric distribution of azimuthally aligned vorticity will be present, see Fig. 5.1. The dynamical means by which the vorticity is generated is unclear[1]. Very little discussion is available in the literature. Chapman and Critchlow (1967) offer an essentially kinematic argument to explain the generation of circulation which hinges on the oscillation phase of the drop at impact. The reader is referred to Peck and Sigurdson (1994) for a more complete discussion.

---

[1]When this chapter was prepared for publication (1994), this statement reflected the state of knowledge. I believe the work in Part I of this thesis provides significant insight into this process.
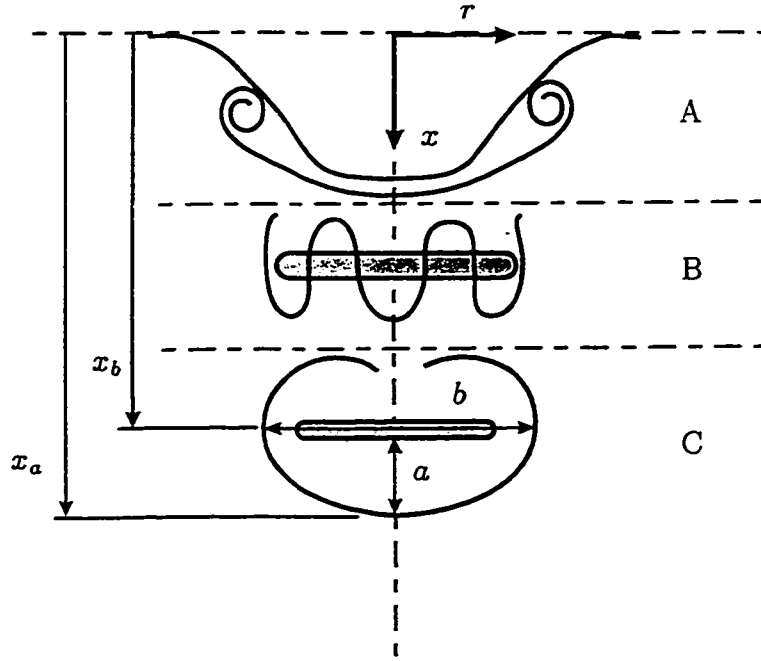
Figure 5.1: Schematic diagram of vortex structure after drop impact

It is unlikely that there is any significant contribution to the vortex dy-
namics taking place after impact from the small amount of vorticity created
within the drop during free-fall. It has been shown that in a drop-fixed frame
of reference the internal velocities are on the order of 1% of the drop velocity
after the drop has reached terminal velocity, (Pruppacher and Beard, 1987).
If the axisymmetric vortex sheet created by the impact is considered in the
absence of the free-surface it will begin to roll-up under its Biot-Savart self-
induction. A spiral forms in the x, r plane which will center about a circle
that has its plane perpendicular to, and its origin on, the axis of symmetry.
The radius of this circle will decrease until a steady value, r_1, is reached . If
the initial radius to the outer edge of the sheet is r_2 and $C = \frac{r_1}{r_2}$, C will take
on a value less than 1 in order to satisfy the invariance of the hydrodynamic

impulse, I, where,

$$I = \frac{1}{2}\rho \int_v r \times \omega dV. \tag{5.1}$$

Here r is the position vector and ω is the vorticity of the elemental volume dV. Integration is taken over the entire volume, V. The value of C is dependent on the initial radial distribution of the azimuthal vorticity (see for example Taylor (1953)). Unlike Taylor's analysis, the impulse is no longer necessarily invariant in the presence of the free-surface. For the idealized theoretical case of a steady free-surface the surface will tend to further contract the vortex sheet as the vorticity interacts with its images. The result of the vortex sheet roll-up is the vortex ring.

At this point it is important to clarify the definitions of the vortex ring and the vortex ring core which will be used. Common definitions of vortex rings range from a single circular line vortex to Hill's spherical vortex. This issue is further complicated when describing turbulent or unsteady vortex rings. The present chapter will adopt the definition of Glezer and Coles (1990); the vortex ring will be defined as "an axially symmetric, approximately spheroidal volume whose internal mean vorticity lies entirely in the azimuthal direction". In a reference frame moving with the vortex ring the spheroid is bounded by a stream-surface with a front and rear stagnation point. The vortex ring core will refer to the concentrated region of azimuthal vorticity within the vortex ring often idealized as a single circular line vortex.

The point in time when the vortex sheet becomes a vortex ring is ambiguous but occurs in the nondimensional time interval, 0 to 1.5 (using the time-scaling proposed in Sec. 5.3). This time interval will be referred to as the vortex ring formation interval (interval A shown in figures). The time intervals mentioned are not meant to represent precise boundaries. They are to aid in identifying which general flow regime the vortex ring is undergoing in the following discussions.

As the vortex ring travels downward it may undergo an instability whereby azimuthal vorticity is tilted to become stream-wise vorticity and is deposited into the wake. This is observed in the present experiments and is described in greater detail elsewhere, (Peck and Sigurdson, 1994). This will be referred to as the transition region corresponding to the nondimensional time interval, 1.5 to 3.6 (interval B shown in figures).

The vorticity that is left within the vortex ring relaminarizes and proceeds downward into the pool. This corresponds to nondimensional times greater

than 3.6 and is referred to as the relaminarized region (interval C shown in figures).

This problem has also been studied in the light of the entrainment of bubbles which act as nucleation sites for boiling, often termed Mesler entrainment, (Esmailizadeh and Mesler, 1986). The results to be presented are also relevant to the study of drop-pool mixing in the near interface region,(Anilkumar et al., 1991). It is hoped that the present quantitative results will assist in understanding these topics.

5.2 Apparatus

A schematic of the apparatus used in this experiment is shown in Fig. 5.2. A comprehensive description of the experimental apparatus has been given in Peck and Sigurdson (1994). The entire experiment was automated by a personal computer operating through a series of I/O devices. This allowed a complete set of data to be taken without the danger of disturbances from human presence.

The drops were formed on tips constructed from carefully prepared stainless steel hypodermic tubes. A small stepper-motor-actuated pump was fabricated to deliver precise amounts of fluid to the tip. The pendant drops were first quickly filled to 85 % of their predicted final volume. The rate of filling was then slowed until the weight of the pendant drop caused it to fall away from the tip. This is similar to the method used to obtain a consistently sized drop when using the drop mass technique of surface tension measurement (Wilkinson, 1972). The dye used in the drops was Fluorescein with a concentration of 400 mg per 1000 ml of distilled water. The surface tension of the Fluorescein solution was tested using the drop mass technique in a separate set of experiments using a 4.4 mm diameter glass tip prepared using the techniques outlined by Harkins and Brown (1919). Less than a 1 % difference in surface tension between the drop and the pure water of the pool were recorded.

The un-dyed pool was held within a glass vessel which had been blown from a single piece of glass. The temperature of the pool at the beginning of the experiment was $19^{\circ}C$ and rose over the course of the experiment to $21^{\circ}C$. An optically clear window was fused into one wall of the vessel to allow proper focusing of photographic equipment. The vessel and the drop forming tips were mounted on a vibration isolation table to stabilize the free
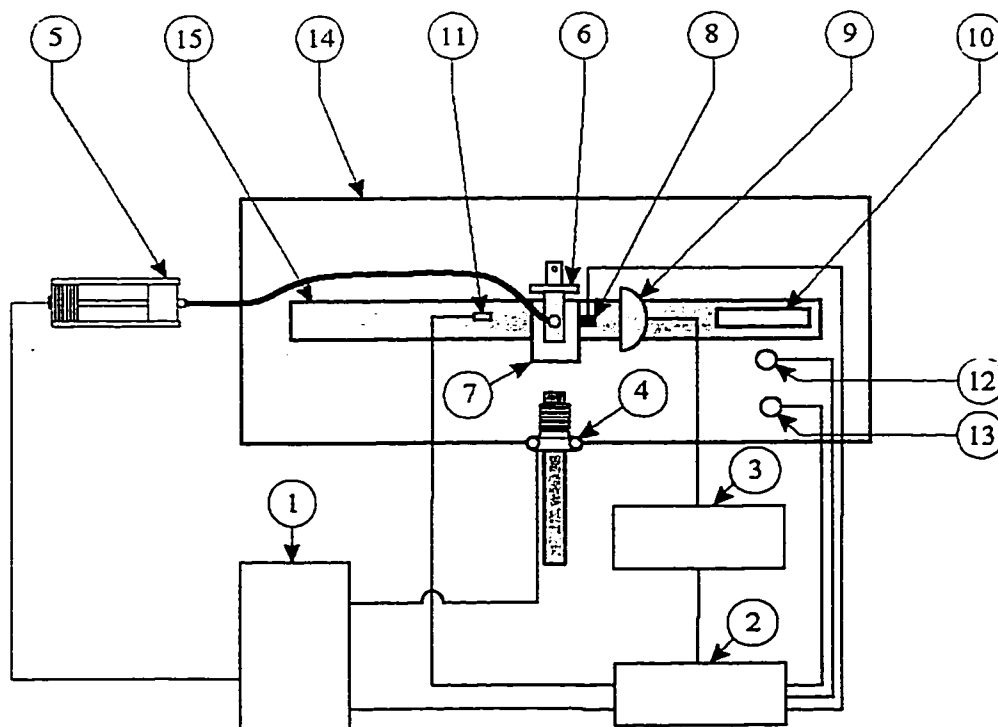
Figure 5.2: Plan view of apparatus. (1) Personal computer, (2) data acquisition/ management board, (3) function generator, (4) 35 mm camera, (5) stepper motor driven, precision pump, (6) three-axis traverse and hypodermic tube carrier, (7) test cell, (8) cell temperature probe, (9) strobolume, (10) He-Ne triggering laser, (11) photo-transistor to receive laser trigger, (12) relative humidity sensor, (13) ambient temperature sensor, (14) optical benches, (15) vibration-isolation table.

surfaces of the pool and the pendant drop. The height of fall was defined as the distance from the tip to the free surface minus two drop radii. The fall height remained constant throughout the experiments at 32.9 mm.

All of the apparatus which would come in contact with the liquids involved were constructed of stainless steel, glass or teflon. This allowed the apparatus to be cleaned using a 1:1 nitric acid solution followed by ten rinses of distilled water. This eliminated any contaminants present on the apparatus. The free surface was left open to the atmosphere. The degree to which airborne contaminants may affect the results is currently under investigation. The

photographic data were acquired with a Nikon F3 camera and 60 mm lens mounted on a bellows. A strobe was used to illuminate the event from the right side of the tank. The strobe was discharged at a rate of 66.67 bursts per second while keeping the camera shutter open in a darkened room. The flash rate was controlled by a function generator. This resulted in four or five images being reproduced on each photograph at 15 ms intervals. The time at which the first flash was triggered was controlled by a timing circuit. The circuit was activated by the falling drop intercepting a laser beam reflected off the surface of the pool. The accuracy of the timing circuit was determined to be 0.15 ms. The time for the first flash in the series to be discharged was varied for different drop impacts by 2 to 3 ms over a 15 ms range starting at 7.5 ms. In this way a complete record of the event was compiled for the first 70 ms.

5.3 Experimental Results

Twenty-eight multiple exposure photographs were taken yielding one hundred and thirty points. One of these photographs is shown in Fig. 5.3. Three distances were measured from these photographs as follows.

The depth x_b of the horizontal plane which contained the vortex ring's greatest width (henceforth referred to as the vortex ring's major axis) was measured relative to the position of the undisturbed free surface, Fig. 5.1. This measurement was the most reasonable estimate of the position of the vortex ring's core obtainable using this form of flow visualization. Examination of more detailed single exposure photographs confirmed that the center of the spirals formed from the dyed fluid sheet corresponds to the position of the vortex ring's major axis. It seems reasonable to assume that the position of the center of the vortex ring core will be close to the center of the spiral at these early times when the diffusion length of the vorticity is small.

The depth of the vortex ring's greatest penetration x_a was also measured relative to the undisturbed free surface. This was taken to be the greatest depth that dyed fluid associated with the vortex ring was visible. That position will be referred to as the depth of the vortex ring's leading edge. Care must be exercised when interpreting this result. The position of the dye does not necessarily mark the stream-surface separating the vortex ring from the outer irrotational flow. The diffusion of vorticity through the fluid is much faster than the dye. Thus while the presence of dyed fluid that was
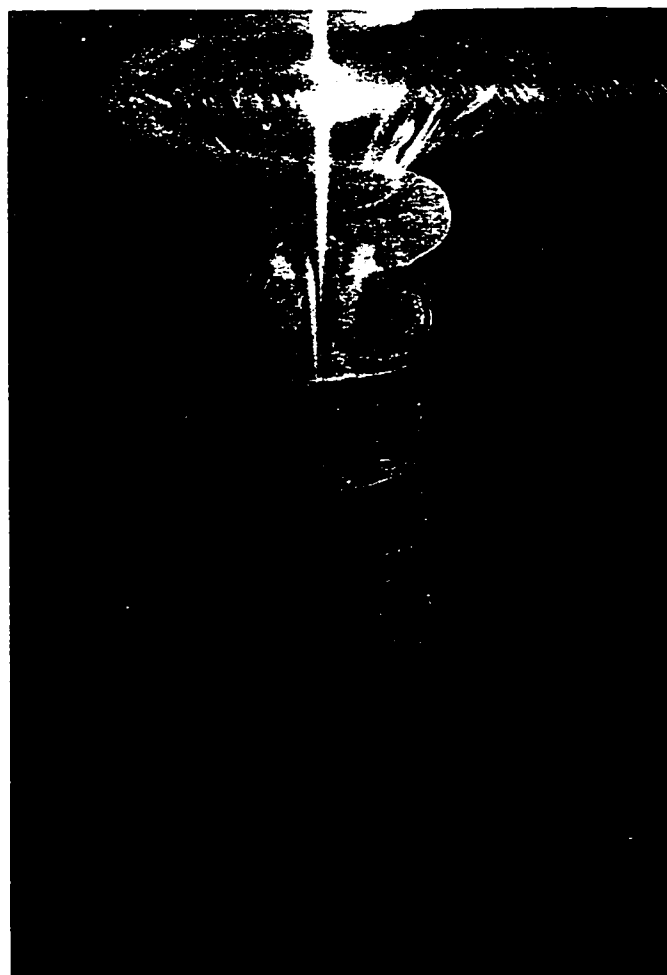
Figure 5.3: A typical multi-exposure photograph acquired in this experiment. The first flash was discharged at 17.5 ms after impact and at 15 ms intervals thereafter.

initially rotational indicates the presence of vorticity, the converse does not hold. The position of the leading edge as measured in these experiments can only give an approximate indication of the position of the front stagnation point on the bounding stream-surface. The minor axis length a will be defined as $x_a - x_b$. This is one half the length of the minor axis expected if the vortex ring were symmetrical about the horizontal plane containing the vortex ring core. Limitations of the flow visualization technique used did not allow any

accurate measurement of the rear stagnation point.

The length of the major axis b was the third measurement to be taken from the photographs. This dimension must also be treated with the same care mentioned in the preceding paragraph. At early times this length suffers in interpretation due to the highly unsteady nature of the vortex ring as it undergoes a transition to turbulence. During these times the major axis was taken to be the maximum length across which dyed fluid was observed.

The lengths were made dimensionless with the effective drop diameter, d_e. This is the diameter of a sphere which would occupy the same volume as the dyed water drop used in these experiments.

All the times appearing in the present chapter were made dimensionless with the time at which the maximum penetration depth of the crater occurs, t_m. Pumphrey has found that t_m varies as $U^{\frac{1}{3}} d_e$. Oğuz and Prosperetti (1990) suggest a dimensionless scaling which appears in that paper linking Pumphrey's experimental result with the dispersion of the impacting drop's energy via the largest wavelength capillary waves with wave-speed, c_m. This scaling did not require viscosity and hence the scaling presented here is independent of Re. Nondimensionalization yields the following result,

$$t_m = \frac{d_e}{2} U^{\frac{1}{3}} c_m^{-\frac{4}{3}}.$$

This may be written as follows $\left(\text{since} \quad c_m = \left(\frac{4g\gamma}{\rho} \right)^{\frac{1}{4}} \right)$,

$$\frac{t_m U}{d_e} = (We\, Fr\,)^{\frac{1}{3}}$$

Therefore,

$$\frac{t}{t_m} = \frac{tU}{d_e}(We\, Fr\,)^{-\frac{1}{3}}.$$

The measured time for the crater to reach its maximum depth in the present experiment was 8 ms ±.5 ms. This corresponds well with the predicted value of 8.5 ms using the above relationship. Two other cases were tested from data appearing in Rodriguez and Mesler (1988) (this publication will henceforth be referred to as RM) for 4.4 mm d_e drops falling from 17.6 mm and 27.6 mm. The predicted times were 13.0 and 14.0 ms respectively. The values taken from the published data were 12.5 and 15 ms ±1 ms in the same order.

The velocities of the vortex ring, U_v, were calculated from x_b. A centered differencing technique was used where the data was available. At the endpoints of each data set a backward or forward differencing was used as required. From multiple exposure photographs taken of the drop in free-fall it was determined that the drop struck the pool while spherical passing from vertically prolate to vertically oblate. The ratio of the major and minor axes of the drop (defined in the usual sense for an ellipse) in the fully prolate configuration just prior to impact was 1.1.

All of the results mentioned so far were dependent on the reproducibility of this delicate experiment. It is for this reason that the present method of data acquisition was used. The small scatter in the data confirms that the events studied here were reproducible and represented a specific phenomenon under these conditions.

5.4   Discussion

The position of the vortex ring's major axis and leading edge are plotted against time in Fig. 5.4, which includes data from RM (in all of the figures the open circles represent data from Case 1 while the open squares represent data from Case 2). No error bars are shown in the plots since the measurement error lies within the plotted symbols. The position of the vortex ring's major diameter is plotted in Fig. 5.5. In both Fig. 5.4 and Fig. 5.5 we see the data for the two cases agrees very well, indicating the validity of the proposed scaling. The Case 2 data appears offset slightly below the Case 1 data, which may be due to the maximum crater impact depth being slightly smaller in that case. This would be consistent with the vortex ring being created nearer the surface. The agreement between the two cases is even better for Fig. 5.5 indicating the maximum ring diameter position is a better diagnostic than the leading edge position, which can be influenced by differing individual growth rates of the vortex rings. This influence can be seen in Fig. 5.6 where the Case 1 vortices are growing slightly faster than the Case 2 vortices.

In Fig. 5.4 and Fig. 5.5 we also see that the vortex rings travel away from the free surface in a remarkably smooth manner over the entire time interval studied (in particular note the best fit line in Fig. 5.5). This is surprising when the upward flow due to the reversing impact crater (estimated to be of the same order of magnitude as U) is considered at early times (interval A). It is equally unexpected during the transition phase, B, where the vortex ring
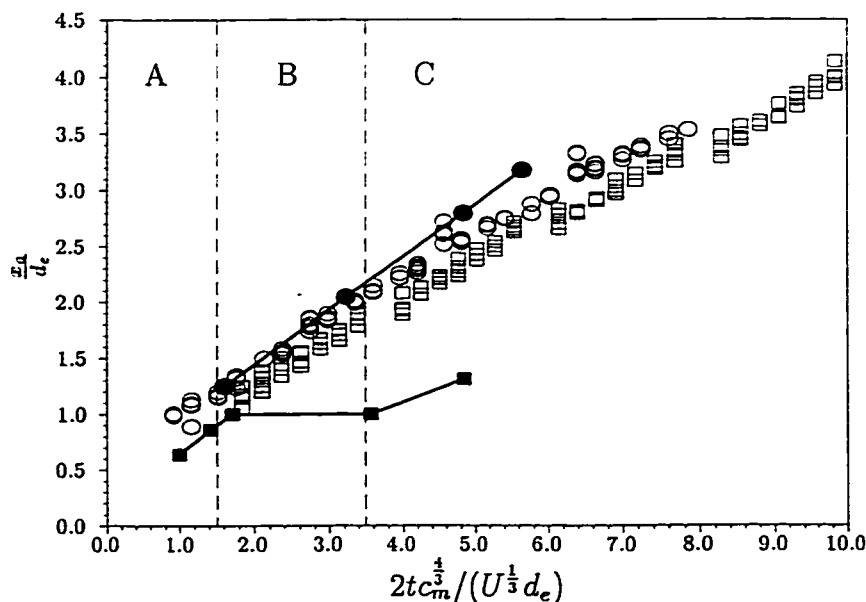
Figure 5.4: The nondimensionalized position of the vortex ring's leading edge vs nondimensional time. The open circles correspond to the depth of the leading edge in Case 1 (We =23.2, Fr =25.2). The open squares represent the depth of the leading edge in Case 2 (We =16.6, Fr = 18) The filled circles and squares are data which appear in RM for the position of the leading edge of vortex rings created by larger drops, d_e = 4.4mm, impacting the pool at different oscillation phases. The filled squares and circles correspond to drops which were vertically oblate and vertically prolate at impact, respectively. Two best fit lines are plotted in region B. The upper line is for data from Case 1, the lower line for Case 2.

undergoes dramatic topological changes. After the vortex ring has undergone transition and has shed its secondary structure into the wake the leading edge advances into the pool at a slightly greater rate than the major axis. This indicates that the leading edge is advancing away from the vortex ring's major axis. The vortex ring is growing as will be discussed later.

Data is published in RM for a drop with a d_e of 4.4 mm which had fallen 17.6 mm before striking a pool and was fully prolate at impact. The We and

Figure 5.5: The nondimensionalized position of the vortex ring's major diameter vs nondimensionalized time (see caption to Fig. 5.4 for explanation of symbols

Fr calculated in this case are near 21 and 8 respectively. The We is very close to that in Case 1. In the same publication, data were also presented for the case of a drop with the same effective diameter but impacting in the fully oblate position after falling 27.6 mm yielding a We of 31 and Fr of 12.5. These data are also shown in Fig. 5.4. The vortex rings formed from fully prolate drops in the experiments of RM scale very well with the data collected for the significantly smaller drops studied in the present experiments. This lends support to the validity of the scaling proposed here. This is not the case for the vortex rings formed from the fully oblate drops in the RM experiments. The position of x_a for the vortex rings created by fully oblate drops consistently lies behind the others discussed.

The photographs reproduced of vortex rings produced by fully prolate drops in RM's experiments also show a qualitative similarity to those studied here. In both cases the vortex rings appear to become unstable after formation and undergo a transition. This is observable if the first exposure in Fig. 5.3 of the present chapter is compared with Fig 3, frame 11 of RM. Both of these photographs correspond to nondimensional times of 2.1. The expulsion of dyed fluid into the wake is also visible in RM at later times consistent with those observed here.

The apparent similarity between the prolate drop of RM's and the smaller drops studied here and the dissimilarity of the oblate case may be due to the complex crater-vortex sheet interaction at early nondimensional times between 0 and 1. RM have suggested that the increased influence of the crater inhibits the formation of the vortex ring.

The diameter of the vortex ring was scaled using the effective drop diameter and plotted against the scaled time in Fig. 5.6. Note that it is the drops which are prolate at impact (RM, Case 2) which have similarly sized vortex rings. There is some ambiguity as to when the vortex sheet actually becomes a vortex ring. Thus, the diameters plotted at early times represent the maximum extent of the volute of dyed fluid within which the vortex sheet is embedded. It can be ascertained from Fig. 5.6 that the sheet contracts. As mentioned earlier the diameter contraction is entirely consistent with the formation of a vortex ring from a vortex sheet. In these experiments the distribution of circulation along the sheet is unknown and any attempts to estimate it are hampered by the presence of the unsteady free surface. A stationary free surface will cause a diameter reduction of a vortex ring of this sign near it due to velocities induced from its images. To what degree these effects come into play in the present unsteady case are unknown.

There is some scatter in the data during the transition phase due to the ambiguity in the measurement of the complex vortical topology.

After the transition phase the vortex ring diameter, b, is approximately 40 % larger than d_c in Case 1 and 25 % larger in Case 2. In both cases the diameter begins to increase at a slow rate. In Case 1, b grows by 6.5 % between the start of region C to 10 nondimensional time units. In Case 2, b grows by 4.5 % over the same time interval. This growth, coupled with the advancement of the leading edge away from the plane containing the major axis, implies that bulk fluid is being entrained as the vortex ring progresses through the pool. At these later times the entrainment is likely dominated by diffusive processes perhaps similar to those outlined by Maxworthy (1972).
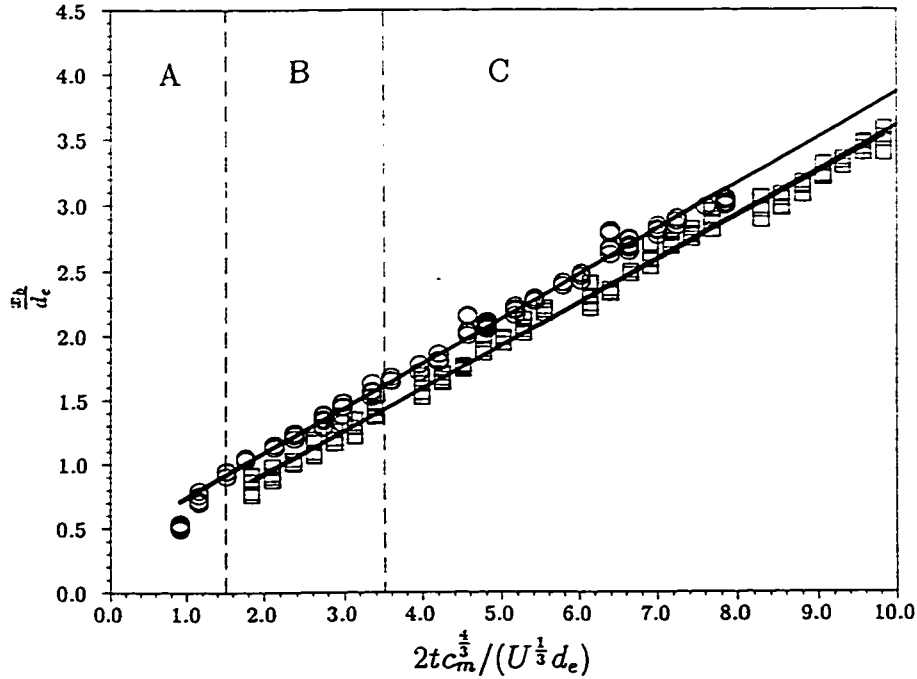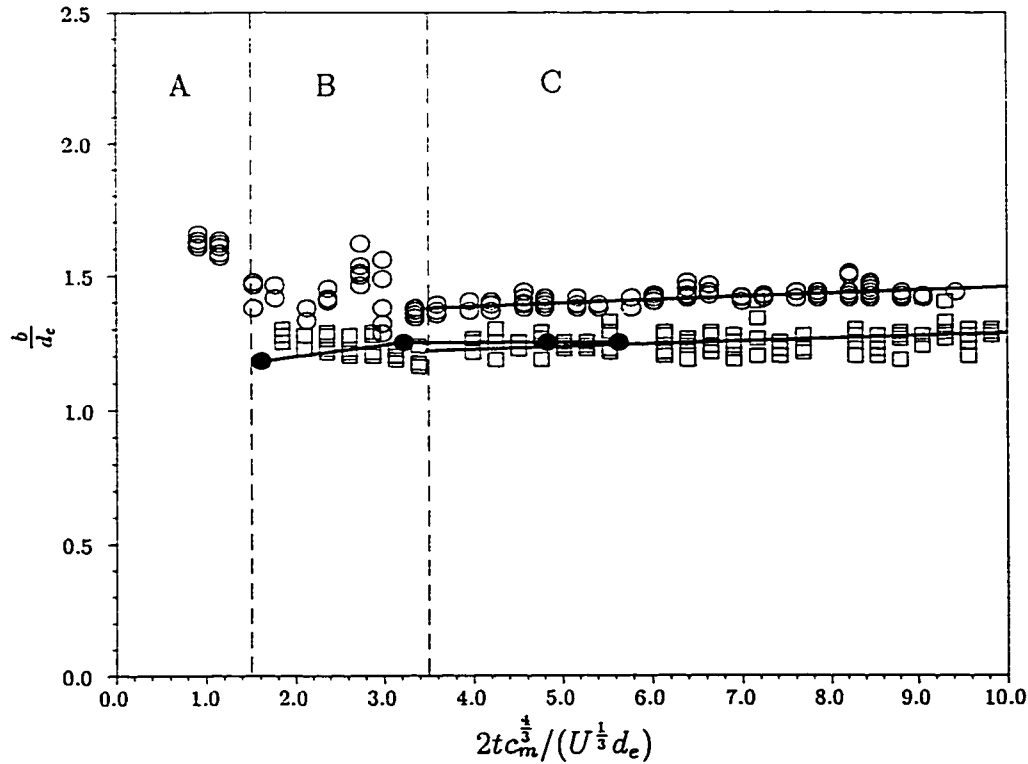
Figure 5.6: The nondimensionalized diameter of the vortex ring vs nondi-
mensionalized time (see caption to Fig. 5.4 for explanation of symbols)

At early times entrainment due to convective means is viable.

To test for self-similarity of the vortex ring, the ratio of the minor axis,
a, and one half the major axis length, $b/2$, were plotted versus time Fig. 5.7.
The ratio was approximately 0.7 for the relaminarized vortex ring, and
remained so for the times considered here, indicating self- similarity was
present. The Reynolds number (Re) of the vortex ring was calculated from
the measured velocities to be near 500 just after relaminarization. Here,

$$Re = \frac{U_v b}{\nu} \qquad (5.2)$$

where ν is the kinematic viscosity. In Case 1 the Re was 390 at the begin-
ning of the region C, the start of the relaminarization region, and decreased
to 360 by eight nondimensional time units. For Case 2 the respective values
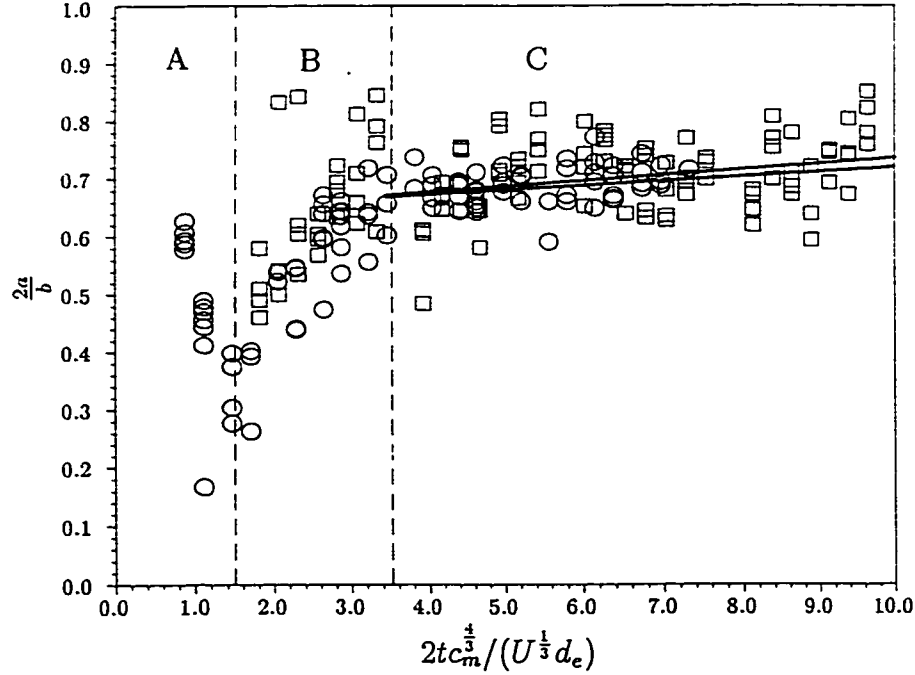
Figure 5.7: Ratio of the vortex ring's minor axis, a (defined in section 3), to one half the vortex rings major axis, b/2, vs nondimensionalized time (see caption to Fig. 5.4 for explanation of symbols).

are 370 and 320. These Re are within the known range for laminar vortex rings. While these are the Re after relaminarization, it is likely that the Re is significantly higher prior to transition when the vortex ring is travelling downward through the upward flow of the reversing impact crater. Therefore the velocities along the vortex ring's bounding stream-surface in a vortex ring-fixed frame of reference will have to be greater than that implied by the velocity of the vortex ring in a lab-fixed frame of reference.

The dimensionless velocity of the vortex ring was also plotted vs the scaled time in Fig. 5.8. The upper line is a best fit line for the data from Case 1, the lower line corresponds to Case 2. The scaling used was taken directly from the slope of the x_b vs. time graph. A general trend of slowly -
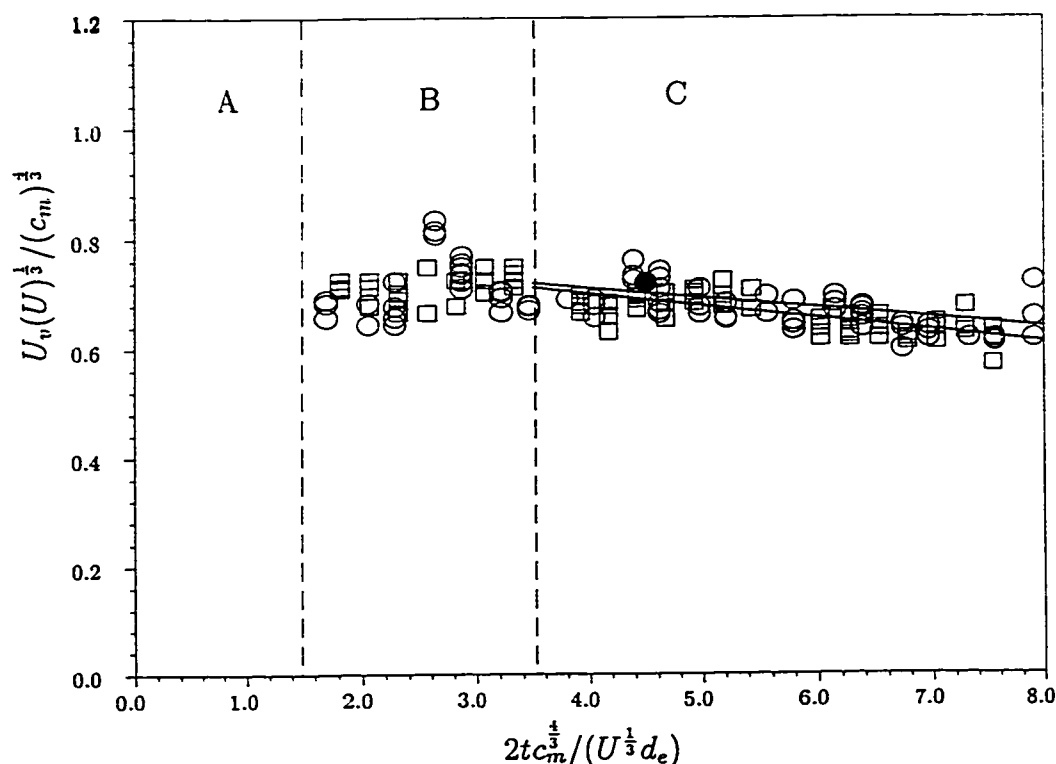
Figure 5.8: The nondimensional velocity of the vortex ring's major axis and a single data point given by RM for a vortex ring created by a 4.4 mm d_e drop impacting in the vertically prolate configuration (filled circle) vs. nondimensional time. The upper line is a best fit line for the data from Case 1, the lower line corresponds to Case 2 (see caption to Fig. 5.4 for explanation of symbols).

decreasing velocity is evident. In region C this is consistent with the motion of previously studied laminar vortex rings, (Maxworthy, 1972; Saffman, 1970). The offset between Case 1 and Case 2 that appeared in the location data now disappears and agreement is excellent, supporting the hypothesized scaling. The data point from the text of RM compares well with the present data.

A disconcerting prediction of this result is that the vortex ring velocity would scale to an inverse one third power of the drop velocity at impact. In other words, the velocity of the vortex ring will decrease as the drop height

is increased. In the present experiments the drops with the higher We and Fr impacted the pool at 80 cm/s creating a vortex ring with a velocity of 10.9 cm/s after relaminarization. The lower We and Fr drops impacted the pool at 68 cm/s and created vortex rings with a slightly higher velocity of 11.4 cm/s which is predicted from the scaling.

This discomfort is slightly alleviated by the following consideration. If it is assumed that the vortex ring velocity at early times will determine the total depth that the vortex ring will travel, then the penetration depth data collected by RM corroborates this scaling. The maximum depth of penetration (the depth at which the vortex ring ceases its downward motion) for a fully prolate drop at impact decreases with increasing fall height, with the exception of one anomalous result. Further agreement is found in Thomson and Newall (1885) where drops were used which were similar in size to those in the present experiments. Here the maximum depth of penetration was found to decrease with increasing drop height for five drop heights which produced greatest penetration. There is little quantitative data to test this result further.

5.5 Conclusions

The evolution of drop-produced vortex rings was measured and analyzed from drops released from two heights. In both cases the dyed drops had a $d_e = 2.6$mm but in Case 1 were almost spherical at impact while in Case 2 they were fully prolate. In the first case the drops impacted the pool with a $We = 23.2$, and $Fr = 25.2$. In the second case the drop had a $We = 16.6$ and $Fr = 18.0$. Measurements of vortex ring location versus time indicated a remarkably steady rate of progress, even in the early stages of vortex ring development. In these stages the upward motion of the free surface might be expected to have a retarding influence.

The drops with the higher We and Fr impacted the pool at 80 cm/s creating a vortex ring with a velocity of 10.9 cm/s after relaminarization. The lower We and Fr drops impacted the pool at 68.4 cm/s and created vortex rings with a slightly higher velocity of 11.4 cm/s at the same nondimensional time.

A proposed scaling uses d_e as a length-scale and the time to maximum impact crater depth as a time-scale. Values for this time predicted from theory compared well to measurements. The scaling gave excellent agreement when

used to compare the present results for vortex ring location and velocity with those previously published for significantly larger drops ($d_e = 4.4$mm) that had a similar We. The agreement occurred when the larger drops had struck the surface in a fully prolate configuration, but not when they were oblate. The validity of the scaling was also supported by direct qualitative comparison of the timing of the transition behaviour of the vortex ring. The scaling suggests the counter-intuitive result that the vortex ring velocity varies as $U^{-\frac{1}{3}}$. This is corroborated to some extent by previously published data.

Comparison between these data sets is encouraging but far from validates the scaling. More comparisons with different sized drops, other values of fall height, We and Fr are necessary for confirmation.

In the laminar ring region the ratio of the width of the vortex ring to the effective drop diameter was determined to be 1.25 to 1.4 compared to 1.3 for the larger drops. In this same region the ratio of the minor axis to one half the major axis was 0.7. This can be used as an indication of the shape of the ring. Self-similarity is implied by its constancy, although this was measured over a relatively short range of vortex ring propagation, approximately two drop diameters.

Bibliography

A. V. Anilkumar, C.P. Lee, and T.G. Wang. Surface-tension induced mixing following coalescence of initially stationary drops. *Phys. Fluids A*, 3(11): 2587–2591, November 1991.

D. S. Chapman and P.R. Critchlow. Formation of vortex rings from falling drops. *J. Fluid Mech.*, 29:177–185, 1967.

Ladan Esmailizadeh and Russel Mesler. Bubble entrainment with drops. *J. Colloid Interface Sci.*, 110(2):561–574, April 1986.

A. Glezer and D. Coles. An experimental study of a turbulent vortex ring. *J. Fluid Mech.*, 211:243–283, 1990.

William D. Harkins and F.E. Brown. The determination of surface tension (free-surface energy), and the weight of falling drops: the surface tension of water and benzene by the capillary height method. *J. Amer. Chem. Soc.*, 41:499–524, 1919.

Mingying Hsiao, Seth Lichter, and Luis G. Quintero. The critical Weber number for vortex and jet formation for drops impinging on a pool. *Phys. Fluids*, 31(12):3560 –3562, December 1988.

H. F. Keedy. *Vortex Rings Formed by Free-Surface Interaction*. PhD thesis, University of Michigan, Ann Arbor, Michigan, 1967.

T. Maxworthy. The structure and stability of vortex rings. *J. Fluid Mech.*, 51(part 1):15–32, 1972.

Hasan Oğuz and Andrea Prosperetti. Bubble entrainment by the impact of drops on liquid surfaces. *J. Fluid Mech.*, 219:143–179, 1990.

Bill Peck and Lorenz Sigurdson. The three-dimensional vortex structure of an impacting water drop. *Phys. Fluids*, 6(2):564–576, February 1994.

Bill Peck and Lorenz Sigurdson. The vortex ring velocity resulting from an impacting water drop. *Exp. in Fluids*, 18:351–357, 1995.

H Pruppacher and K. Beard. A wind tunnel investigation of the internal circulation and shape of water drops falling at terminal velocity in air. *Quart. J. R. Met. Soc.*, 96:247–256, 1987.

Francisco Rodriguez and Russel Mesler. The penetration of drop formed vortex rings into pools of liquid. *J. Colloid Interface Sci.*, 121(1):121–129, January 1988.

P. G. Saffman. The velocity of viscous vortex rings. *Stud. Appl. Math*, 49: 371–380, 1970.

G.I. Taylor. Formation of a vortex ring by giving an impulse to a circular disk and then dissolving it away. *J. Appl. Phys.*, 24(1):104, January 1953.

J. J. Thomson and H. F. Newall. On the formation of vortex rings by drops falling into liquids, and some allied phenomena. *Proc. Roy. Soc. London Ser. A*, 39:417–436, 1885.

M.C. Wilkinson. Extended use of, and comments on, the drop-weight (drop-volume) technique for the determination of surface tension and interfacial tension. *J. Colloid Interface Sci.*, 40(1):14–26, July 1972.

CHAPTER 6

AN APPARATUS TO STUDY DROP-FORMED VORTEX RINGS†

6.1 Introduction

The study of vortex rings is of fundamental interest in fluid mechanics. Saffman (1981) asserts that "one particular motion exemplifies the whole range of problems of vortex motion and is also a commonly known phenomenon, namely the vortex ring". The most popular method for producing vortex rings is to expel fluid through a sharp circular orifice. Although this experiment has been widely studied many questions about orifice-produced vortex rings and vortex rings in general remain unanswered (Auerbach, 1988; Shariff and Leonard, 1992). One difficulty encountered with orifice-created vortex rings is the effect of the solid boundaries on the vortex field's evolution when the vortex ring has just formed and is still very near the generator. Other methods of vortex ring production are known such as when a smoke filled air bubble on a free surface bursts (Rogers, 1858; Buchholz et al., 1995).

Another method to produce vortex rings without a solid boundary is to let liquid drops impact a pool of the same liquid. If the drops are released from not too great a height a vortex ring forms as the drop and pool coalesce (Rodriguez and Mesler, 1984; Hsiao et al., 1988). Although this experiment has been a subject of sporadic study for well over a century (Rogers, 1858; Thomson and Newall, 1885; Chapman and Critchlow, 1967; Rodriguez and Mesler, 1988) the phenomenon is still not completely understood.

The inspiration for this work is a photograph published by Okabe and

---

†A form of this chapter has appeared in the Journal of Measurement Science and Technology: Peck et al. (1995)

Inoue (1961) which appears in Batchelor (1967). We have recently undertaken our own experiments to elicit understanding of the vortex dynamics of drop-formed vortex rings from single and multi-exposure photographic data (Peck and Sigurdson, 1991, 1992, 1994a,b). Our intent was to reproduce and track the evolution of the structure seen in Okabe and Inoue's figure II,1 (Batchelor's figure 7.2.3). The difficulties in repeatably reproducing their result, which was necessary for a meaningful analysis from single exposure photography of separate events, soon became apparent. In Okabe and Inoue's experiments the drops were formed on the tip of a burette and allowed to fall into a pool. The large and irregular oscillations induced in the drop as it released from the tip of the burette were responsible for setting new initial conditions with each drop impact. This caused a large variation in the vortex structures observed with drops formed under the same conditions using the limit of control available with that apparatus. Constructing an apparatus to successfully reproduce this experiment was a challenging opportunity to utilize techniques from several areas of experimental science. We found this to be a difficult task with little assistance available in the literature.

The version of the apparatus which we will discuss is the latest of several iterations used in our laboratory. Through its evolution we have synthesized ideas from previous experiments and modified many areas which we believe precluded reproducibility and hence clear understanding of the phenomenon.

In this final form our apparatus provides another method to study the short and long term properties of vortex rings. By producing such small (3–6.7 mm diameter) low-Reynold's number vortex rings (Re less than 1500 where $Re = \frac{U_v D_v}{\nu}$ where U_v is the velocity of the vortex ring, D_v the vortex ring diameter and ν is the kinematic viscosity of the liquid) we have been able to observe the instability and transition to turbulence of a time-dependant three-dimensional vortex structure (Sigurdson and Peck, 1994). The long time evolution of the vortex ring can also be conveniently studied over its entire motion. This is not the case for vortex rings created by large orifice generators since they require very large and expensive reservoirs to conduct the experiment.

Although our primary interest is drop-formed vortex rings, this apparatus can also be used to study free-surface dynamics due to drop impact. For example, if drops impact the surface within a certain range of Froude and Weber numbers (Represented by Fr and We respectively where $Fr = \frac{U^2}{gD}$; $We = \frac{\rho U^2 D}{\gamma}$, ρ is the liquid's density, g is the acceleration due to gravity,γ is

the surface tension, U is the drop's velocity and D is the drop diameter) an air bubble is created by the impact crater. This phenomenon is significant to those studying underwater acoustics, boiling and cavitation. For a review of drop impact phenomena in general we refer the reader to Rein (1993) and Prosperetti and Oğuz (1993).

6.2   Apparatus

In constructing this apparatus our primary concern was to set reproducible initial conditions for each drop impact. Several parameters had to be considered for this to be so. The drop would have known fluid properties, impact velocity and oscillation phase. The pool onto which the drop fell would be clean with known fluid properties. Rogers (1858) also pointed out that "it is essential to a perfect experiment to have the liquid of the reservoir as motionless as possible, its mass should be large, and it should be allowed to come to rest after each drop before the next is allowed to impinge upon it" implying that the surface of the pool and the pool's bulk fluid should be motionless. To study the long term characteristics of vortex rings it is especially important to have the pool free of any currents which may have been created by the passage of vortex rings or temperature gradients in the pool. The atmosphere through which the drop fell should also be free of contaminants and currents. The following apparatus, shown in Fig. 6.1 and schematically in Fig. 6.2, was designed to meet these criteria.
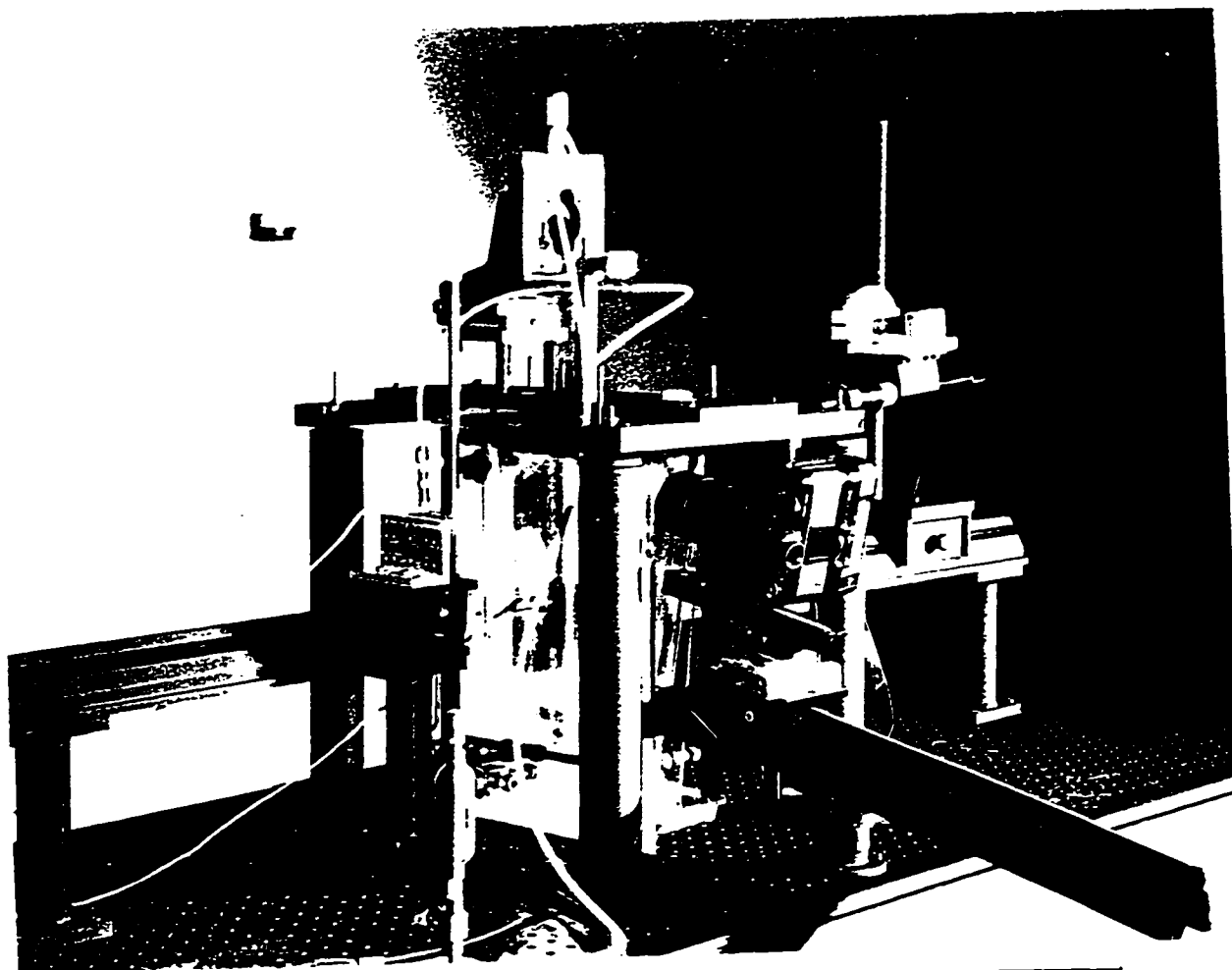
Figure 6.1: A photograph of the experimental apparatus. For clarity of presentation some of the support equipment is not shown.
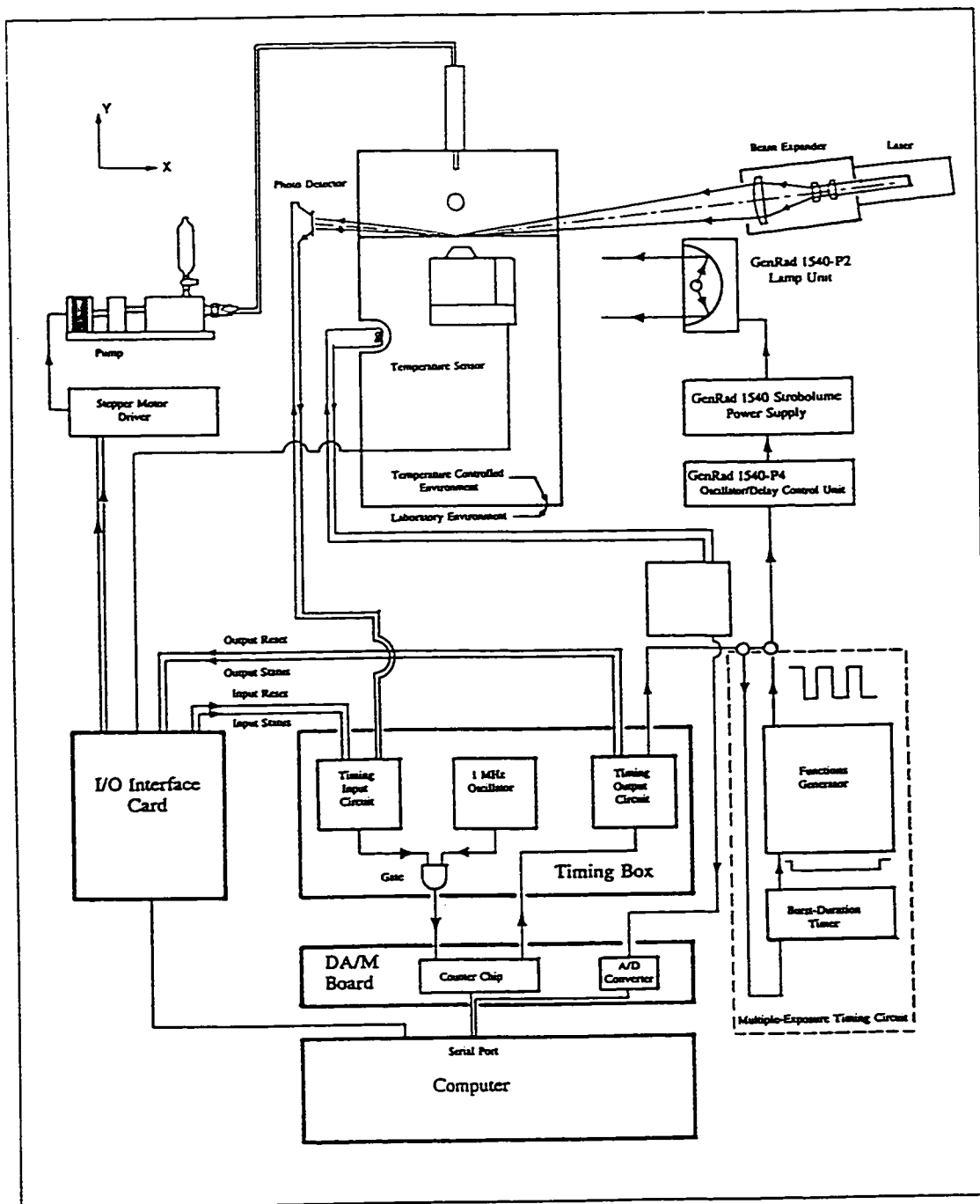
Figure 6.2: Schematic diagram of the experiment and electronics

6.2.1 The test cell

The liquid pool into which the drops fall is held within a sealed, prismoidal glass hexahedron made from 5 mm thick sheets of plane glass. The height
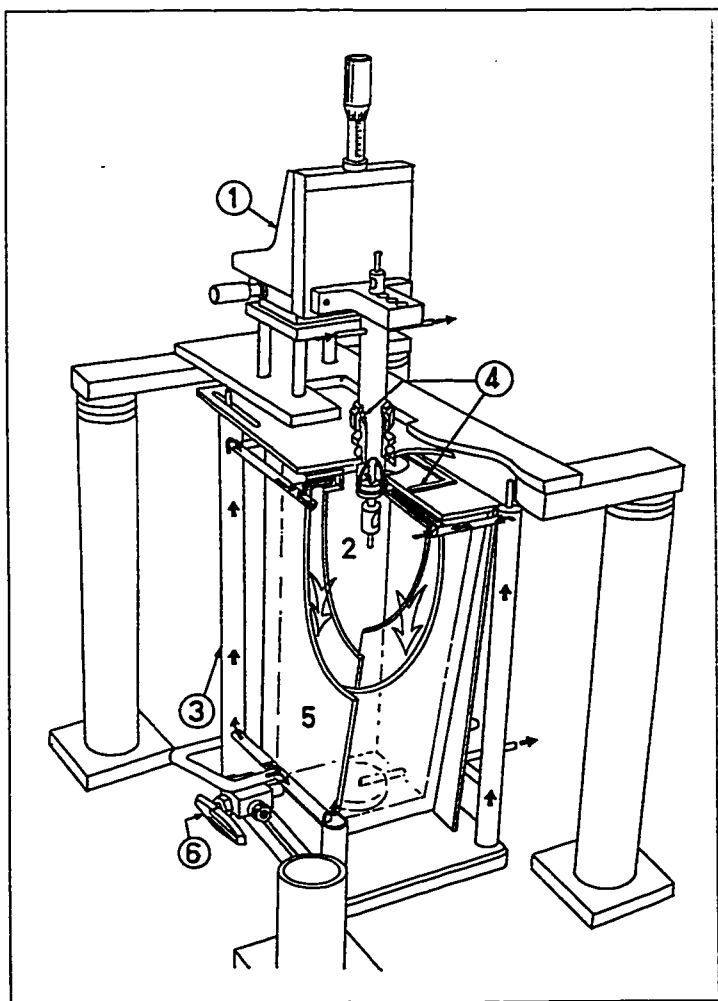
Figure 6.3: A cutaway perspective drawing of the temperature controlled pool reservoir. 1, three-axis traverse; 2, tip and tip holder assembly; 3, inlet manifold; 4, Teflon gaskets; 5, reservoir; 6, three-way inlet/outlet valve. The heavy dark arrows indicate the motion of heating/cooling fluid.

of the reservoir is 40 cm. At its base the reservoir is 10 cm×9 cm and at

the top 10 cm×13.5 cm. An 8 cm hole was drilled through the top of the reservoir to allow the entrance of the drop formation apparatus. The depth of the pool is sufficient to study of the most penetrating vortex rings based on previously published data (Rodriguez and Mesler, 1988).

The plane glass sheet provides transparency and optical flatness which are necessary to take clearly focused photographs. Having the film plane parallel to the walls of the test cell minimizes distortion of the image. With this in mind, one of the test cell's walls was tilted 5° outward from vertical enabling the camera to be positioned at a 5° angle below horizontal. This viewing location provides the clearest view of the drop impact and subsequent vortex-free-surface interaction. The plane walls will also allow the use of Laser Induced Fluorescence planned for future experiments. Laser Doppler Velocimetry and Particle Image Velocimetry have been considered but at present it is unclear how the requisite seeding particles would affect the sensitive interfacial properties.

Surface tension is very susceptible to outside contamination. To eliminate contamination from the apparatus it was important to design all the components of the apparatus that would come in contact with the pool or drop liquid to withstand vigorous cleaning procedures. With this in mind, the glass walls, top plate and bottom plate were ground together along their edges to obtain a water-sealed fit. The six pieces were then cemented together on the outside of the ground joint. This prevents the test fluid or volatile cleaning agents from coming in contact with and possibly dissolving surface active agents in the cement. It is also important to keep the interface free of contamination during the course of the experiment. To maintain the clean environment the pool was sealed from the lab environment using Teflon gaskets, Fig. 6.3.

A temperature sensor (Analog Devices 590J) is located on the wall of the reservoir to record the test-cell temperature. At the bottom of the reservoir an outlet pipe is attached to a Teflon-packed three-way valve for filling and draining the test fluid. A flange on the outlet pipe is ground into the glass to provide a clean, water tight seal.

6.2.2 Drop Formation

The pendant drops are formed on carefully prepared tips of various diameters to allow drops of the desired volume to be formed. The drops we have used ranged from 2.6 mm to 5.4 mm d_e where the effective diameter d_e is the

diameter of a sphere with the same volume. The smallest drops were formed on 27 gauge (.40 mm outside diameter) stainless steel hypodermic tubes and the largest on prepared Pyrex capillary tubing tips with diameters ranging from 2.594 to 5.560 mm.

The hypodermic tubes are prepared as follows. First the lateral surface of the tube is highly polished with successively smaller grits of diamond paste (1000-14000 mesh) while the tube is rotated in a precision collet mounted in a lathe. When a high polish is obtained the end of the tube is ground flat with a fine abrasive disc. This face is left unpolished to ensure the tip wets uniformly during the early formation stages of the pendant drop. This is similar to the method used by Wilkinson (1972) to prepare tips for measuring surface tension using the drop-volume method.

Pyrex tips are prepared using techniques similar to those given by Harkins and Brown (1919). This method is similar to that for the hypodermic tubing but requires the tubing to be ground circular before polishing. This is done by turning the capillary tubing rapidly in a lathe while simultaneously grinding the lateral surfaces with a diamond impregnated or silicon-carbide wheel mounted in a high speed tool. The surfaces are then polished as before. To finish its face the tip is mounted in a 10 cm diameter brass rod with a hole drilled slightly larger than the tip. The small cavity between the brass hole and the tip is filled with lapidary sealing wax before grinding the brass block and the tip with 600 grit carborundum paste. The wax prevents the edges from chipping while the face is being ground.

Burs or chips on the face of the tips inevitably cause pendant drops to creep up the sides of the tube. When the pendant drop released from the tip in this case the drops acquired a non-vertical trajectory. This was unacceptable to us for two reasons. First, it is important that the drop fall at a preset spot for timing accuracy, see Sec. 6.2.6. Also, with properly prepared tips forming drops of a known size, the surface tension may be measured using the drop-volume method.

After the tips are completed they are measured 16 times (in total) across four diameters using a tool-maker's microscope. This is necessary for an accurate knowledge of the diameter and to ensure they have not become oval during the polishing process. We summarize the characteristics of the tips in Table 6.1.

Appropriately sized, interchangeable Teflon collets hold the tips securely in a temperature controlled stainless steel mount, Fig. 6.3. This holder was mounted on a three-axis traverse which allows precise positioning of the tip

Tip	Mean Tip Diameter (mm)	Eccentricity
1	0.418 ± 0.003	1.001
2	2.594 ± 0.007	1.004
3	4.939 ± 0.001	1.005
4	5.560 ± 0.009	1.001

Table 6.1: A table of manufactured tips used and their sizes and eccentricities. The eccentricity listed is the largest ratio of the four mean diameters measured for each tip which are at right angles to each other.

in relation to the impact site

6.2.3 Temperature Control

A major concern in our experiments has been the control of the liquid's dynamic viscosity μ and the interface's surface tension γ. Both are functions of temperature. The rapid change with temperature in the dynamic viscosity of liquids is often overlooked in water drop experiments. The test cell and drop formation tip were temperature-controlled by a re-circulating bath of water. Fig. 6.3 shows the system's plumbing.

The water is fed into the chamber through a manifold with four inlets at the top of the tank, Fig. 6.3. A single outlet is positioned at the bottom. This was done to ensure a symmetric flow with uniform cooling. The tip holding device is also temperature controlled. An annulus was constructed around the feed pipe to the formation tips. Fluid is circulated through this annulus in parallel with the test cell chamber's plumbing.

By using an enclosed test environment and a circulating temperature control bath this apparatus eliminates any temperature gradients in the test fluids which may cause convection cells. Experiments to test for thermal gradients in the reservoir showed no measurable temperature gradients after 130 minutes (see Fig. 6.4). Each experiment was started in a worst case situation with the pool artificially far warmer or cooler than room temperature. The reservoir was then cooled/warmed until the temperature observed on three glass thermometers placed 1 cm from the bottom, the center and 1 cm from the top of the test cell did not change in a 10 minute interval. This systems temperature control also ensures that the temperature of the drop fluid will be the same of the pool fluid which has often been tacitly assumed in the
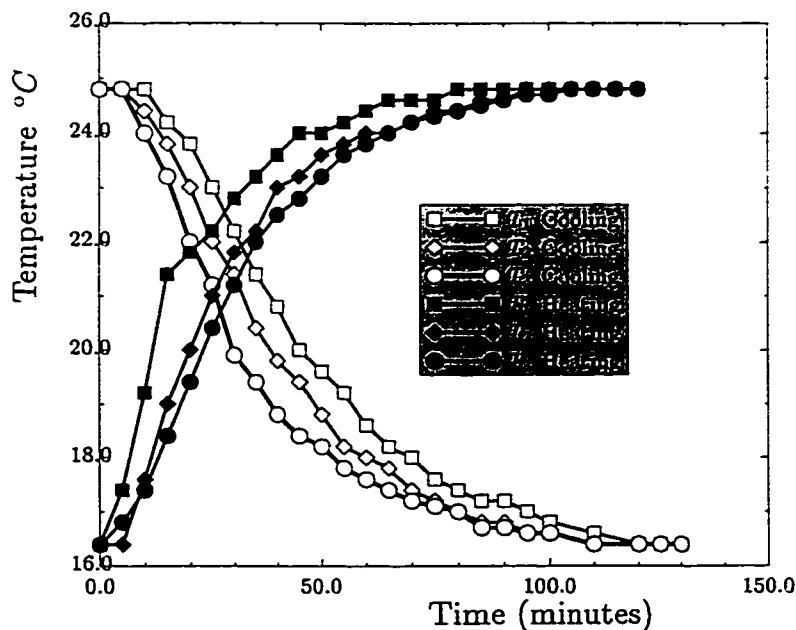
Figure 6.4: A plot of the test cell temperature vs. time for two cases. In the first case the temperature was recorded at three locations while the tank was cooled from 25° C. In the second, the tank was warmed from a cooled state.

past. This assumption is likely incorrect in most cases due to evaporative cooling of the drop in an open atmosphere. In this apparatus the atmosphere within the test cell is sealed and will reach a saturated state eliminating any evaporative cooling in the drop or the pool. These cells have been observed in other experiments (Keedy, 1967) and may have gone unnoticed in others. Early versions of the present apparatus such as that decribed in Chpt. 5 were very susceptible to these currents.

6.2.4   Pump

A small stepper-motor-actuated pump was constructed to deliver fluid to the drop-formation tips. The pump was a simple plunger riding in a cylinder. It is a rugged design which delivers accurate amounts of fluids. The materials

and methods of construction allowed the pump to be thoroughly cleaned. The pump body was machined from a solid block of stainless steel to eliminate the risk of contaminants being trapped in blind joints. The piston bore was honed to give a consistently sized 6.75 mm bore along the length of the cylinder. A small inlet hole enters the top of the cylinder through which the cylinder fluid is recharged. Teflon-packed ball valves are mounted on the pump inlet and outlet to direct the flow for drop production or cylinder recharging.

A stainless steel pushrod with a Teflon piston ring serves as the plunger. The plunger is translated along its axis by a live-nut mounted in precision bearings threaded onto a 40 tpi thread which was machined onto the rear 8 cm of the pushrod. The nut is turned while the plunger is not allowed to rotate. A gear reduced stepper motor was installed which drives the nut through a 45.71:1 gear reduction. The stepping motor allows computer automation of the process.

The pump, test cell, and drop formation tips form a system similar to an apparatus reported by Tornberg (1977) to measure surface tension by the drop-volume method. By knowing the volume displaced by the pump, V (determined from the stepper-motor input) to release a drop from a properly prepared tip of radius r it is possible to determine the surface tension from the relationship first developed by Harkins and Brown (1919),

$$\gamma = \frac{V \Delta \rho g}{2\pi r f(\frac{r}{V^{\frac{1}{3}}})}, \tag{6.1}$$

where $\Delta \rho$ is the density difference across the interface. The function $f(\frac{r}{V^{\frac{1}{3}}})$ is calculated from a fourth order polynomial fit to data collected by Wilkinson (1972). Thus, it is natural for us to use the data collected to keep track of the surface tension of our drops since there has been some question regarding the surfactant properties of the dyes used for flow visualization (Fluorescein). To obtain the most accurate measurements of surface tension with the drop-volume method the tip should be chosen such that $f(\frac{r}{V^{\frac{1}{3}}})$ is near 0.6 for a liquid/air interface. The largest tip we use is near this value and is the tip used for measuring reported values of surface tension (Peck and Sigurdson, 1994b). Data from the smaller tips are only used to monitor the surface tension as the experiment proceeds.

6.2.5 Photography and timing

A 35 mm format SLR camera (Nikon F-3) with motor drive (Nikon MD-4) is mounted on a bellows extension (Nikon PB-6). A 60 mm f/2.8 lens (Micro-Nikkor) is used in the standard or reversed configurations. The reversed configuration gives more object to lens distance under certain magnifications. We chose the Nikon F-3 camera for its ability to open and close the shutter manually while also using a motor drive. The optics are focused by replacing the drop formation tip with a stainless steel dowel. The dowel is lowered into the pool slightly and the lens is focused on it.

The photographs are taken in a darkened room with the camera shutter open. The strobolume lamp (Gen Rad 1540-P2 Lamp Unit) is discharged at a preset time after drop impact (see section 6.2.6). The strobolume control unit is set to the high intensity range giving a 15 μs peak light output. The length of the flash is sufficiently brief to freeze the phenomena we are observing. At this range of lamp intensity an f stop setting of 8 gives sufficient depth of field and brightness.

Multiple exposure photographs are used to measure velocities and check repeatability. In a previous paper representative results of this technique are used to consider a proposed scaling (Peck and Sigurdson, 1994b). The photographs used in these experiments were taken with the addition of the circuit shown in Fig. 6.2 and the strobolume lamp set to the medium intensity range. The frequency of the signal to the strobolume varies between 30 to 100 Hz which is too quick for the strobolume lamp to recharge while set at the highest intensity range.

The flow visualization photographs we obtain with 35 mm photographs are much clearer than those obtainable from high speed film (Hi-Cam) or video. Also, with our timing system, the timing resolution is generally far better than a Hi-Cam. Since a Hi-Cam must be started well in advance of the event the timing error will be the time between frames which is typically 1 ms. There is also a difficulty capturing the event at all due to the limited amount of filming time available (1-2 s). Experiments using high speed film must resort to artificially initiating the drop's fall in order to record its impact.

6.2.6 Timing

Discharging the strobolume lamp at a predetermined and reproducible time after impact was necessary to construct an accurate record of the vortex

ring's evolution. In a previous paper Peck and Sigurdson (1994a) we observed dramatic restructuring of the vortex topology in less than 5 *ms*. Our system was able to time the lamp's discharge with a typical error of less than 100 μs.

The triggering system was set up as follows. A 0.5 mW He-Ne laser (Melles Griot model 05 LLR 811) was declined 5 degrees from horizontal and focused on the centre of the impact site using an 8 × beam expander (Melles Griot model 09 LBC 003). The timing circuit was triggered by an interruption in the laser beam that had been reflected off of the air water interface into a photo detector positioned on the opposite side of the pool. We chose this geometry so that the drop would pass through the beam close to the interface. This reduces the amount of timing lead that would otherwise have to be determined and adjusted out if the drop were to break the beam at some point further above the interface. While the best position for the beam would have been parallel to the plane of the interface it was necessary to use our present geometry to avoid interference from the meniscus on the sides of the tank.

The geometry of the laser trigger introduces a lead time due to the beam touching the falling drop's surface at latitudes removed from the lower pole, point P in Fig. 6.5. The lead time is increased if the central axis of the drop does not pass through the point of symmetry, O and the drop first touches the laser beam at point Q. There is also an error due to the uncertainty of when the beam is sufficiently attenuated by the passing drop to begin the timing circuit.

An analysis of the maximum lead time for a spherical drop yields

$$\delta_t \approx \frac{1}{\sqrt{2gh}} \left[R(\sec\alpha - 1) + \epsilon_x \tan(\alpha) + \frac{\lambda f \sec\alpha}{6\pi w} \right] \qquad (6.2)$$

where δ_t is the lead time. This is the time it takes for the drop's bottom pole to traverse the distance to the pool surface from its point in space when first contact is made between the drop and the laser. From left to right, the first term within the braces represents the error due to the first contact of the drop with the laser at latitudes removed from the bottom pole, Fig. 6.5. The second term arises due to uncertainty in the lateral positioning of drop, ϵ_x. The last term is the laser beam width, where λ is the wavelength of the laser (629 nm), f the focal length of the beam expander (60 cm) and w is the laser beam width before entering the beam expander. The distance was then divided by the calculated velocity for a body falling in a vacuum $u = \sqrt{2gh}$,
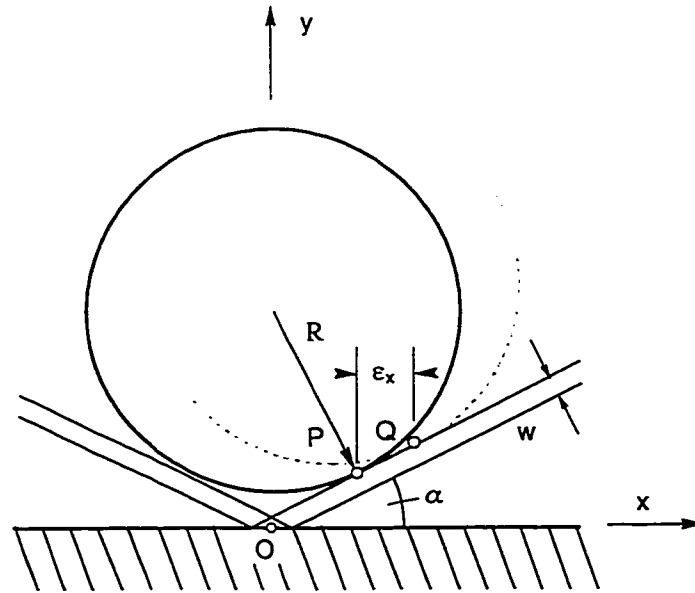
Figure 6.5: The geometry of the laser timing circuit. Here R is the spherical drop radius, w is the laser beam width, α is the laser beam's declination. The dashed circle represents a drop which has fallen away from the point of symmetry O by an amount ϵ_x.

where h is the distance the drop centroid has fallen from release. In the analysis we have assumed that the drop's acceleration is negligible over the small time interval considered and that the beam does not diverge.

The results are displayed graphically in Fig. 6.6 and Fig. 6.7 for an ϵ_x of 1 mm. Fig. 6.6 shows the timing to be more sensitive to declination angle than drop radius. The second figure illustrates the individual contributions to the lead time from the three terms. The greatest contribution to the lead time is due to the lateral positioning of the drop. For the range of experiments we wish to study the lead time will fall below 0.5 ms.

6.2.7 Vibration control

This experiment is very succeptible to vibration. It was necessary to mount the reservoir, drop formation apparatus, laser timing equipment and photographic equipment on a 75 × 181 cm optical table supported by four air-
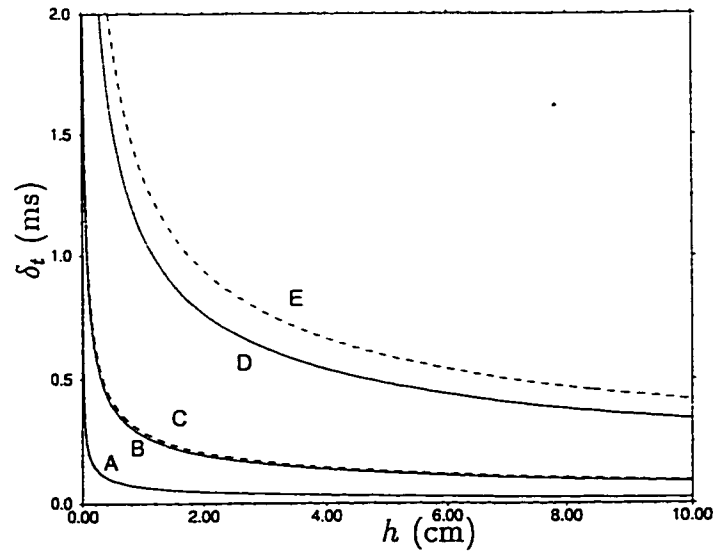
Figure 6.6: The combined lead time and timing error versus fall height. Curves A B and D represent a 2.6 mm d_e drop with declination angles α of 0, 5 and 20 degrees respectively. Curves A, C and E represent a 6 mm d_e drop with the same respective values of α (The curves for $\alpha = 0°$ are coincident for both d_e)

charged vibration isolation dampers. The centre of the stand-offs and the optical benches used to support the laser equipment were filled with lead shot suspended in an elastomer (Flex-ane 80) for damping.

6.3   Automation

6.3.1   Electronics

The experiment was automated by a small computer (Hewlett Packard Vectra 286) to eliminate any uncertainty or irregularities due to human control. With reference to Fig. 6.2, the pump's stepper motor, 35 mm camera, and timing circuits are controlled through a I/O interface card (Metrabyte PIO-96). A separate board (DA/M-100-3) with an on-board counting IC chip is used to count the gated output from a 1 MHz oscillator. The gate is opened by an interruption in the signal from the photo detector (Motorola
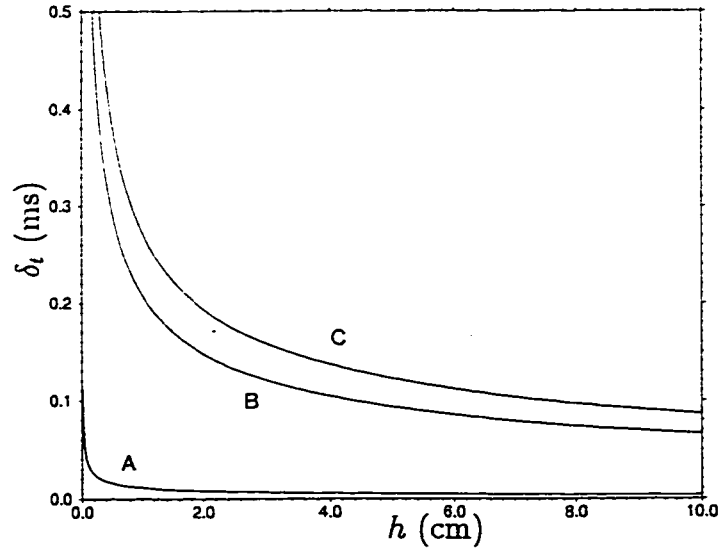
Figure 6.7: Components of the lead time versus fall height for a 2.6 mm d_e drop with fixed $\alpha = 5°$. Curve A is the lead time due to the laser beam striking the drop at latitudes removed from the lower pole. The distance between curves B and A is the lead time due to the passage of the drop through the beam. The distance between curves C and B is the increased lead time due to misalignment of the drop's vertical axis with the point of symmetry

MRD 300). Flip-flops in the timing input circuit ensure only one signal passes on to the gate for each impact. This is necessary to eliminate multiple inputs to the gate because of impact-created surface waves reflecting the laser beam over the photo detector several times. A signal to the strobolume control unit (GenRad 1540-P4) is sent after the counting chip counts down to its pre-loaded number of cycles input to it from the computer program for each exposure. The strobolume control unit was modified to eliminate an inherent 300 μs delay. An optional multiple-exposure timing circuit is shown in Fig. 6.2. A gated function generator (Dynascan 3030) is put in line with a duration timing circuit. Thus we are able to determine the period between and number of bursts.

6.3.2 Computer Control

Computer software used to run the experiment was written in the QuickBA-SIC language. The program is fully automatic and needs no input from an operator once the experimental run is begun. The number of experiments in each run is only limited by the number of exposures on the camera's film, which is usually 24 or 36. The program uses flash delay times as well as drop formation rates input before the start of an experiment. The formation rates determine how fast the pendant drop will be formed. This is done in two stages; in the first stage the pendant drop is rapidly filled to approximately 90 percent of its final volume in approximately 60 s. Then the drop is slowly filled until it falls away which may take from 60 to 120 s. The time for the experiment to lay dormant between exposures is set at 2 minutes which allows any disturbances from previous drops to dissipate.

6.4 Conclusions

An apparatus which can reproducibly study the vortex ring produced by the impact of a liquid drop on a liquid pool has been discussed. The experiments are conducted in a sealed, temperature-controlled glass walled reservoir. To eliminate inconsistencies from human control the apparatus was fully automated allowing runs of 24 to 36 separate impacts. Single exposure photographs are taken by discharging a strobe lamp at a precisely controlled time after impact. The combined error and lead in timing the strobe discharge varies with the impact velocities and is $O(.1ms)$. Multiple-exposure photographs are used to measure vortex velocities from flow visualization photographs. By drawing on techniques used to measure surface tension, the surface tension of the drops used to form the vortex rings can be measured and monitored.

Bibliography

D. Auerbach. Some open questions on the flow of circular vortex rings. *Fluid Dyn. Res.*, 3:209–213, 1988.

G. K. Batchelor. *An Introduction to Fluid Dynamics*. Cambridge University, New York, 1967.

James Buchholz, Lorenz Sigurdson, and Bill Peck. Bursting soap bubble. *Phys. Fluids*, 7(9):s3, September 1995.

D. S. Chapman and P.R. Critchlow. Formation of vortex rings from falling drops. *J. Fluid Mech.*, 29:177–185, 1967.

William D. Harkins and F.E. Brown. The determination of surface tension (free-surface energy), and the weight of falling drops: the surface tension of water and benzene by the capillary height method. *J. Amer. Chem. Soc.*, 41:499–524, 1919.

Mingying Hsiao, Seth Lichter, and Luis G. Quintero. The critical Weber number for vortex and jet formation for drops impinging on a pool. *Phys. Fluids*, 31(12):3560 –3562, December 1988.

H. F. Keedy. *Vortex Rings Formed by Free-Surface Interaction*. PhD thesis, University of Michigan, Ann Arbor, Michigan, 1967.

J. Okabe and S. Inoue. The generation of vortex rings, II. *Rept. Res. Inst. Appl. Mech.*, 9(36):147–161, 1961.

Bill Peck and Lorenz Sigurdson. Impacting water drop. *Phys. Fluids A*, 3 (9):2032, September 1991.

Bill Peck and Lorenz Sigurdson. Impacting water drops. *Phys. Fluids A*, 4 (9):1872, September 1992.

Bill Peck and Lorenz Sigurdson. The three-dimensional vortex structure of an impacting water drop. *Phys. Fluids*, 6(2):564–576, February 1994a.

Bill Peck and Lorenz Sigurdson. The vortex dynamics of impacting water drops. In *Eleventh Canadian Symposium on Fluid Mechanics.*, page 125, 1994b.

Bill Peck, Lorenz Sigurdson, Bernard Faulkner, and Ian Buttar. An apparatus to study drop-formed vortex rings. *Measurement Science and Technology*, 6:1538–1545, 1995.

Andrea Prosperetti and Hasan Oğuz. The impact of drops and the underwater noise of rain. *Annu. Rev. Fluid Mech.*, 25:557–602, 1993.

Martin Rein. Phenomena of liquid drop impact on solid and liquid surfaces. *Fluid Dyn. Res.*, 12:61–93, 1993.

Francisco Rodriguez and Russel Mesler. Some drops dont splash. *J. Colloid Interface Sci.*, 106(2):347–352, February 1984.

Francisco Rodriguez and Russel Mesler. The penetration of drop formed vortex rings into pools of liquid. *J. Colloid Interface Sci.*, 121(1):121–129, January 1988.

W.B. Rogers. On the formation of rotating rings by air and liquids under certain conditions of discharge. *Am. J. Sci. Arts. Sec. Ser.* , 26:246–258, 1858.

P.G. Saffman. Dynamics of vorticity. *J. Fluid Mech.*, 106:49–58, 1981.

Karim Shariff and Anthony Leonard. Vortex rings. *Annu. Rev. Fluid Mech.*, 24:235–279, 1992.

Lorenz Sigurdson and Bill Peck. Three-dimensional transition of the vorticity created by an impacting warter drop. In V. R. Benzied, editor, *Advances in Turbulence*, pages 470–475. EuroMECH, Kluwer Academic, 1994.

J. J. Thomson and H. F. Newall. On the formation of vortex rings by drops falling into liquids, and some allied phenomena. *Proc. Roy. Soc. London Ser. A*, 39:417–436, 1885.

Eva Tornberg. A surface tension apparatus according to the drop volume principle. *J. Colloid Interface Sci.*, 60(1):50–53, June 1977.

M.C. Wilkinson. Extended use of, and comments on, the drop-weight (drop-volume) technique for the determination of surface tension and interfacial tension. *J. Colloid Interface Sci.*, 40(1):14–26, July 1972.

CHAPTER 7

DROP-FORMED VORTEX RINGS

7.1 Introduction

This chapter presents results from experiments using impacting water drops
to produce vortex rings. This interest results from Sigurdson's observation
of the similarity between the vortex structure created by a water drop im-
pacting a pool of water and structure visible in an atomic blast (Sigurdson,
1991; Sigurdson and Peck, 1992a,b). The goal is to understand the process
that creates vorticity from this assumed initially irrotational flow and to
understand how vortex rings form (Peck, 1993; Peck and Sigurdson, 1994;
Sigurdson and Peck, 1994). We also discuss possible explanations of how an
instability forms on the vortex ring at early times.

Our previous work in this area addressed vortex structures formed by
2.6 mm diameter impacting drops and subsequent motion of the vortex rings
at early times after impact. There are still outstanding questions however:
the means by which vorticity is created by the drop impact is addressed as is
the process of vortex ring formation from this vorticity. Also the mechanism
which leads to instability on the vortex ring at early times and the final
stages of motion when the vortex ring stops are discussed.

Experimental data reported in this chapter have been acquired using high-
speed photography. Recently several authors have called for more sophisti-
cated techniques to be employed for studying this phenomenon, for example
PIV or LIV (Durst, 1996; Dooley et al., 1997). There is no doubt that our
understanding of this experiment would benefit from such analysis. However,
before these expensive experiments could be considered we chose to address

---

†A version of this chapter will be submitted to the Journal of Fluid Mechanics

the quality of the experiment itself rather than the measurement technique's sophistication. As we showed in Chpt. 6, several parts of this experiment have gone overlooked even though they could have significant effects on the experiment. Addressing these concerns allowed us to carefully study effects of droplet oscillation phase on vortex ring formation. Precise timing allowed us to study the effect of drop height on vortex ring formation. Temperature control of the reservoir was also important to ensure a repeatable oscillation phase at impact. Temperature control also ensured any thermal gradients in the reservoir were small enough to allow the final stages of vortex ring decay to be studied.

A significant contribution from this chapter is the description of the vorticity creation process in this experiment. Thomson and Newall (1885) explained the creation of vorticity by comparing the impacting drop to a solid sphere impinging on a free surface. They believed the the drop surface could act as a rigid surface from which vorticity would diffuse in a similar way as from a solid boundary. Chapman and Critchlow (1967) attempted to explain vorticity creation in terms of circulation present after impact; no explanation of actual vorticity creation was given though. More recently, Sigurdson and Peck (1989) suggested a vorticity creation process dependent on baroclinic torques. Later, we discussed the level of vorticity which must be present at a free surface to satisfy the vanishing tangential stress condition(Peck and Sigurdson, 1994). This discussion was quite elementary since we were basing this on results for a steady surface (Batchelor, 1967). A recent paper by Creswell and Morton (1995) has extended this idea to the surface of a coalescing drop using a fixed toroidal coordinate system which limited their analysis. Rein (1996) recently published work on coalescing and splashing drops where he cites the work of Creswell and Morton (1995) to account for vorticity generation. In this chapter we further refine these ideas with the results derived in Chpt. 2 and explain the application of torques at the interface using results from Chpt. 4.

Two recent papers have investigated the case of pendant drops just coming in contact with a pool (Shankar and Kumar, 1995; Dooley et al., 1997). In these experiments drops are formed slowly on a tip until they come in contact with the receiving pool. The primary interest here is scaling formation parameters to the penetration depth. Only Dooley et al. (1997) address the vorticity creation process directly. Here they explain vorticity creation in terms of vorticity flux Φ. Shankar and Kumar (1995) discuss the creation of vorticity but in the context of a "slug". The slug is defined as the drop

fluid just after making contact with the pool. They believe this slug to be rotational but do not discuss how rotational motion is generated. Their remaining discussion describes boundary layer separation from the free surface.

Details of boundary layer separation from the free surface and its subsequent roll-up into a vortex ring has received little attention. Creswell and Morton (1995) give the only detailed description of this process. We extend these ideas using new photographic data and the analysis from previous chapters. These new data show how vortex rings are formed from the separated boundary layer. We also show that vorticity is created by high We drops and explain how vortex ring formation is inhibited by the impact craters subsequent pinch-off into a submerged bubble.

Observations of an instability forming on the vortex ring at early times extends the discussion begun in Peck and Sigurdson (1994) and Sigurdson and Peck (1994). New photographic data of the instability is presented.

This chapter is organized as follow. In Sec. 7.2 we briefly review the apparatus. The apparatus used in these experiments allowed us to examine the behaviour of vortex rings at very low Re. Sec. 7.3 presents results from careful experiments to understand the motion of drops as they were released from the formation tip. These results let us investigate the relationship between drop fall height and penetration depth of vortex rings in Sec. 7.4. Here we also discuss what is meant by a penetration depth in this context. From this we were able to choose appropriate drop heights to examine the vorticity creation and subsequent instability of the vortex rings. Sec. 7.5 presents results from detailed photography of the vortex ring formation and discusses the vorticity creation mechanism. Also, we discuss possible mechanisms which explain the appearance of the high-wavenumber instability at early times. We summarize our findings in Sec. 7.8.

7.2 Apparatus

Experiments discussed in this chapter used the apparatus described in Chpt. 6. A single drop size was used for all the experiments presented in this chapter. The drops were formed from the number 3 tip in Table 6.1. The drop's size was calculated from the volume displaced to produce each drop by the precision pump described in Sec. 6.2.4. The average effective diameter d_e was calculated to be 5.18 mm ± 0.01 mm from a data set with $n = 208$. A histogram of these data is shown in Fig. 7.1. Surface tension was tracked during
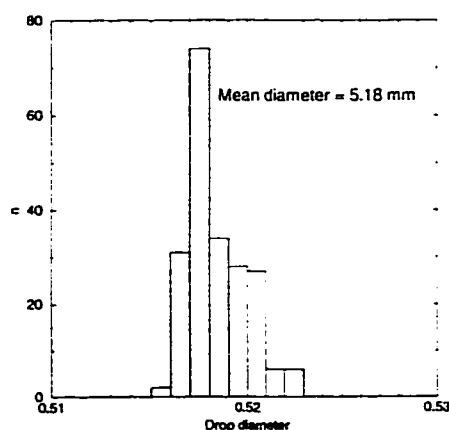
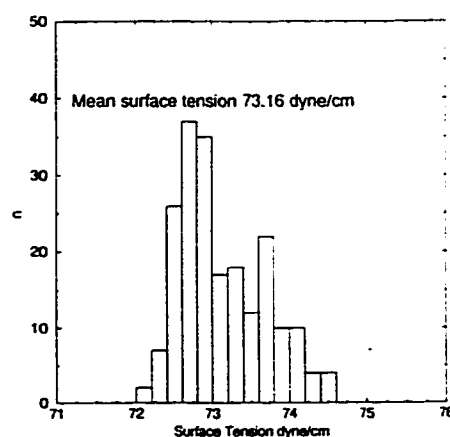Figure 7.1: Histogram of drop diameter calculated from drop volume

Figure 7.2: Histogram of γ calculated from drop volume

the experiments using the drop-volume technique discussed in Sec. 6.2.4. The mean γ was 73.16 $dynes/cm$ with a standard deviation of 0.601 $dynes/cm$. A histogram of γ using data from these experiments is shown in Fig. 7.2.

This apparatus has significant advantages over that used for the experiments described in Chpt. 5. This apparatus allowed us to reproduce experimental conditions with sufficient accuracy. Temperature control and the enclosed environment ensured consistent fluid properties in each experiment. The cooling system was set at 15.0 $^{\circ}C$ which produced a uniform 15.4 $^{\circ}C$ throughout the test cell. The maximum temperature variation over the experiments was $0.1C^{\circ}$. This eliminated currents visible in pools open to the atmosphere which are presumedly caused by evaporative cooling at the surface. The quiescent state of the test cell allowed very accurate observations of the vortex ring behaviour at long times after impact where the vortex ring expands very quickly.

7.3 The falling drop

A large drop diameter was chosen so that the range of experiments performed would span the known range where vortex rings are known to form. This range extends to $We = 64$ (Hsiao et al., 1988). With the present apparatus

and drop size we were able to study drops with $We = 76$. Also, drop oscilla-
tions are known to affect the quality of the vortex ring formed. The larger
oscillation amplitude of these drops would amplify this effect.

To this end, we began by gathering a detailed record of the drop's ge-
ometry during free-fall. This was necessary to determine the effects of the
drop's phase on vorticity creation and vortex ring formation process.

Previous publications have given little attention to this part of the ex-
periment (Keedy, 1967; Chapman and Critchlow, 1967; Hallet and Chris-
tensen, 1984; Rodriguez and Mesler, 1988). Keedy (1967) includes several
photographs of the drop in free-fall but only studied smaller diameter drops
(0.26 cm). Chapman and Critchlow (1967) discussed the geometry of larger
drops in free-fall but no photographs are included with their paper. They
do provide a plot of eccentricity vs fall height taken from unpublished pho-
tographic data. Eccentricity was defined as the vertical height of the drop
divided by its width. From these data they deduced the effect of oscillation
phase on vortex ring penetration depth. Hallet and Christensen (1984) and
later Rodriguez and Mesler (1988) only published photographs of drops at
times within a few milliseconds of the moment of impact.

A series of sixty-seven precisely timed photographs taken of the falling
drop give a detailed record of its behavior during free-fall. The photographs
are in groups of two to five of the same drop at 15 ms intervals. Twenty
drops were photographed this way, each subsequent drop having the initial
delay incremented 1 ms which filled in the information over 15 ms intervals.

The photographs were scanned into electronic format and data collected
from these electronic images. Electronic images were enhanced using Adobe
Photoshop© software. Photoshop was then used to trace outlines of the drops
in free-fall to be imported by Adobe Illustrator© where bitmaps of the profile
were made. An example of a scanned photograph and the corresponding
bitmap is shown in Fig. 7.3. This step was necessary since the images were
not clear enough for the edge finding filters in Photoshop to give a reliable
edge. The filled bitmaps were analyzed using Matrox Inspector© software.
These images gave the drop centroid and position relative to the tip.

7.3.1 Drop separation

Detailed behavior of the drop as it separates from the tip is available from the
photographic data. Using the method described in Chpt. 6 a pendant drop
was quickly filled to 90% of its predicted final volume on the formation tip and
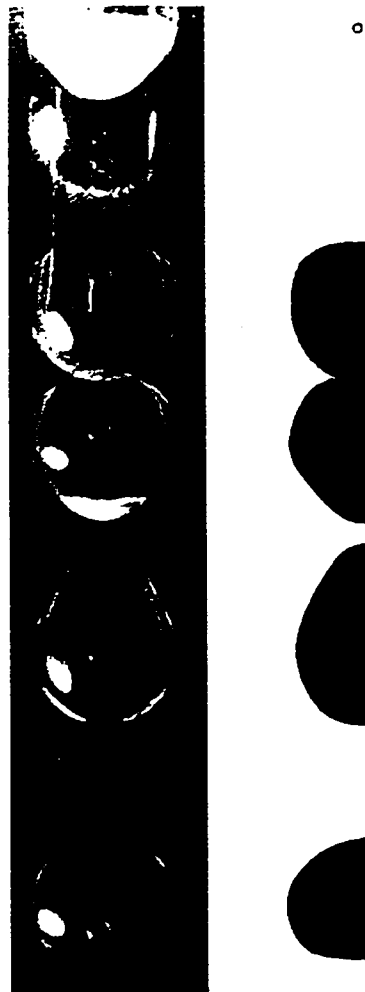
Figure 7.3: A scanned image and the corresponding filled bitmap. The tip diameter visible at the top of the photograph is 4.939 mm. A smaller 1.1 mm diameter drop formed during drop separation is visible. The multi-exposure photography timing causes this smaller drop to be superimposed on the previous exposures main drop

then slowly filled until it fell away. An estimated outline of the pendant drop is shown by the light line in Fig. 7.4. Previous experiments have assumed the centroid of the drop was one drop radius below the formation tip Chapman

and Critchlow (1967); Rodriguez and Mesler (1988). The fall height was then determined to be the distance from one drop radius below the tip to one drop radius above the surface. Analysis of our photographs show this assumption to be flawed. As the drop begins to move away from the tip, the radius of
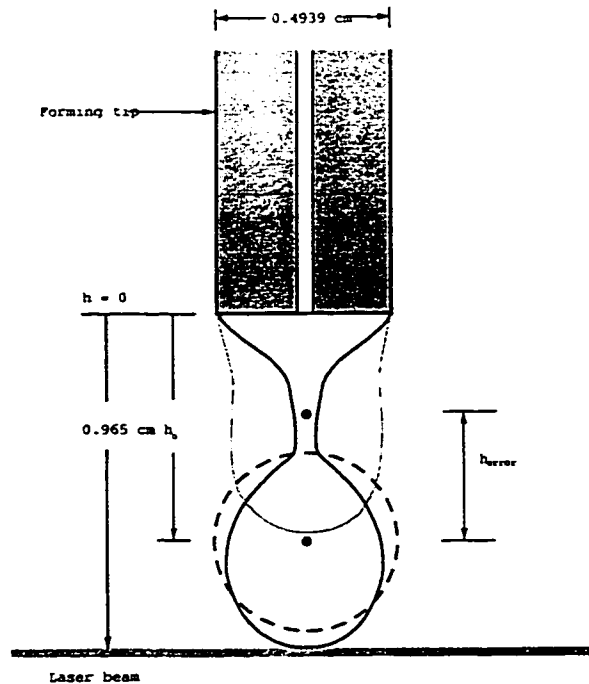
Figure 7.4: A scale drawing showing a pendant drop on the formation tip. The distance h_o is the distance from the base of the tip to the virtual origin determined from Fig. 7.6. The dashed line represents the profile of a spherical drop centred on the virtual origin represented by the small circle filled with a cross. A similar circle above h_o represents one drop radius from the base of the tip. h_{error} is the distance between these two points. The drop profile outlined with a solid dark line extending to the laser beam is the actual profile of the pendant drop 15 ms after it breaks the laser beam. The light gray line represents an approximate outline of a pendant drop before it begins to separate from the tip.

the pendant drop begins to decrease about one drop radius below the tip. This forms a neck shown by the darkly outlined profile in Fig. 7.4. The first

image in Fig. 7.5 shows the drop profile 1 ms later, very near the instant when the drop disconnects from the tip. Surface tension retards the motion of the fluid which will form the drop until the neck breaks. After the drop is disconnected from the neck, the drop centroid will be in free-fall. Profiles of the drop in free-fall are shown in Fig. 7.5. Positions of the drop centroid were found from computer analyses of the filled bitmaps. These are plotted vs time in Fig. 7.6. A best fit line of this plot gives:

$$h(t) = 0.682 \ cm + 6.24t \ \frac{cm}{s} + \frac{1}{2}932 \ t^2 \ \frac{cm}{s^2}. \tag{7.1}$$

This fit under predicts the value of $g = 9.81 \, m/s^2$ by 5%.

Setting the first time derivative of Eq. (7.1) to zero gives the time when the freely falling drop would have been stationary. The drop's virtual origin is the corresponding point in space h_o. In time, the calculation gives -6.7 ms or 21.7 ms before the outlined image in Fig. 7.4. In space, this corresponds to 0.64 cm below the forming tip's base. Thus, the starting point of the drop's centroid is over one drop diameter from the forming tip's base. In contrast, previous papers have used one drop radius to estimate the virtual origin. This would be less than half the correct height in the present case.

These data are specific to the drop size considered. For much smaller drops (2.6 mm diameter) the drops are nearly spherical when released from the tip. This would move the virtual origin closer to one drop radius below the tip.

The drops used in the experiments of Rodriguez and Mesler (1988) and Chapman and Critchlow (1967) are closer to the size studied here. Thus, their estimate of the virtual origin is likely incorrect. This explains the error correlating penetration depth with oscillation phase reported by Rodriguez and Mesler (1988). Using the incorrect higher virtual origin increases the calculated drop velocity over the true drop velocity. Hence, the time between oscillations they calculated from their assumed drop height is likely incorrect.

7.3.2 Drop oscillation

The freely falling drop's oscillation period was measured from plots of data taken from the filled bitmaps. The oscillation amplitude Φ_d plotted against time is shown in Fig. 7.7. The amplitude was calculated by measuring the vertical height of the drop and subtracting the effective diameter. $\Phi_d = (h_{max} - h_{min}) - d_e$. Measuring peak to peak gives a 34.0 ms period. This
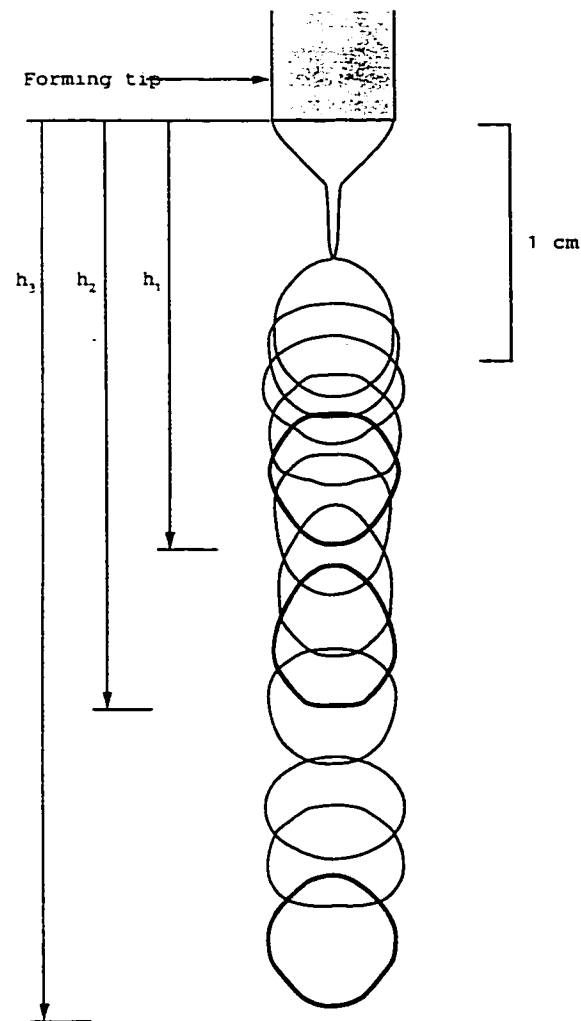
Figure 7.5: The drop centroid position relative to the base of the formation tip vs. time. Zero time is the moment the drop passed through the laser set at a height determined by trial and error

compares well with the predicted period of 34.2 ms calculated using Kelvin's
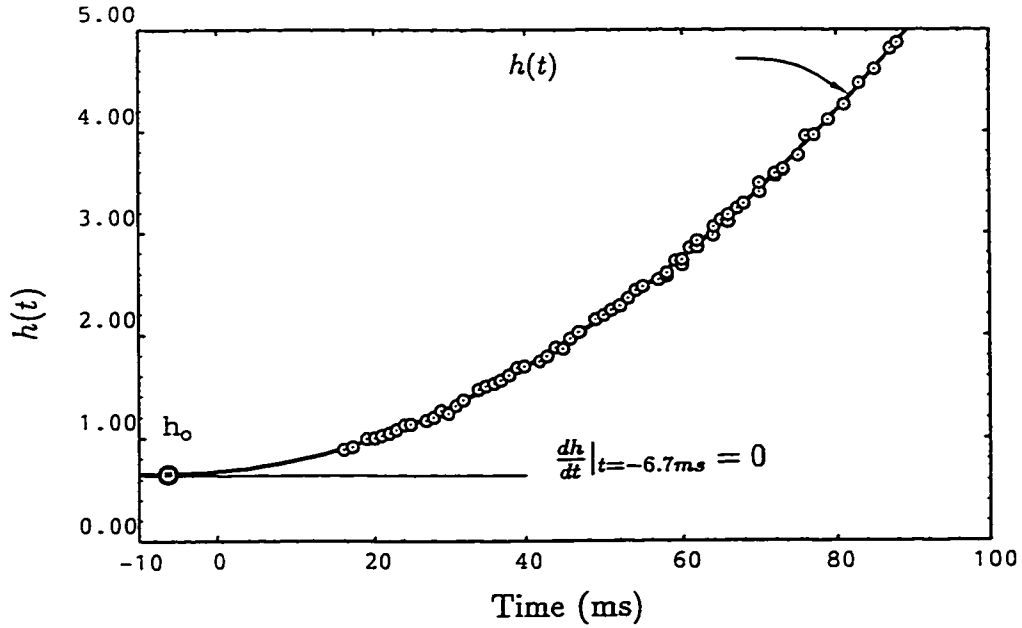
Figure 7.6: Plot of the position of the drop centroid $h(t)$ relative to the base of the formation tip vs. time. The virtual origin, the point in space where the velocity is zero, is represented by h_0. The flash delay was set at 15 ms after the drop broke the laser beam. This time was found by trail and error. Here, $h(t) = 0.682\ cm + 6.24\ \frac{cm}{s}\ t + \frac{1}{2}932\ \frac{cm}{s^2}\ t^2$.

result (Lamb, 1932; Chapman and Critchlow, 1967):

$$\tau_d = \frac{\pi}{4}\sqrt{\frac{\rho d_e^3}{\gamma}}.$$

(7.2)

We used values previously given in this text for this calculation: $\gamma = 73.16\ dynes/cm$; $\rho = 0.999\ gm/cm^3$; $d_e = 0.518\ cm$.

Figure 7.7: Plot of the amplitude of oscillation vs time. The values of $\Phi_d > 0$ correspond to a vertically prolate drop; $\Phi_d < 0$ correspond to a vertically oblate phase. Oscillation period τ_d measured peak to peak is 34 ms.

7.3.3 Drop volume

The drop's volume was easily calculated using the area and centroid calculated from the filled bitmap using Matrox Inspec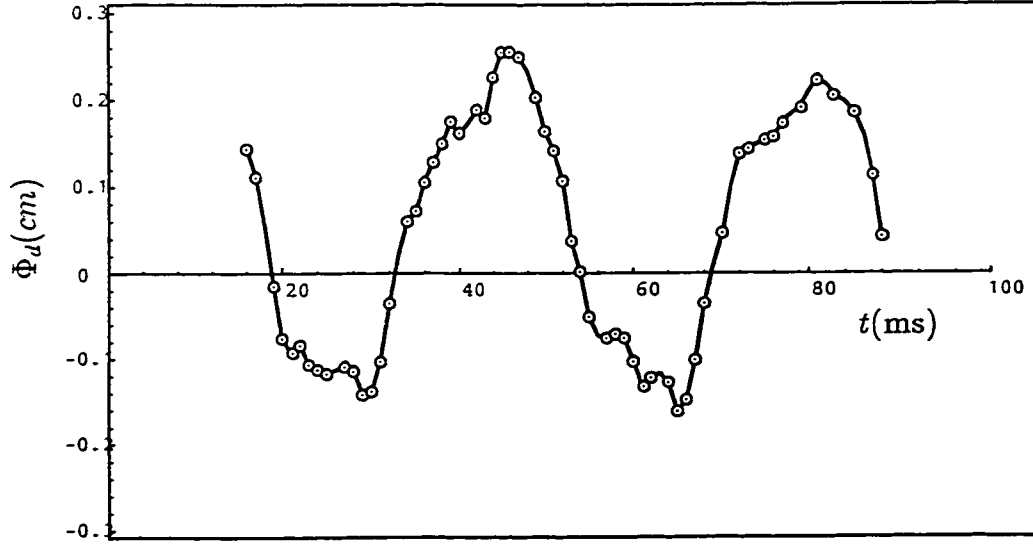tor © software (see Fig. 7.3). The filled bitmaps are half of the drop profile. The volume of the drop was calculated from the position of the centroid from the vertical axis $\bar{x}$ and the bitmap area A_f using the theorem of Pappus and Guldinus for a volume of revolution. Thus, the volume of the drop is given by $2\pi A_f \bar{x}$ from which d_e could be calculated, $d_e = (12 A_f \bar{x})^{1/3}$. This calculation gave a mean d_e of 5.15 mm. The larger drop diameter predicted by drop-volume measurements (5.18 mm) is consistent with the observed smaller drop formed during drop separation. This small drop is visible in Fig. 7.3. The difference between the two measurements is equivalent to a drop with a 1.33 mm diameter, close to the measured value of 1.1 mm. This small difference in d_e verifies the drops axisymmetry during freefall.
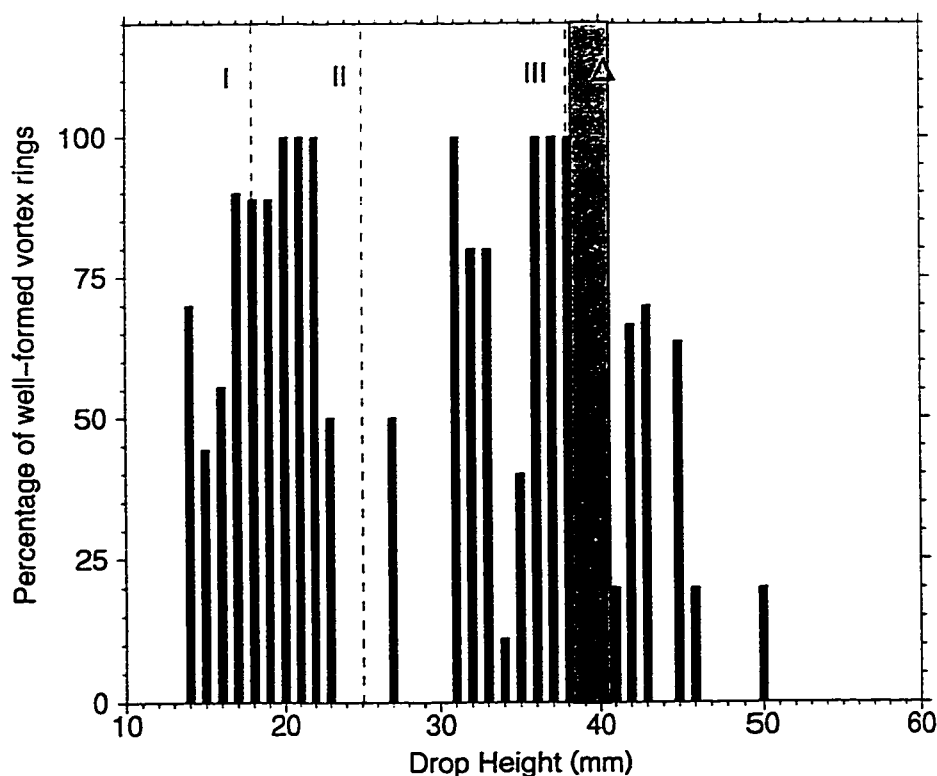
Figure 7.8: A plot of the probability of a vortex ring being formed vs. drop height. The drop height was varied by 0.1 cm increments and nine or ten experiments were recorded at each drop height. The roman numerals correspond to the first three cases as defined in text of Sec. 7.4. The gray region of width Δ is a 'notch' in the data where no vortex rings were formed; see also Fig. 7.9

7.4   Penetration depth of drop-formed vortex rings

Penetration depth of drop-formed vortex rings formed from drop impact has been reported in several publications (Rodriguez and Mesler, 1988; Keedy, 1967; Chapman and Critchlow, 1967; Thomson and Newall, 1885). In the present work penetration depth is used as calibration for experiments on vorticity creation at early times. The height of the formation tip was varied in 0.1 cm increments from 10 cm to 60 cm. At each height, nine or ten experiments were conducted and recorded on video tape. The videocamera

was mounted perpendicular to the vertical face of the tank. Its position was varied so the lens axis would roughly match the final depth of the vortex ring to avoid parallax. A careful record of the vortex ring quality was recorded. The quality was recorded as: well-formed, poor or none. Although a subjective measure, these data indicate variation in probability of vortex ring production over the range of heights used. The percentage of well formed vortex rings is plotted in Fig. 7.8.

For now, we introduce a new variable, the critical depth d_c. Critical depth was measured from a scale fixed to the edge of the tank. The critical depth was taken to be the depth where the dye within the vortex ring did not travel more than one scale unit 0.1 cm in 1 s: $U_r = 0.1$ cm/s or approximately 0.5% of the initial vortex ring speed. The vortex ring speed is discussed in Sec. 7.5.4.

This does not necessarily correspond to the overall penetration depth which we take to be the depth of the vorticity centroid of the vortex ring as $t \to \infty$. We discuss this further in Sec. 7.7.

Results of these experiments are shown in Fig. 7.9. The critical depth was difficult to judge from videotape. We address this in Sec. 7.7. Vortex rings begin to formed from impacting drops when $h = 1.4$ cm. Vortex rings form from tip heights below this but were neglected since the drop was never in freefall. The first critical depth maxima occurs at 1.8 cm with the vortex ring travelling 18 cm into the pool. At and on either side of this maxima, vortex rings are consistently formed (see Fig. 7.8).

The first minima where vortex rings form occurs at 2.7 cm. Vortex ring formation is intermittent with a 50 % chance of success, Fig. 7.8.

The next maxima occurs at 3.8 cm. The critical depth 21.5 cm is slightly greater than observed for the first maxima. Vortex rings are regularly formed from 3.8 cm but at 3.9 and 4.0 cm no vortex rings were formed. This is represented by the shaded area in Fig. 7.8 and Fig. 7.9 marked with Δ.

Both maxima occurred with $\Phi_d > 0$ but the drop was not yet fully prolate. Here the drop is passing from a configuration where the vertical and horizontal axes lengths are nearly equal to a vertically prolate configuration and is closer to the former. This agrees with the observations of Chapman and Critchlow (1967) but disagrees with Rodriguez and Mesler (1988).

A correlation between the percentage of vortex rings formed at a particular height and the critical depth is apparent when Fig. 7.8 and Fig. 7.9 are compared. This is in overall agreement with the behaviour noted in Cai (1989).
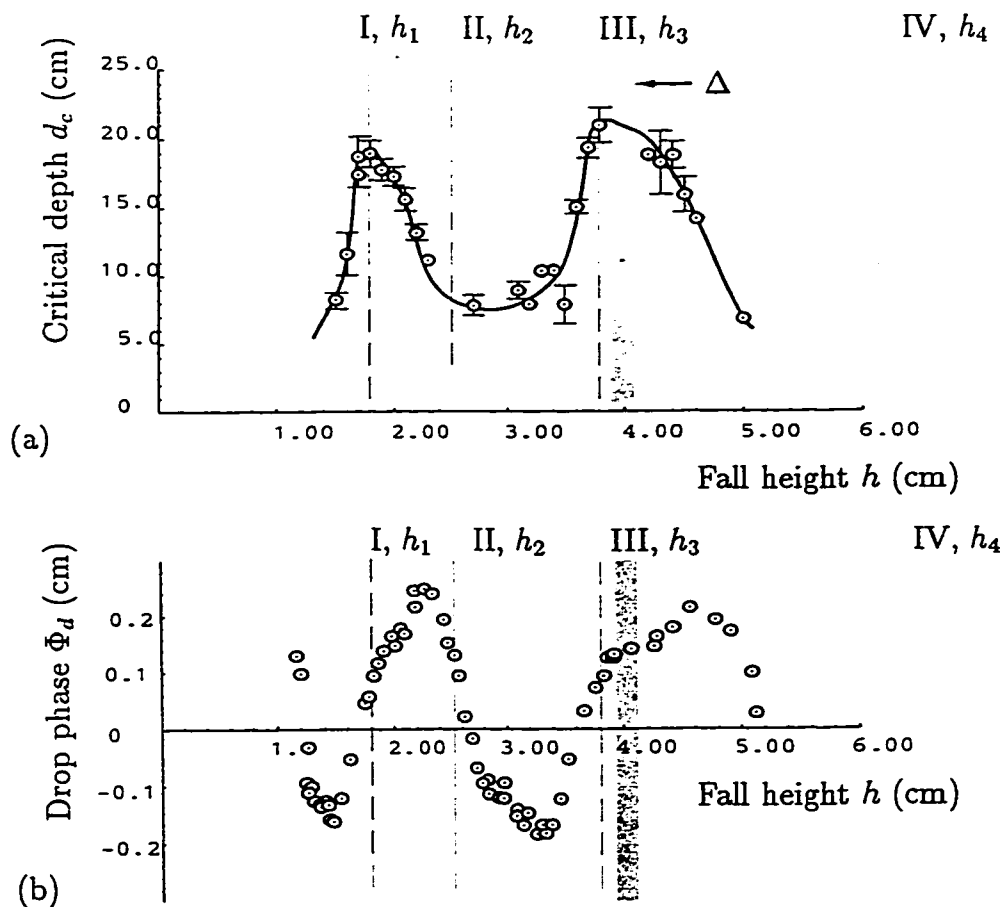
Figure 7.9: Plots of the critical depth d_c and oscillation phase Φ_d vs the fall height. The fall height is the distance from the base of the tip to the free surface in (a) and to the lowest point of the drop in (b). The gray region, denoted Δ, represents a 'notch' in the data where no vortex rings were formed.

In view of these results the following four cases were chosen for further study with 35 mm photography. Case I is the first maxima. Case II was set

at 25 cm. This is near the first minima but slightly lower. No vortex rings were observed to formed from drops released at this height. In this case we hoped to discern if vorticity is still created by drop impact and understand why no vortex rings emerge. Case III is the second maxima. This case was chosen for direct comparison with the first maxima. Case IV is the next predicted maxima based on drop oscillation phase. This case is above the We where vortex rings are known to form as predicted in Hsiao et al. (1988). As with Case II, this height was chosen to observe existence of any early-time vorticity creation. These four cases are summarized in Table 7.1, where

Case	Tip height cm	d_e mm	U cm/s	We	Fr	Re
Case I	1.80	5.1	40.3	11.4	3.2	1800
Case II	2.50	5.1	54.4	20.7	5.9	2450
Case III	3.8	5.1	72.2	36.6	10.4	3250
Case IV	7.5	5.1	104.2	76.0	21.6	4690

Table 7.1: A table of relevant dimensionless quantities. The fluid properties are: $\gamma = 72.9$ dynes/cm^2; $\rho = 0.9999$ gm/cm^3 ; $\mu = 0.0114$ gm/cm s

$$We = \frac{\rho U^2 d_e}{\gamma}, \quad Fr = \frac{U^2}{g d_e}, \quad Re = \frac{U d_e}{\nu}. \tag{7.3}$$

These nondimensional numbers all refer to the drop falling through air at impact.

7.5 The formation of vortex rings from drop impact

Understanding the creation of vortex rings from impacting drops and especially the means by which vorticity is created is important for fundamental understanding of free surface dynamics. This experiment serves as a reproducible means of identifying where vorticity is created and where the boundary layer separates from the surface and enters the bulk fluid. In this section we will describe these processes educed from photographic data.

Results from Sec. 7.4 directed selection of appropriate release heights for comparing vortex ring formation process. Several series of precisely timed 35 mm photographs were taken of the vortex ring formation process for the

four cases given in Table 7.1. Nine photographs are displayed for each case shown in Plates 1-36. The times used for each case were chosen to be representative of the vortex ring evolution and for comparison with the other three cases. The time shown below each plate refers to the delay time between the laser beam being broken and the photographs shown; for details see Chpt. 6. A table of the Plates in this chapter with their times and viewpoints is given in Table 7.2.

Case I			Case II			Case III			Case IV		
Plate	View	t (ms)	Plate	View	t (ms)	Plate	View	t (ms)	Plate	View	t (ms)
1	Side	6	2	Side	5	3	Side	5	4	Side	5
5	Side	10	6	Side	10	7	Side	10	8	Side	10
9	Side	15	10	Side	15	11	Side	16	12	Side	15
13	Side	20	14	Side	20	15	Side	20	16	Side	20
17	Side	25	18	Side	25	19	Side	25	20	Side	25
21	Side	30	22	Side	30	23	Side	30	24	Side	30
25	Side	40	26	Side	35	27	Side	35	28	Side	35
29	Side	55	30	Side	60	31	Side	55	32	Side	50
33	Side	100	34	Side	110	35	Side	100	36	Side	100
37	Top	0.0	38	Top	0.0	39	Top	0.0	40	Top	0.0
41	Top	0.5	42	Top	0.5	43	Top	0.5	44	Top	0.5
45	Top	1.0	46	Top	1.0	47	Top	1.0	48	Top	1.0
49	Top	2.0	50	Top	2.0	51	Top	2.0	52	Top	2.0
53	Top	3.5	54	Top	3.5	55	Top	3.5	56	Top	3.5
57	Top	5.5	58	Top	5.5	59	Top	5.5	60	Top	5.5
61	Top	7.5	62	Top	7.5	63	Top	7.5	64	Top	7.5
65	Top	9.5	66	Top	9.5	67	Top	9.5	68	Top	9.5
69	Top	11.5	70	Top	11.5	71	Top	11.5	72	Top	11.5

Table 7.2: A table of delay times and camera views in plates. The line next to the photographs is the location of the free surface.

Case IV

Plate 4   5 ms

Plate 8   10 ms

Plate 12   15 ms

Case III

Plate 3   5 ms

Plate 7   10 ms

Plate 11   15 ms

Case II

Plate 2   5 ms

Plate 6   10 ms

Plate 10   15 ms

Case I

Plate 1   6 ms

Plate 5   10 ms

Plate 9   16 ms

Scale
5 mm

Case IV

Plate 16   20 ms

Plate 20   25 ms

Plate 24   30 ms

Case III

Plate 15   20 ms

Plate 19   25 ms

Plate 23   30 ms

Case II

Plate 14   20 ms

Plate 18   25 ms

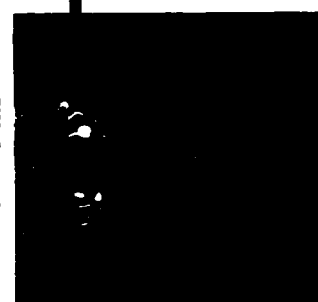Plate 22   30 ms

Case I

Plate 13   20 ms

Plate 17   25 ms

Plate 21   30 ms

Case IV

Plate 28   35 ms

Plate 32   50 ms

Case III

Plate 27   35 ms

Plate 31   55 ms

Case II

Plate 26   35 ms

Plate 30   60 ms

Case I

Plate 25   40 ms
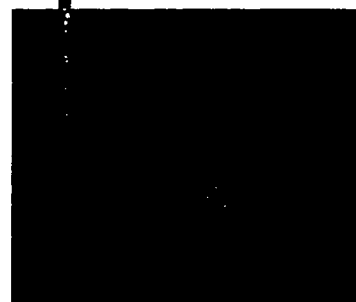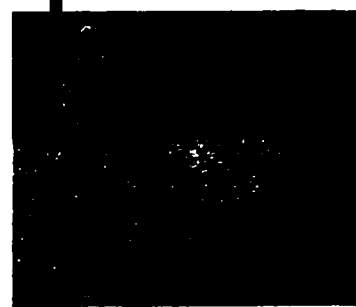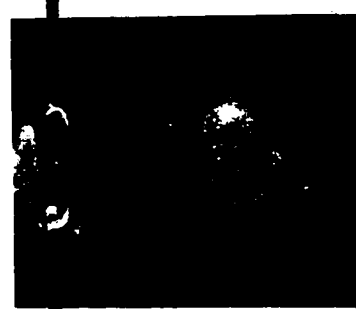
Plate 29   55 ms

Case IV

Plate 36   100 ms

Case III

Plate 35   100 ms

Case II
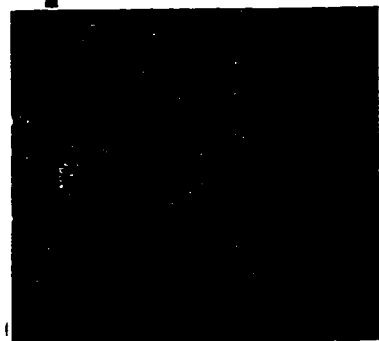
Plate 34   110 ms

Case I

Plate 33   100 ms

Case IV

Missing

Plate 40

Plate 44   0.5 ms

Plate 48   1.0 ms

Case III

Plate 39   0.0 ms

Plate 43   0.5 ms

Plate 47   1.0 ms

Case II

Plate 38   0.0 ms

Plate 42   0.5 ms

Plate 46   1.0 ms

Case I

Plate 37   0.0 ms

Plate 41   0.5 ms

Plate 45   1.0 ms

Case IV   Plate 52   2.0 ms   Plate 56   3.5 ms   Plate 60   5.5 ms

Case III   Plate 51   2.0 ms   Plate 55   3.5 ms   Plate 59   5.5 ms

Case II   Plate 50   2.0 ms   Plate 54   3.5 ms   Plate 58   5.5 ms
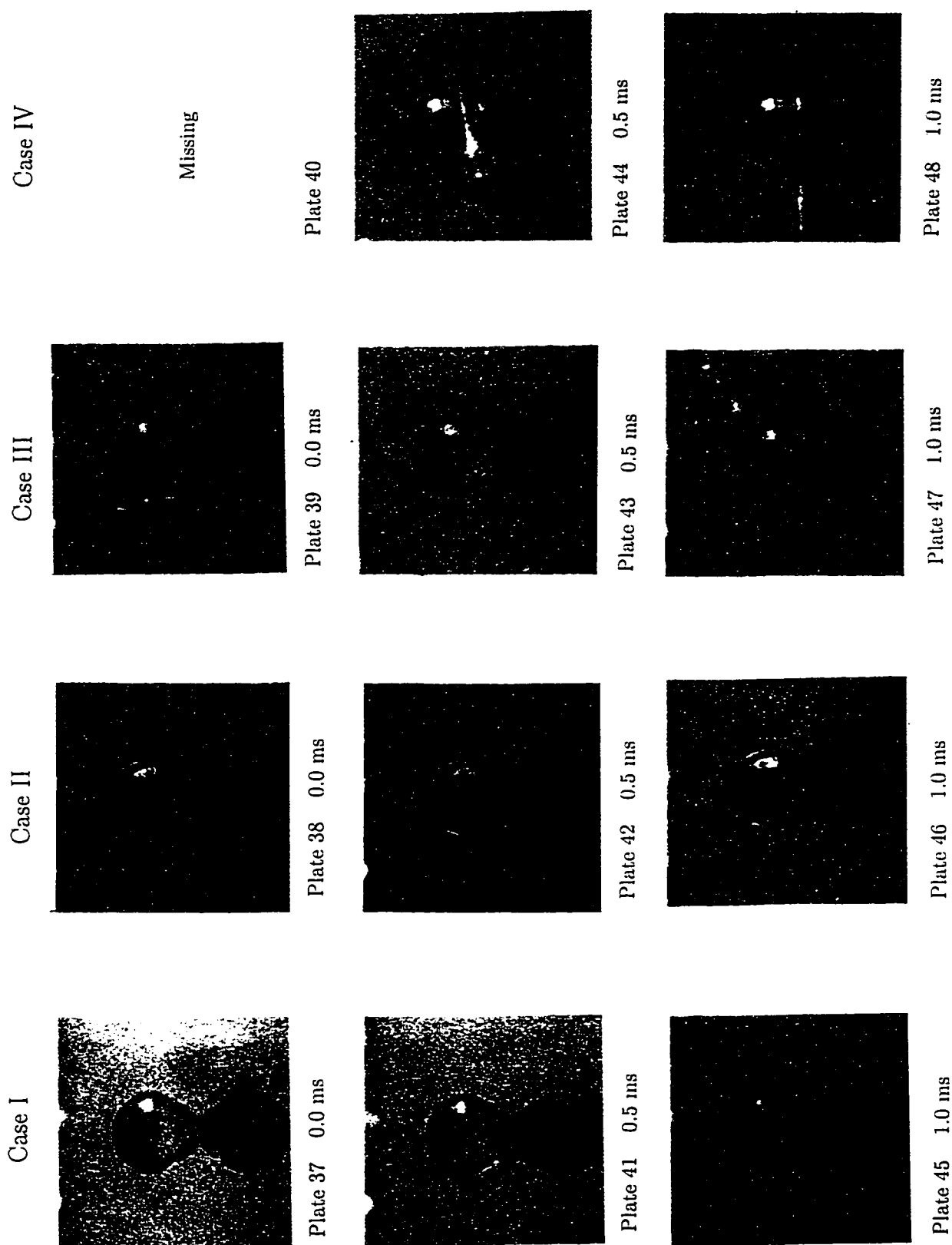
Case I   Plate 49   2.0 ms   Plate 53   3.5 ms   Plate 57   5.5 ms
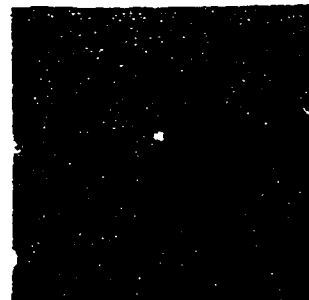
Case IV

Plate 64   7.5 ms

Plate 68   9.5 ms

Plate 72   11.5 ms

Case III

Plate 63   7.5 ms

Plate 67   9.5 ms

Plate 71   11.5 ms

Case II
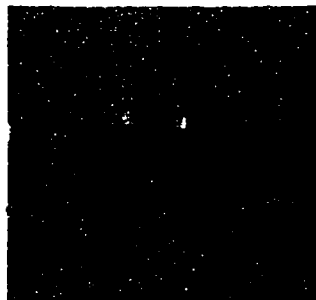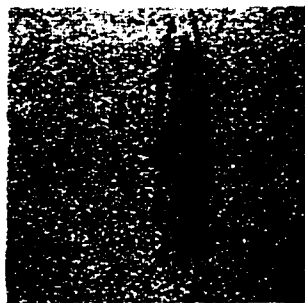
Plate 62   7.5 ms

Plate 66   9.5 ms

Plate 70   11.5ms

Case I

Plate 61   7.5 ms

Plate 65   9.5 ms

Plate 69   11.5 ms

7.5.1 Vorticity creation

The creation of vorticity and formation of vortex rings is most easily described by separating the process into the initial stage which includes the drop in free-fall and four subsequent stages. It is most convenient to classify the four impact cases (Cases I–IV) considered in terms of the geometries observed in the photographic data since the times when these geometries occur change for each Case. Period A refers to early times $O(1ms)$ after impact. In this stage the diameter of the ring of contact expands outward from an initially small 'contact patch' assumed to be much smaller than the dimensions of the drop to roughly the drop diameter. Period B refers to times following Period A and until the drop has penetrated into the pool so that the surface is approximately flat. Period C refers to times during which an impact crater forms until Period D. Period D refers to times after the impact crater has reached its maximum depth and its motion and concavity reverses.

The sign of azimuthally-directed ω will be assigned as follows. Counterclockwise vorticity in the right hand half plane is assumed positive. Hence, the primary vortex ring is formed from positive ω. Negative or 'countersigned' vorticity is clockwise directed vorticity in the right hand half plane.

Initial contact

When the drop first contacts the pool there are two regions of essentially irrotational flow: the quiescent pool and the falling drop assumed to be in a state of uniform translation. The validity of assuming the drop to be irrotational is addressed in the following four paragraphs.

Several critics have suggested that vorticity which forms the vortex ring is created by drag on the falling drop. We believe this is false for the following reasons.

Experimental measurements of internal circulation in the drop show this to be very small—$O(1\%)$ of the translational velocity—even for drops at terminal velocity, (Pruppacher and Beard, 1987). The drops used in the present experiments are only in free-fall for a very short time so it is doubtful that they will acquire much internal circulation from air drag. Also, even if the vorticity was created in free-fall, we would still not have a clear description of the vorticity creation process at the air-drop interface.

Secondly, vortex ring production very similar to what is observed in the present experiments occurs for pendant drops which just come in contact

with the pool. These drops are never in free-fall and will not experience drag. In the pendant drop case, the entire vortex ring creation process is driven by the coalescence of the static liquid drop with the quiescent pool.

A third possibility not suggested by anyone before is creation of vorticity at the moving drop boundary while the drop oscillates in free-fall. Although often considered to be an irrotational motion, the free surface of an oscillating drop must obey the same boundary condition derived in Chpt. 2. Thus, surface rotation will require vorticity to be present since the principal axis of strain aligned n on the surface of the drop will have to rotate. This is unlikely to be the principal effect since just-touching drops do not oscillate and still produce similar effects. Also, since drops do oscillate as they fall, this implies that n rotates to produce both signs of vorticity, although experiments always produce vortex rings with the same predominant sign of vorticity such that the vortex rings travel into the pool.

With the assumptions of irrotational flow stated above, the circulation about a material circuit shown in Fig. 7.10 is zero. This observation is due to Creswell and Morton (1995). This also holds true for any reducible circuit within this region. Thus, by Stokes' theorem, the vorticity in this region is initially zero. Since the fluid within this region is assumed to possess homogeneous material properties, vorticity can only be diffused into the interior region from the boundaries and it is here where we look for the vorticity creation mechanism [1]. Creswell and Morton (1995) used the stress boundary condition—similar to that discussed in Chpt. 2—to deduce the level of vorticity required at the free surface. They argued that the vorticity level is set at the free surface and is then diffused through the boundary. These authors were hindered by the form of equations used by them when their paper was written. Their starting equations were those which appear in Batchelor (1967) given in generalized three-dimensional coordinates.

As we pointed out in the closing to Chpt. 2, the stress boundary condition at a free surface does not explain the details of how the vorticity is actually created. The analysis in Chpt. 4 of torques shows that torques are applied to fluid elements at the interface through the combined action of viscous torques arising from viscosity gradients and a density-gradient-viscosity-gradient coupling mechanism. This is consistent with the sign of vorticity predicted by the free surface stress boundary condition (see Sec. 4.2.5). Thus, when we

---

[1]For a general discussion of the circulation theorem we refer the reader to Truesdell (1954, Chpt. IX) and Batchelor (1967, p. 269)

speak of vorticity creation, we assume that sufficient vorticity has been created to match the level of vorticity at the surface required by the sharp interface model, Eq. (3.10).
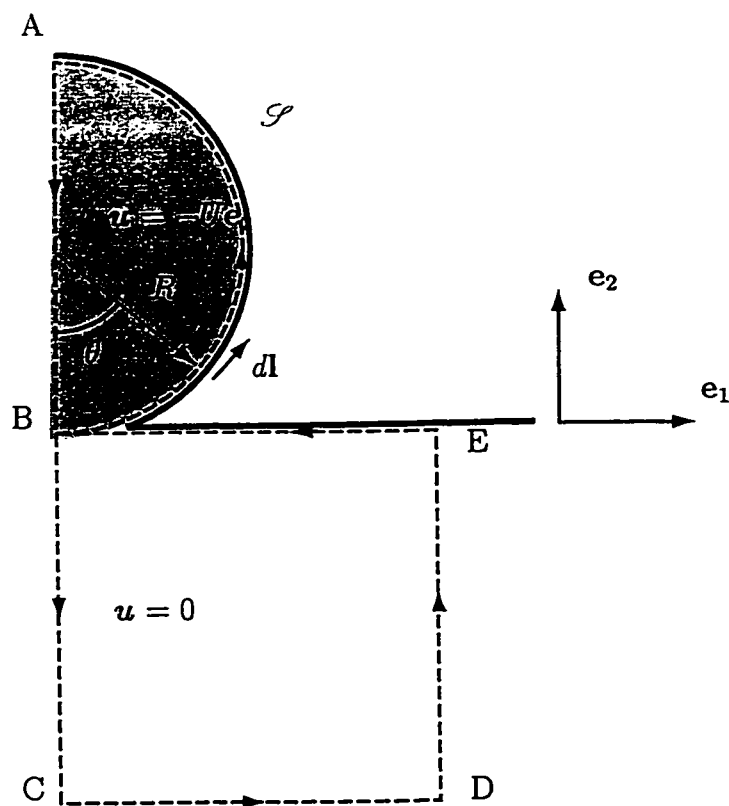
$$\Gamma = \oint u \cdot dl = \int_A^B + \int_B^A = 2UR + \int_0^\pi -U\sin\theta r d\theta = 0$$

Figure 7.10: Sketch of a fluid drop at the moment of impact with a pool. The shaded region represents the drop fluid, the dark line the fluid interface. The dashed line is a material curve around which the circulation is zero at the moment of impact.

Period A

We begin by comparing vortex ring formation and onset of instability for the two cases producing most penetrating vortex rings — Case I and Case III

— over the four time periods given above. Some relevant comments on Case II and Case IV are included in the following sections but we will leave the greater portion of this discussion to their separate sections: Sec. 7.5.2 and Sec. 7.5.3.

In all four cases vorticity appears in the bulk flow very soon after the drop and pool first touch. At times less than 5 ms — before much of the dyed drop fluid has entered the pool — there appears to be vorticity visible at the interface where dyed fluid from the drop meets the undyed fluid of the pool. This is suggested in Plates 1, 2 and 3. Assuming vorticity is present it is likely in the form of a vortex sheet originating at the surface. This is consistent with observations made by Shankar and Kumar (1995) for pendant drops and the conjecture of Creswell and Morton (1995) for impacting drops. Also, in Plate 2, a secondary distribution of dye appears on the bottom of the dye-pool interface which is rolling up at its circumference as well. We note that while Plate 4 is taken at the same delay times as the previous three plates the drop penetrates the pool faster and it appears to be more similar to the lower impact velocity drops at later times.

If vorticity is present in the bulk fluid at such early times we should look for a mechanism before these times which explains creation of at least some of the vorticity. Also, appearance of the vortex sheet roll-up in the bulk fluid indicates the boundary has separated from the surface at an earlier time. Photographs at early times from below do not reveal much information since much of the flow is obscured. We can get some additional information by comparing photographs of drops taken from slightly above during the first moments of impact shown in Plates 37-72.

We idealize the impact process as the coalescence of an initially spherical drop with a plane surface, Fig. 7.11(A). Initially the drop and the pool are irrotational, Fig. 7.10. As the drop first touches the pool the interfaces merge and the ring of contact quickly pulls to the sides; from the dotted line to the solid line in Fig. 7.11(B). This process is visible in the photographic Plates taken of the drop impact viewed from above the surface, Plates 37–72. During Period A, the surface normal at points on the lower surface of the drop quickly rotates. Some elements of the drop surface will initially be pointed vertically down and in the first 1–2 ms the normal affixed to these particles will be rotated to point slightly upwards. The sign of vorticity required to match the vanishing tangential stress Eq. (3.10) is consistent with what is observed in the vortex ring.

Predicting the sign of vorticity in this way is similar in spirit to the method

used in Peck and Sigurdson (1994). There, however we were limited by the steady-surface result from Batchelor (1967). In the same way Creswell and Morton (1995) interpreted vorticity creation using these relations but were restricted to a specialized stationary toroidal coordinate system where it was difficult to interpret the moving interface. The results derived in Chpt. 2 using convected coordinates greatly simplify the interpretation for unsteady interfaces.

Also, our photographs from below and, more convincingly, those published by Creswell and Morton (1995) show undyed fluid from the pool climbs · up the outside of the original dyed drop. This behaviour is also observed by Dooley et al. (1997) for stationary drops just touching the surface. This being the case requires the pool surface to be lifted near the drop causing the surface to rotate. Considering the sign of $\dot{n}$ in this case requires vorticity of opposite sign to that of the vortex ring's to be created. This is shown schematicliy in Fig. 7.11 b. This conclusion has not been reached by previous authors. Since the fluid beneath the pool at this point carries no tracers boundary layer separation is invisible unless dyed fluid is entrained.

This may explain the occasional appearance of a large-diameter dyed ring visible in Plate 2 at the outer edge of the impinging drop where the pool surface is almost flat again. The dyed ring's diameter increases with time while starting near the interface, which is consistent with countersign vorticity (see Plate 6, Plate 10). The presence of countersign vorticity is important for our discussion of possible vortex instabilities in Sec. 7.6. As noted earlier, observing this ring is dependent on dyed fluid being entrained by the countersign vorticity as it rolls up.

We can estimate the level of vorticity as follows. From Chpt. 2: $\omega = 2n \times \dot{n}$. We know from the photographs taken from above that n will rotate by $\pi/2$ at some of the points on the interface in the first 1 ms (see Plates 37–48). This gives $\omega \sim 2(\pi/2)(10^{-3}\ s) \sim 3000\ s^{-1}$. Of course this is an average over the first 1 ms and this value may be much higher at earlier times.

Period B

At the beginning of period B, the contact ring has expanded to the diameter of the drop and drop fluid enters the pool (see Plates 48, 50, 51, 53). Creswell and Morton (1995) base their vorticity generation arguments on this period of the flow. Here they argue that drop fluid passes over regions of high
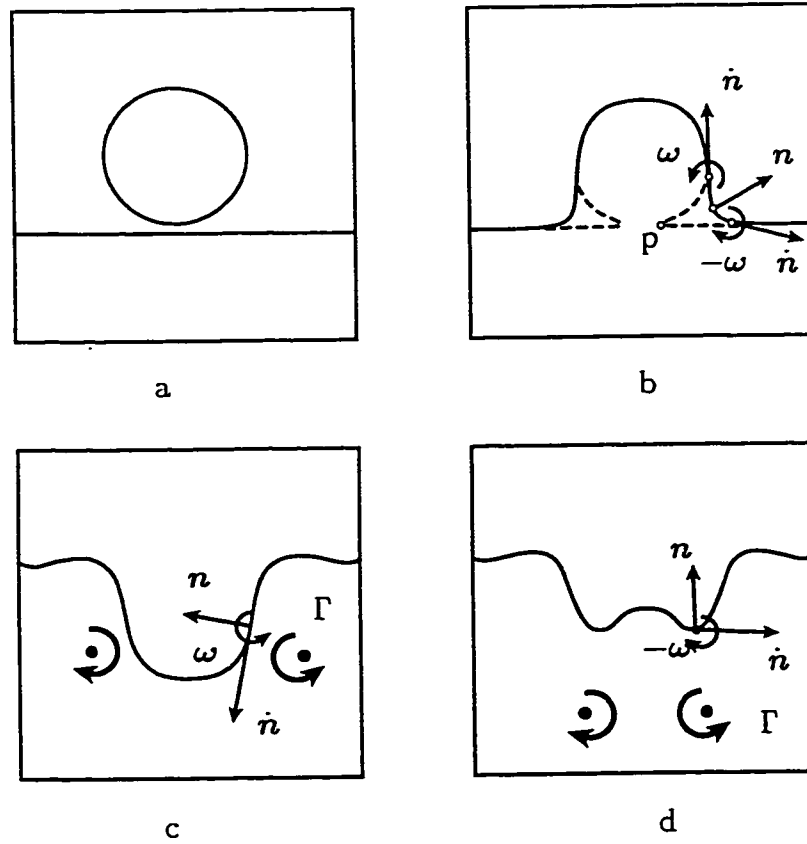
Figure 7.11: Sketch of the vorticity creation process

curvature of the free surface as the drop drains into the pool. This argument is based on their experimental photographic data taken of dyed drops from above the pool. Our data indicates that the dyed fluid does not pass over the region of high curvature at the base of the drop. Rather, it seems that the boundary layer has separated further up the walls of the dyed fluid drop. This is indicated in the photographic data given in Creswell and Morton (1995) as well where demarcation of the original pool surface and the drop surface is marked with the boundary of particles originally distributed on the pool surface. This would mark a separation point of the boundary layer, Fig. 7.12 a.

This is reconcilable with our vorticity generation model since the surface is undergoing a rapid rotation consistent with the sign of the primary vorticity.
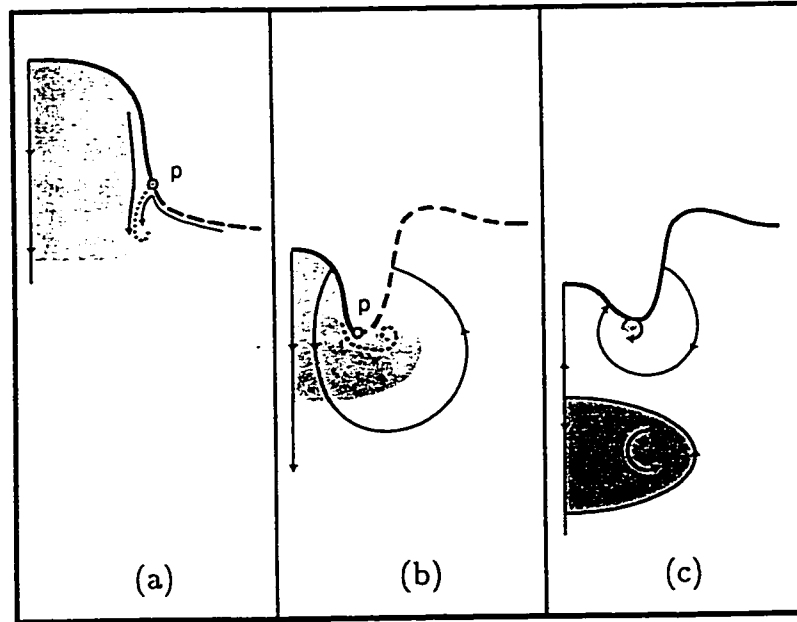
Figure 7.12: Sketch of boundary layer separation: (a) The boundary separates from the surface near a stagnation point p; (b) Vortex sheet rollup, the impact crater still serves as a source of vorticity; (c) Dye is entrained by countersign vorticity which is formed from the reversing impact crater. Hypothesized countersign vorticity formed in Period A not shown.

The rotating surface acts as a source of vorticity which diffuses into the drop fluid as it drains into the pool. Boundary layer separation is indicated as discussed above.

We also mention Shankar and Kumar (1995) who use a less sophisticated argument which does include vorticity generation. Here they suggest that a *microjet* is ejected into the bulk fluid by the coalescing drop. They liken this to the formation of vortex rings from submerged orifices. This model does not account for the very transient nature of the free surface in this phenomenon.

Period C

Drop impact forms a crater whose geometry is dependent on impact velocity and drop geometry (Peck and Sigurdson, 1995). The motion of the impact

crater geometry greatly influences vortex ring creation.

After the trailing edge of the drop becomes level with the free surface a crater begins to form with a convex region in the centre (see Fig. 7.11c). The convex region travels into the pool as the crater forms. At the outer edges of the convex region the surface is rapidly turning over to form the walls of the crater. Rotation of n at all points in the crater is consistent with positive signed vorticity and will be the highest at the transition region described above. Time to deepest crater formation is between 20 and 25 ms in Case I and Case III. The level of vorticity at the boundary will be similar to that described in Period A.

Period D

In Period D, the impact crater begins to reverse. Now another convex region forms in the centre of the impact crater but its motion is reversed when compared to the convex region observed during Period C.

By this time the primary vortex ring has moved away from the surface. At the outer edge of the reversing impact crater the surface normal is rotating rapidly acting as a source of negative-signed vorticity. The appearance of counter-sign vorticity is visible in the reversing impact crater forming vortex rings at the surface of opposite sign to the primary vortex ring. The sign of this ring can be deduced easily since its radius expands under the influence of its image vortex required by the presence of the free surface (Peck and Sigurdson, 1994).

We previously reported that the earliest observed formation of countersign vorticity was in the reversing impact crater and concluded no other counter-sign vorticity was formed (Sigurdson and Peck, 1994). Our arguments earlier in this section suggest that countersign vorticity may be created during the first period of coalescence $t < 1$ ms which is sooner than previously thought. This is especially important in view of the role of counter-sign vorticity possibly being responsible for an instability observed on the vortex ring core that leads to the three-dimensional structure. The nature of this instability is unclear (Sigurdson and Peck (1994), Appendix D). It may fall into the category of a Rayleigh centrifugal instability. The Rayleigh centrifugal criterion is that a necessary and sufficient condition for *stability* is that the square of the circulation does not decrease anywhere (Drazin and Reid, 1991, p.69). Hence, the presence of two signs of vorticity invalidates this condition and is unstable. Thus, the presence of countersign vorticity at early stages

is important because it could trigger the instability.

7.5.2 Case II: Minimum penetration and Subcritical We

Case II drop impacts do not produce well-formed vortex rings, (see Fig. 7.8). At this height, $\Phi_d \approx 0.12 > 0$ and going to $\Phi_d < 0$ so drops are becoming vertically oblate from vertically prolate but are still prolate as shown in Fig. 7.7. As Plate 38 shows, the drop is pear shaped at impact. As the drops impacts the pool, a wider impact crater forms than in Case I or Case III: (see Plates 2, 6, 10, 14). A vortex ring forms in a way similar to Cases I and III and is visible at the base of the impact crater (see Plate 18). As noted by Rodriguez and Mesler (1988), the vortex ring does not move away from the impact crater before the reversing flow into the impact crater retards its forward motion. During the crater reversal countersign vorticity of will be generated in the reversing impact crater. The primary vortex ring will remain near a source of countersign vorticity possibly annihilating some vorticity or at least reducing the net local circulation.

A large amplitude instability forms between 30 ms (Plate 22) and 35 ms (Plate 26) and the initially axisymmetric distribution of vorticity now becomes a tangle of vortex tubes which remains near the surface. In some cases a vortex ring does emerge from this tangle but none were captured in the photographs.

7.5.3 Case IV: High We case

The drops studied in Case IV have $We = 76$ as shown in 7.1. These drops do not form vortex rings propagating through the pool which is consistent with the predictions in Hsiao et al. (1988). Many recent works have concluded that vorticity is not created at these higher We and have sought explanations for this behaviour. We will point out some flaws in this conjecture.

Creswell and Morton (1995) and Rein (1995) suggest that in the very early moments of impact—roughly equivalent to our Period A—the impacting drop flattens at impact and contact is made at several points on the interface. This is referred to as surface destruction. They go on to say that the vorticity generation mechanism will no longer operate after the surface is destroyed. This is plausible for regions where there is surface destruction, but this is limited to times no greater than those discussed in Period A. Creswell and Morton (1995) however, base their vorticity generation explanation on Period

B which will still act as a source of vorticity regardless of whether there was surface destruction or not.

Our data shows that vorticity *is* produced from high-*We* drops. Plate 4 shows a vortex ring that forms very near the surface and appears to have evolved in a similar way as for lower *We* drops studied in these experiments. Plate 8 and Plate 12 show that the impact crater rapidly swells outward near its base. This appears to be an extension of the crater bulging observed in Case III visible in Plate 11. Plate 12 and 18 show a large bubble—near the size of the drop—forming as the impact crater neck pinches off. This large bubble appears to oscillate between 20 and 25 ms (see Plates 16 and 20). During this period, the vortex ring seen rolling up in Plate 4 at 5 ms is no longer seen. The drop fluid gets divided by the bubble growth. Some of the dyed fluid of the drop originally associated with the vorticity appears to be entrained into the wake of the bubble (see Plates 20, 24 28). Some of the dyed fluid appears to be in front of the bubble at 20 ms (Plate 16), although this is difficult to interpret because of the reflections. The large bubble travels into the pool before eventually rising to the surface. At 50 ms some dye is below the bubble as it has begun to rise. Plate 36 shows dye that has propagated into the pool and has formed a weak vortex ring.

The large bubble formation process discussed here does not seem to have been reported before. This phenomenon is very different from very high speed drop impacts where a bubble is formed from a fluid sheet rising from the surface Engel (1966).

7.5.4 Estimates of surface vorticity

The level of surface vorticity is checked with the following: estimates of the level of vorticity required in the separating boundary layer and estimating the vortex rings vorticity.

Boundary layer approach

This is essentially the technique used in Creswell and Morton (1995). Here they reasoned that the level of vorticity can be estimated after knowing the jump in velocity $[u]$ across the boundary layer. The velocity difference arises between the drop fluid rushing into the pool and the pool fluid assumed to be stationary. The integrated amount of vorticity through the shear layer of

thickness l can be estimated from this velocity jump:

$$\int \omega dy = -\int_0^l \frac{du}{dy} dy = -\int_{u_1}^{u_2} du = u_1 - u_2 = [\![u]\!]. \qquad (7.4)$$

We recalculate these estimates using by estimating the surface vorticity from the rate of rotation of the surface normal affixed to a material particle on the surface. This differs significantly from their approach which was based solely on surface curvature and does not include effects of surface rotation.

We assume the difference in velocity across the separated boundary layer will be $O(U)$, where U is the translational speed of the drop at impact. This means that the integrated amount of ω through the boundary layer will follow $U \sim \omega l$. Assuming the boundary thickness grows like $\sqrt{\nu t}$ gives $\omega \sim U/\sqrt{\nu t}$. Now $t \sim 2\text{ms}$ and $U = 40\text{cm/s}$ (Case I) so that $\omega \sim 8000\,\text{s}^{-1}$. This is higher than our earlier predicted estimates of ω on the surface. The value used for U is likely too high since the drop fluid is slowed at impact. Also, the vorticity level predicted at the surface is based on an average $[\![\dot{n}]\!]$ and may be much higher at the first instants.

Ideal vortex ring velocity approach

Estimates of the vorticity level in the vortex ring can also provide some information. Assuming the equation for a vortex ring's velocity U_r in an ideal fluid can be used to estimate U_r in a real fluid at early times

$$U_r = \frac{\Gamma}{4\pi R} \left[\ln\left(\frac{8R}{\varepsilon}\right) - \frac{1}{4} \right]. \qquad (7.5)$$

As mentioned in Chpt. 1, this formulae is originally due to Kelvin and appears in Helmholtz (1867), a derivation can be found in Lamb (1932) and a more complete treatment in Saffman (1992)[2]. Here, R is the vortex ring radius, ε the core radius and Γ circulation . Hence, we require estimates of these three values to calculate U_r.

---

[2]In a personal discussion, Professor Saffman pointed out to me that derivations of Eq. (7.5) are rarely found in the literature. In fact he thought that derivations were only to found in Lamb (1932) and his own book (Saffman, 1992). I subsequently found another derivation in Shivamoggi (1985), unfortunately this result is incorrect! As it stands the only correct derivations are in the citations above.

Assuming ω is uniform through ε the vorticity level follows from the circulation, $\Gamma = \omega \pi \varepsilon^2$. Substituting this result in Eq. (7.5) gives:

$$\omega = \frac{4U_r R}{\varepsilon^2} \left[\ln\left(\frac{8R}{\varepsilon}\right) - \frac{1}{4} \right]^{-1} . \tag{7.6}$$

Now estimates of ω depend on U, R and ε.

U_r was calculated for Case I and III from multiple-exposure photographs using centred differences: $(U_r)_i = (x_{i+1} - x_{i-1})/(2\Delta t)$. Each photograph captured 10 images separated by 40 ms intervals. A plot of U_r vs time is presented in Fig. 7.13. From this figure we chose a typical early-time $U_r = 22$ cm/s.

The vortex ring radius was measured from 35 mm photographs. This distance was taken to be half the centre to centre distance of the spirals visible in photographs. The most difficult estimate is the core radius. As a lower bound we use the diffusion length $\varepsilon = \sqrt{4\nu t}$ where t is assumed to be the time from impact. With ν given earlier this gives $\varepsilon = 0.044$ cm. As an upper bound we resort to estimates from concentrated dyes regions visible in photographs and use 0.1 cm. These two core estimates yield $\omega = 3700s^{-1}$ and $\omega = 800s^{-1}$, ω decreasing with increasing core size. Estimates of ω based on $\dot{n}$ in Sec. 7.5.1 give $\omega \sim 3000s^{-1}$ which is within the bounds on ω estimated from Eq. (7.6).
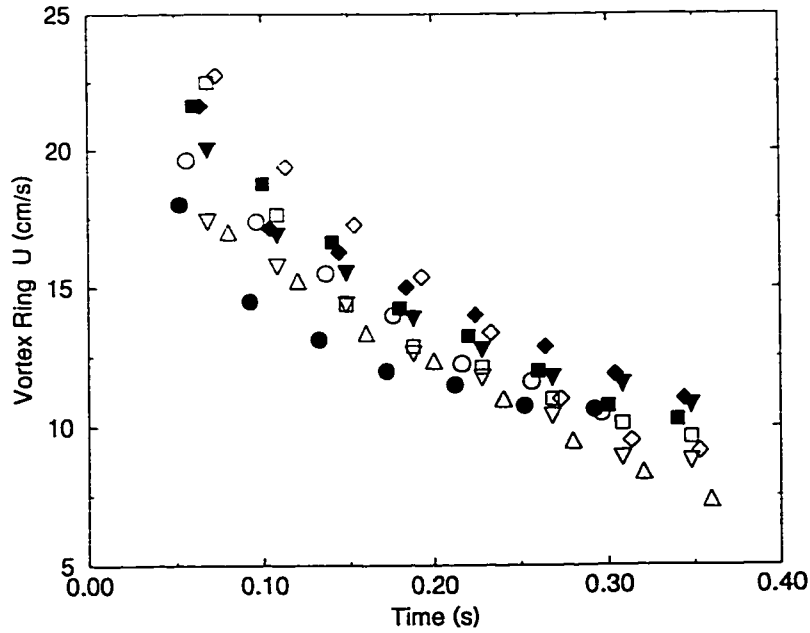
Figure 7.13: Vortex ring speed vs time. Unfilled symbols correspond to Case I, filled symbols Case III. The different shapes correspond to individual multi-exposure photographs

7.6 Vortex Instabilities

This section discusses vortex instabilities which evolve during the first 100 ms after impact.

A large-scale instability is often observed which has been compared to the structure in the Atomic Blast under precise circumstances for both cases (Peck and Sigurdson, 1994). Observation of this structure was originally reported for a 4.4 mm diameter drop in Okabe and Inoue (1961). Detailed observations of this structure's evolution for smaller drops appear in Peck and Sigurdson (1994) and Peck (1993). There we observed that an axisymmetric distribution of lobes—or 'petals'—composed of vortical fluid evolves from the vortex ring. These petals are composed of vortical fluid although a recent paper suggested otherwise (Rom-Kedar et al., 1990; Shariff and Leonard, 1992). Proof of their vortical nature is educed from the observed reconnection process at the tips of the petals. The tips of the petals pinch off to form small

vortex rings travelling away from the central axis. While this was reported in Peck (1993) the first photograph of this appears in Plate 29.

The type of instability responsible for this structure is of particular interest and is addressed in (Sigurdson and Peck, 1994) which is included as Appendix D. That paper concludes the instability is likely due to a Taylor-Görtler centrifugal instability or Bernal-Roshko type of instability rather than a Widnall-type core instability.

In this section we present new observations of the early-time instability formation and comment on possible sources of countersign vorticity necessary to satisfy Rayleigh's criterion.

7.6.1 Early-time instability: Case I

Our experiments show consistent formation of the large-scale structure mentioned above in Case I. A time sequence of its evolution is recorded in Plates 21, 25, 29 and 33. The earliest sign of instability in this case appears in the range 16–25 ms: Plates 9, 13 and 17. Plate 17 (25 ms) shows an azimuthal distribution of dye along the crater wall just in the wake of the forming vortex ring. This sheet of dye is still visible in the wake at 30 ms, Plate 21. A similar but more prominent form of this instability is visible in Case III. From 40–55 ms a low-wavenumber instability forms on the ring and large-scale structures escape the vortex ring. These structures form petals visible at later times (see Plate 33).

7.6.2 Early-time instability: Case III

From 5–10 ms a tiny azimuthal instability is visible on the circumference of the dyed fluid just entering the pool (see Plates 3 and 7). At 15-20 ms an azimuthal distribution of 16–20 spike-like structures is visible near the crater wall and in the vortex ring wake (see Plate 11 and Plate 15). The spikes appear to travel away from the crater walls from 20-25 ms (see Plates 19 and 23). This is surprising since this motion is opposite to the local flow direction induced by the vortex ring. A possible explanation is that these structures are hairpin line-vortices convecting away from the surface under their self-induction. The wave number drops to four at 25 ms. At 30 ms, a fine-scale instability appears over the entire ring. This instability grows begins to be deposited into the wake of the ring (see Plates 27, 31, 35).

The large scale structures observed in Case III are not observed: instead, finer-scale features is shed into the wake (see Plates 23, 27, 31 and 35).

The source of this instability may be a centrifugal instability. In Peck and Sigurdson (1994) we reasoned that countersign vorticity could be introduced into the flow from the reversing impact crater. This would be too late for the source of the instability observed here. But, as we have argued in Sec. 7.5.1 a possible source of countersign vorticity exists at the earliest stages of impact. Here the upward motion of the free surface at first impact was thought to be a possible source of countersign vorticity. The presence of countersign vorticity is supported by observations of Case II and is responsible for the relatively large amount of dye visible in countersign vortex rings at the free surface in that case at later times.

As mentioned earlier, Case II vortex rings also become unstable but disintegrate; this appears to be driven by the flow into the reversing impact crater.

7.7 Notes on the final decay

The critical depth as defined above does not necessarily mark the end of the vortex ring motion. Indeed, it is not at all obvious that a vortex ring should necessarily come to a stop. Multi-exposure 35 mm photographs taken at 5 s intervals in subsequent experiments showed the vortex ring to be still moving slowly downward $O(> .1cm/s)$ even after 20 s. This is expected since—in an unbounded viscous fluid—the downward-directed hydrodynamic impulse I is conserved in time.

Only scattered observations of this long-time behaviour have been reported. Shankar and Kumar (1995) noticed similar behaviour for vortex rings produced from small coalescing drops. They were very surprised by this behaviour and felt it was a phenomenon peculiar to the smallest drop size they used: 2.5 mm. They did not observe this sudden growth behaviour in larger vortex rings such as those used in the present experiments. This is likely because of the increased time necessary for vorticity to diffuse to the vertical axis of symmetry for the larger vortex rings. By this time the vortex motion in their experiments appears to be dominated by instabilities forming on the vortex ring similar to those observed by Thomson and Newall (1885). From our experience this instability seems to be density driven and can be delayed substantially by using less concentrated dye. Also, as Keedy (1967)

pointed out the penetration depth and the onset of vortex ring instability is strongly affected by thermal currents in the reservoir. His solution was to try and find places in the reservoir where the pool appeared to be still. In our experiments thermal gradients were eliminated using the cooling bath and enclosed test cell as described in Chpt. 6.
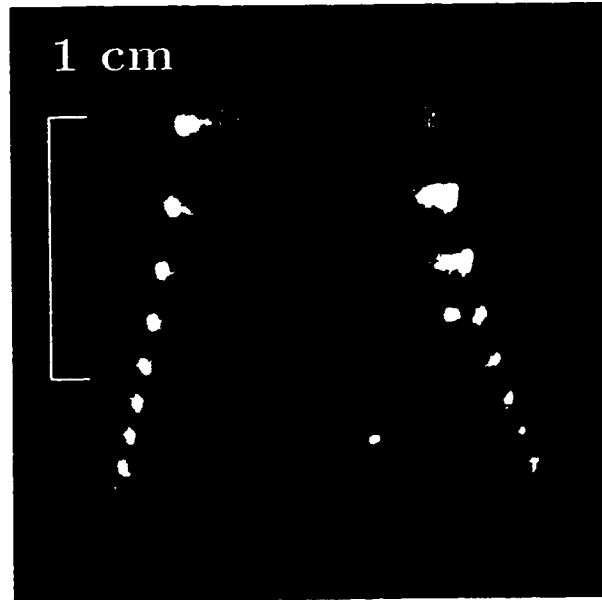

Figure 7.14: Multiple-exposure photograph of a vortex ring. Each image is is recorded at 5 s intervals beginning 20 s after impact

In an ideal fluid a vortex ring retains its size and will not stop its forward motion. In a viscous fluid, energy will be dissipated and the vortex ring will become less energetic. This is the view Anilkumar et al. (1991) used as a basis for scaling arguments to predict the penetration length of vortex rings produced by coalescing drops. Shankar and Kumar (1995) note the difficulty with assigning a true penetration depth to a vortex ring and define the critical depth as the depth to which the vortex ring travels before slowing to 0.2 cm/s.

A clue to the late-time behaviour of the vortex ring is the expansion of the vortex ring to several drop diameters over a short distance beginning at times near 20 s after impact. A typical multi-exposure photograph of this is shown in Fig. 7.14. At this time, the forward motion of the vortex ring is

very slow $O(.1cm/s)$. In some cases, the diameter increases to dimensions on the order of the test cell's dimension.

A possible explanation is the onset of asymptotic drift as predicted by Rott and Cantwell (1993b,a); Shariff and Leonard (1992); Cantwell and Rott (1988); Kambe and Oshima (1975). In these analyses the large time estimates of the Navier Stokes equations are given using asymptotic expansions. Unlike Stokes flow solutions, these solutions include estimates of convective terms and hence the transport of vorticity.

In a vortex ring context asymptotic drift describes the vorticity centroid motion at large times when the vortex core diffuses to dimensions on the scale of the vortex ring diameter. To determine whether this behaviour is possible for the time scales considered we perform the following order of magnitude analysis. The core cross-sectional radius is expected to grow as $\sqrt{\nu t}$ so in the present experiments with $t \sim 20s$ and $\nu = 0.0114cm^2/s$ the diffusion length becomes $l \sim 0.48cm$. This compares well with the observed vortex ring radius—not to be confused with vortex core cross-sectional diameter—of approximately 0.5 cm at 20 s after impact.

If the core diameter is on the order of the vortex ring diameter significant cancellation occurs at the vertical axis of symmetry. Kambe and Oshima (1975) show that the ring diameter should then grow as $t^{1/2}$ to satisfy the invariance of hydrodynamic impulse I. The ring convection velocity $d\bar{x}/dt$ should then decay as $t^{-3/2}$.

To test this behaviour the dyed ring's diameter and it velocity are plotted vs time in Fig. 7.15 and Fig. 7.16. We have purposely worded this as the dyed ring and not the vortex ring. At these large times the position of the dye does not necessarily mark the location of the vorticity. In two-dimensional plane flow, vorticity diffuses in the same manner as a dye but at a much greater rate. Hence, vorticity can be diffused to regions absent of any apparent dye. This is further complicated for non-planar flows since vorticity diffuses as a vector and dye as a scalar.

Experimentally measured values of the dyed ring diameter growth compare very well with the theoretical predicted result for the vortex ring diameter growth. Fig. 7.15 shows a log-log graph of results from seven experiments. The slopes range from 0.47 to 0.57 with an average of 0.504 which agrees well with the predicted value of 0.5.

The vortex ring velocity measured from experiment does not compare as favorably to theoretical values Fig. 7.16. Our results for the exponent are -0.88 to -1.4 with a mean value of -1.25 compared to the theoretical
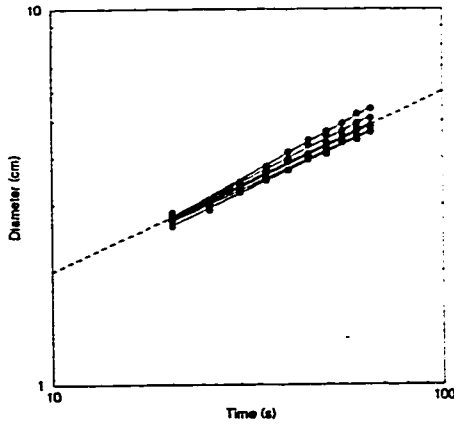
Figure 7.15: Plot of dyed ring diameter vs time for the final stages of vortex ring motion. The dashed line represents a line where $d_r \sim t^{1/2}$
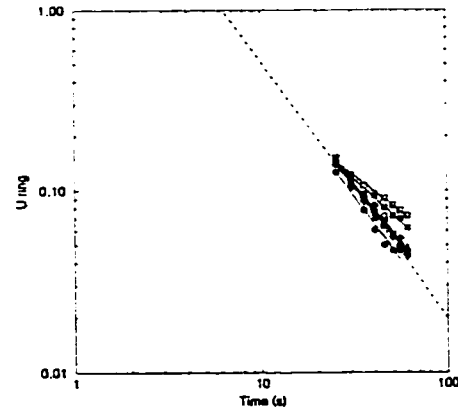
Figure 7.16: Plot of the dyed ring velocity vs time at late stages of motion. The dashed line represents a line where $\frac{d\bar{x}}{dt} \sim t^{-3/2}$

value of -1.5. These low results could be a result of several factors the most obvious being that the vortex ring may not have yet reached the asymptotic drift stage. Also, there are errors in tracking the vorticity centroid with dye although the excellent agreement with theoretically predicted diameter growth suggests otherwise. The total distance travelled by the vortex ring centroid from some time t is finite if the exponent is less than -1. As an example where the exponent in the power law fit is -1.45 so that

$$\frac{d\bar{x}}{dt} = 4.31t^{-1.45}, \tag{7.7}$$

where the factor 4.31 comes from the numerical power law fit done using Xmgr 4.0 $^{©}$. The final depth is calculated by integrating Eq. (7.7):

$$\Delta x = \int_{20\,s}^{\infty} 4.31t^{-1.45}dt = -\left(\frac{4.31}{.45}t^{-0.45}\right)\Big|_{25\,s}^{\infty} = 2.25\ cm. \tag{7.8}$$

This is slightly further than that recorded in the photographic record 1.9 cm. The greater theoretical value is expected since the photographic record does not capture the complete final motion of the ring.

7.8 Conclusions

This chapter presented detailed analysis of vortex ring creation from an impacting drop. A substantial amount of work was expended on studying the motion of the drop in freefall.

For the drop in freefall we found excellent agreement with the measured drop oscillation period of 34.0 ms and the theoretically predicted 34.2 ms period. We also found a virtual origin exists due to the complex drop separation process. The most penetrating vortex rings are formed by drops with the same phase at impact. This phase corresponds to a drop passing from vertically oblate to vertically prolate but still prolate. This agrees with the observations of Chapman and Critchlow (1967) but disagrees with Rodriguez and Mesler (1988). Penetration depth is roughly correlated with the chance of a vortex ring forming.

Vorticity creation observed at early times is consistent with predicted in Chpt. 2 and Chpt. 4. Using a sharp interface model, the level of vorticity required at the free surface estimates is predicted to be $O(3000\,s^{-1})$ at early times. This is consistent with the motion of the vortex rings produced. The surface continues to act as a source of vorticity while the impact crater forms. This feeds the separated boundary layer. This early-time behaviour is observed in the four cases studied here even for We above the critical limit.

Vortex rings are formed in Case I and III because they are able to move away from the impact crater without the upward flow from the reversing impact crater adversely affecting their motion. In Case II a vortex ring appears to form at early times in a similar way as Case I and Case III but Case II vortex rings are trapped in the upward flow due to the reversing crater. Positive vorticity in the vortex ring likely comes in contact with countersign vorticity at this time and some cancellation may occur. Only a weak vortex ring is sometimes observed.

Experimental evidence shows vorticity also appears in a similar way for drops impacting above the critical We. This is counter to arguments from several previous papers where it is argued that no vorticity creation takes place because of surface destruction. At $We = 76$ the appearance of a well-formed vortex ring is inhibited by the separation of a bubble larger than a drop diameter from the surface.

An argument for the appearence of countersign vorticity at very early times has been proposed. This is much earlier than previously thought and may be responsible for the onset of an instability since Rayleigh's centrifugal

criterion for stability is broken.

The sudden enlargement of vortex rings at long times $O(20s)$ after impact was explained: drop-formed vortex rings enter into an asymptotic drift phase. Theoretically, this implies the vortex ring diameter expands as $t^{1/2}$ and the speed of the vortex centroid should slow as $t^{-3/2}$. Experimental results showed the ring diameter enlarged as $t^{1/2}$ and that $d\bar{x}/dt \sim t^{-1.25}$. This ensures the penetration depth of the vorticity centroid is finite.

Bibliography

A. V. Anilkumar, C.P. Lee, and T.G. Wang. Surface-tension induced mixing following coalescence of initially stationary drops. *Phys. Fluids A*, 3(11): 2587–2591, November 1991.

G. K. Batchelor. *An Introduction to Fluid Dynamics*. Cambridge University, New York, 1967.

Y. K. Cai. Phenomena of a liquid drop falling to a liquid surface. *Exp. in Fluids*, 7:388–394, 1989.

Brian Cantwell and Nicholas Rott. The decay of a viscous vortex pair. *Phys. Fluids*, 31(11):3213–3224, November 1988.

D. S. Chapman and P.R. Critchlow. Formation of vortex rings from falling drops. *J. Fluid Mech.*, 29:177–185, 1967.

R. W. Creswell and B. R. Morton. Drop-formed vortex rings–the generation of vorticity. *Phys. Fluids*, 7(6):1363–1370, June 1995.

B. S. Dooley, A. E. Warncke, M. Gharib, and G. Tryggvason. Vortex ring generation due to the coalescence of a water drop with a free surface. *Exp. in Fluids*, 22:369–374, 1997.

P. G. Drazin and W. H. Reid. *Hydrodynamic Stability*. Cambridge University, New York, 1991.

F. Durst. Penetration length and diameter development of vortex rings generated by impacting water drops. *Exp. in Fluids*, 21:110–117, 1996.

Olive Engel. Crater depth in fluid impact. *J. Appl. Phys.*, 37(4):1798–1808, March 1966.

J. Hallet and L. Christensen. Splash and penetration of drops in water. *J. Res. Atmosph.*, 18(4):225–242, Oct.– Dec. 1984.

H. Helmholtz. On integrals of the hydrodynamical equations, which express vortex-motion. *Phil. Mag.*, 33(226):485–512, 1867.

Mingying Hsiao, Seth Lichter, and Luis G. Quintero. The critical Weber number for vortex and jet formation for drops impinging on a pool. *Phys. Fluids*, 31(12):3560 –3562, December 1988.

Tsutomu Kambe and Yuko Oshima. Generation and decay of viscous vortex rings. *J. Phys. Soc. Jap.*, 38(271):1443–1450, 1975.

H. F. Keedy. *Vortex Rings Formed by Free-Surface Interaction.* PhD thesis, University of Michigan, Ann Arbor, Michigan, 1967.

Horace Lamb. *Hydrodynamics.* Dover, New York, 1932.

J. Okabe and S. Inoue. The generation of vortex rings, II. *Rept. Res. Inst. Appl. Mech.*, 9(36):147–161, 1961.

Bill Peck and Lorenz Sigurdson. The three-dimensional vortex structure of an impacting water drop. *Phys. Fluids*, 6(2):564–576, February 1994.

Bill Peck and Lorenz Sigurdson. The vortex ring velocity resulting from an impacting water drop. *Exp. in Fluids*, 18:351–357, 1995.

Bill J. Peck. The three-dimensional vortex structure of an impacting water drop. Master's thesis, University of Alberta, January 1993.

H Pruppacher and K. Beard. A wind tunnel investigation of the internal circulation and shape of water drops falling at terminal velocity in air. *Quart. J. R. Met. Soc.*, 96:247–256, 1987.

M. Rein. Wave phenomena during droplet impact. In S. Morioka and L. van Wijngaarden, editors, *IUATM Symp. on Waves in Liquid/Gas and Liquid/Vapor*, pages 191–200. Kluwer, 1995.

Martin Rein. The transitional regime between coalescing and splashing drops. *J. Fluid Mech.*, 306:145–165, 1996.

Francisco Rodriguez and Russel Mesler. The penetration of drop formed vortex rings into pools of liquid. *J. Colloid Interface Sci.*, 121(1):121–129, January 1988.

V. Rom-Kedar, Anthony Leonard, and S. Wiggins. An analytical study of transport mixing and chaos in an unsteady vortical flow. *J. Fluid Mech.*, 214:347–394, 1990.

Nicholas Rott and Brain Cantwell. Vortex drift. II:The potential flow surrounding a drifting vortical region. *Phys. Fluids A*, 5(6):1451–1455, June 1993a.

Nicholas Rott and Brian Cantwell. Vortex drift. I:Dynamic interpretation. *Phys. Fluids A*, 5(6):1443–1450, June 1993b.

P. G. Saffman. *Vortex Dynamics*. Cambridge University Press, New York, 1992.

P. N. Shankar and Manoj Kumar. Vortex rings generated by drops just coalescing with a pool. *Phys. Fluids*, 7(4):737–746, April 1995.

Karim Shariff and Anthony Leonard. Vortex rings. *Annu. Rev. Fluid Mech.*, 24:235–279, 1992.

Bhimsen K. Shivamoggi. *Theoretical fluid dynamics*. Kluwer Academic, Dordrecht, 1985.

Lorenz Sigurdson. Atom Bomb/Water drop. *Phys. Fluids A*, 3(9):2034, September 1991.

Lorenz Sigurdson and Bill Peck. The vorticity generation mechanism for impinging water drops. In *Proceedings of the American Physical Society*, page 2093. American Physical Society, 1989.

Lorenz Sigurdson and Bill Peck. A drop of violence. *Discover*, page 11, May 1992a.

Lorenz Sigurdson and Bill Peck. The turbulent times of a water drop. *New Scientist*, 135(1830):18, July 1992b.

Lorenz Sigurdson and Bill Peck. Three-dimensional transition of the vorticity created by an impacting warter drop. In V. R. Benzied, editor, *Advances in Turbulence*, pages 470–475. EuroMECH, Kluwer Academic, 1994.

J. J. Thomson and H. F. Newall. On the formation of vortex rings by drops falling into liquids, and some allied phenomena. *Proc. Roy. Soc. London Ser. A*, 39:417–436, 1885.

C. Truesdell. *The Kinematics of Vorticity*. Indiana University, Bloomington, Indiana, 1954.

CHAPTER 8

CONCLUSIONS

8.1 Closing remarks

We close by briefly reviewing the work presented in this thesis and provide an overall context for what was presented.

A careful analysis of interfacial mechanics was carried out in Part I. There were three chapters in this part, Chpt. 2, Chpt. 3 and Chpt. 4, dedicated to understanding the dynamics of vorticity near a free surface.

These chapters also roughly reflect the chronological evolution of my thinking and education on this subject. My work in this field began by working through previous results and making sense of the scattered results in this field and putting them in proper context. These three chapters all benefit from expressing the equations in each chapter using results from differential geometry. Once this task was carried out the incredible depth of results from this field could be used to assist with physical interpretation.

Chpt. 2 generalized and provided detailed physical interpretation of the kinematics at a free surface. Although I derived all the results in this chapter independently, several papers appeared while this thesis was in preparation addressing this subject. The paper most similar to the results in Chpt. 2 was published by Wu (1995) who presented similar results to Eq. (2.15). I was not able to follow his derivation however and the results in that paper were left in a very general form.

To my knowledge Eq. (2.24), describing the presence of streamwise, vorticity is new and is the first time the presence of streamwise vorticity at a free surface has been recognized. This is convincing evidence of the power of differential geometry in the analysis of free surfaces. It was only by expending the small extra effort to write the equations in terms of the curvature tensor

that this result became obvious. Since our paper (Peck and Sigurdson, 1998) was submitted for publication—and before it was accepted for publication— this result has appeared in another paper (Longuet-Higgins, 1998). That paper references the version of our paper which was under review at that time. That paper claims that the effect of surface twist on streamwise vorticity can be educed from the analysis givin therein leading to Eq. (2.31). I do not believe that this is obvious from that analysis without some prior knowledge of the surface twist.

The result deriving from Eq. (2.33) showing that on a steady surface with nonzero Gaussian curvature K vorticity must be present is new. Also recognition of the alignment of the principal value of rate-of-strain with the surface normal is new: Eq. (2.11). This was a particularly satisfying result to discover since, to me at least, it vividly described the interpretation of vorticity attributed to Boussinesq, (Truesdell, 1954). This result also points out an error in the literature given in Longuet-Higgins (1992). Here he stated incorrectly that the motion of fluid elements at a free surface was a rigid body one which was clearly shown to be false. This was important to show and clarify since this incorrect statement has propagated through the literature (Sarpkaya, 1996). By singular coincidence Longuet-Higgins (1998) has now recently recanted his interpretation of solid-body rotation at free surfaces from his earlier paper (Longuet-Higgins, 1992) and recognizes that the interpretation given in Chpt. 2 is correct. The results from Sec. 2.2.4 concerning the geodesic curvature are new and follow immediately once the equations of surface vorticity are expressed in surface coordinates.

Chpt. 3 discusses the vorticity flux. That is, interpreting the diffusion of momentum using the normal gradients of vorticity tangential and normal to a surface. This is a step closer to understanding the vorticity creation mechanism. This is a popular means of estimating the creation of vorticity from free surfaces. Again, I used the sharp interface model and equations of differential geometry to derive the vorticity flux equations. Expressing the equations in a form using results from differential geometry quickly exposed a mistake in the literature. The most important result from this chapter was that the curvature-dependent terms in the vorticity flux equation could be neglected on developable surfaces, that is surfaces where $K = 0$. This analysis pointed out the incorrect result in the literature which was that if vortex lines were straight the vorticity flux due to geometric effects would vanish. This was shown to be false with the analysis given in Sec. 3.4.2 and displayed in Fig. 3.2.

In Chpt. 4 the vorticity transport equation was calculated. Here, recognizing the presence of not only density gradients but also viscosity gradients in the interface exposed new terms in the vorticity transport equation when applied to the thin fluid interface. The extra term arising in the equation of motion due to the viscosity gradient has received very little attention in the literature I reviewed.

Results using the spectral decomposition of D given in Sec. 4.2.1 appears to be new as is the physical interpretation. Also, the assumptions used to obtain Eq. (4.48) in the context of the vorticity equation appear to be unique. This equation satisfied several of the criteria required by the sharp-interface model of the free surface. First, the creation of vorticity should be predicted for surfaces where the surface normal rotates and this is reflected in Eq. (4.48). Also, there should be a production term for interfaces where there is only a viscosity gradient and no density gradient. This too is predicted by Eq. (4.48) where the creation of vorticity is predicted with viscous gradients alone.

Part II contains three chapters reporting experimental results, Chpt. 5, Chpt. 6, Chpt. 7. The first two of these chapters have appeared in the primary literature.

Chpt. 5 was the first chapter to present experimental results. Here vortex rings formed from impacting drops were studied. Scaling arguments were used to compare the data with previously published data with different parameters. This work also points out several problems which needed to be overcome to make reproducible experiments. These issues were addressed in Chpt. 6 which explained how a new apparatus was built based on the apparatus used for the experiments used in Chpt. 5. It is important to note however that the experiments done in Chpt. 5 were not done using the apparatus described in Chpt. 6. This new apparatus was used for the experiments in Chpt. 7 however.

Many new techniques and several revived older techniques were used to construct the final apparatus. This apparatus reflects several hundreds of hours of effort most of it being hand built by myself and the Department of Mechanical Engineering's machine shop staff. The apparatus was sufficiently unique to be published on its own (Peck et al., 1995). I was delighted to include the names of two technicians from the Department of Mechanical Engineering on the paper, Bernard Faulkner and Ian Buttar, who spent countless patient hours working on this apparatus with me.

Finally, Chpt. 7 presented experimental results using this new apparatus.

These results carefully recorded the drop motion above the free surface before impact. This went a long way towards clarifying previous disagreement in the literature over what phase of oscillation produced the most penetrating vortex rings. Also, we presented rarely reported results on the probability of vortex ring formation and found it to be approximately correlated with the penetration depth.

Using results from Part I and experimental observations we predicted the occurrence of early-time countersign vorticity. This is significant since it may explain the source of an early time instability.

Subcritical *We* drops which do not produce vortex rings were studied. Vortex ring formation was inhibited by the flow required by the reversing impact crater. High-*We* drops were found to produce vorticity in a similar way as low *We* drops. The subsequent crater dynamics prevent creation of a vortex ring because of a large bubble which forms from an expanding region of the impact crater.

The first known pictures of the final period of decay are presented. Photographing this process was made possible by the careful construction of the apparatus to ensure no thermal gradients were present. We found excellent agreement with theoretically predicted vortex ring growth and good agreement with the forward motion. These results predict that the vortex centroid should reach a finite depth.

Bibliography

M. S. Longuet-Higgins. Vorticity and curvature at a free surface. *J. Fluid Mech.*, 356:149–155, February 1998.

Michael S. Longuet-Higgins. Capillary rollers and bores. *J. Fluid Mech.*, 240: 659–679, 1992.

Bill Peck and Lorenz Sigurdson. On the kinematics at a free surface. *IMA J. of Appl. Math.*, 60:1–13, 1998.

Bill Peck, Lorenz Sigurdson, Bernard Faulkner, and Ian Buttar. An apparatus to study drop-formed vortex rings. *Measurement Science and Technology*, 6:1538–1545, 1995.

Turgut Sarpkaya. Vorticity, free-surface and surfactants. *Annu. Rev. Fluid Mech.*, 28:83–128, 1996.

C. Truesdell. *The Kinematics of Vorticity*. Indiana University, Bloomington, Indiana, 1954.

Jie-Zhi Wu. A theory of three-dimensional interfacial vorticity. *Phys. Fluids*, 7(10):2375–2395, October 1995.

Appendix A

Jump Conditions at a Fluid Interface

In this appendix the conservation of mass and momentum in a region $\mathscr{R}$ are used to obtain the stress jump conditions on $\mathscr{S}$. The region $\mathscr{R}$, is subdivided into three regions, $\mathscr{R}^-$, $\mathscr{R}^+$ and the material surface $\mathscr{S}$ which forms a common boundary between $\mathscr{R}^+$ and $\mathscr{R}^-$, Fig. A.1.

Conservation of mass

The total mass within $\mathscr{R}$, denoted $\mathcal{M}$, is the sum the three region's masses. $\mathcal{M}$ is the sum of two integrals:

$$\mathcal{M} = \int_{\mathscr{R}-\mathscr{S}} \rho \, dV + \int_{\mathscr{S}} \rho_{\mathscr{S}} \, da, \tag{A.1}$$

where $\rho_{\mathscr{S}}$ is the mass per-unit-area of the surface. To conserve mass in $\mathscr{R}$ the condition

$$\frac{d\mathcal{M}}{dt} = 0 = \frac{d}{dt} \int_{\mathscr{R}-\mathscr{S}} \rho \, dV + \frac{d}{dt} \int_{\mathscr{S}} \rho_{\mathscr{S}} \, da \tag{A.2}$$

must be satisfied.

To evaluate these integrals we will need transport theorems for the bulk fluid regions and the surface itself. The transport theorem for density of the bulk fluid density ρ in a subregion of the $\mathscr{R}$ which contains no singularities
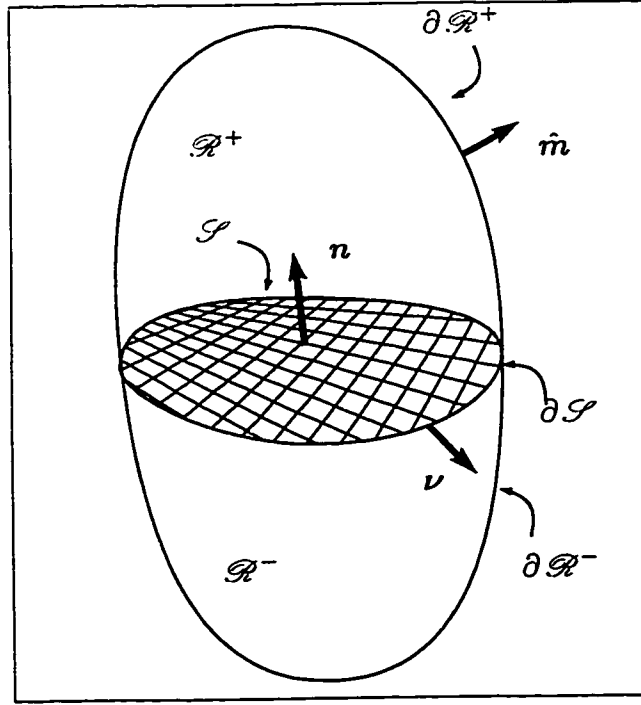
Figure A.1: A region $\mathscr{R}$ of $\mathbb{R}^3$ with an embedded singular surface $\mathscr{S}$.

is

$$\frac{d}{dt} \int_{\mathscr{V}} \rho dV = \int_{\mathscr{V}} \left(\dot{\rho} + \rho \operatorname{div} \boldsymbol{u} \right) dV \qquad \text{(A.3)}$$

$$= \int_{\mathscr{V}} \frac{\partial \rho}{\partial t} dV + \int_{\mathscr{V}} \operatorname{div}(\rho \boldsymbol{u}) dV$$

$$= \int_{\mathscr{V}} \frac{\partial \rho}{\partial t} dV + \int_{\partial \mathscr{V}} \rho \boldsymbol{u} \cdot \boldsymbol{n} da = 0$$

Using the localization theorem we arrive at the mass continuity equation for $\mathscr{R}$,

$$\frac{\partial \rho}{\partial t} + \operatorname{div}(\rho \boldsymbol{u}) = 0. \qquad \text{(A.4)}$$

The derivation of the transport theorem used in Eq. (A.3) is given in several texts on continuum mechanics Chadwick (1976).

We also require the analogous expression of the transport theorem for a surface. Since this form of the transport theorem does not appear as frequently as the three-dimensional version, we will derive it in detail for the surface density. We begin by considering the material derivative of the surface mass. The total mass is given by the integral in Eq. (A.1). The material derivative of this integral becomes:

$$\frac{d}{dt} \int_{\mathscr{S}} \rho_{\mathscr{S}} \, da = \frac{d}{dt} \int_{\mathscr{S}_o} \rho_{\mathscr{S}} \, J dA = \int_{\mathscr{S}_o} \left(\dot{\rho}_{\mathscr{S}} J + \rho_{\mathscr{S}} \dot{J} \right) dA \qquad \text{(A.5)}$$

where,

$$J = \left(\frac{a}{A} \right)^{\frac{1}{2}}. \qquad \text{(A.6)}$$

To proceed we will require an expresssion for the material derivative of J on the surface. Taking the derivative:

$$\dot{J} = \frac{1}{2} \left(\frac{a}{A} \right)^{-\frac{1}{2}} \frac{\dot{a}}{A} = \frac{1}{2} \left(\frac{a}{A} \right)^{\frac{1}{2}} \frac{\dot{a}}{a} \qquad \text{(A.7)}$$

$$= J \left(\frac{\dot{a}}{2a} \right) \qquad \text{(A.8)}$$

Also,

$$\dot{a} = \dot{\overline{\det(a_{\alpha\beta})}} = \frac{\partial [\det(a_{\alpha\beta})]}{\partial a_{\lambda\gamma}} \dot{a}_{\lambda\gamma} = a a^{\alpha\beta} \dot{a}_{\alpha\beta}. \qquad \text{(A.9)}$$

Since we are using convected coordinates,

$$\mathbf{a}_\alpha = \frac{d}{dt} \left(\frac{\partial \mathbf{r}}{\partial \theta^\alpha} \right) = \frac{\partial \dot{\mathbf{r}}}{\partial \theta^\alpha} = \mathbf{v}_{,\alpha}. \qquad \text{(A.10)}$$

Substituting gives

$$\frac{d(a_{\alpha\beta})}{dt} = \frac{d}{dt}(\mathbf{a}_\alpha \cdot \mathbf{a}_\beta) = \mathbf{v}_{,\alpha} \cdot \mathbf{a}_\beta + \mathbf{a}_\alpha \cdot \mathbf{v}_{,\beta} \qquad \text{(A.11)}$$

$$= \left(v^\gamma |_\alpha - v b_\alpha^\gamma \right) \mathbf{a}_\gamma \cdot \mathbf{a}_\beta + \mathbf{a}_\alpha \cdot \left(v^\gamma |_\beta - v b_\beta^\gamma \right) \mathbf{a}_\gamma \qquad \text{(A.12)}$$

$$= v_\beta |_\alpha + v_\alpha |_\beta - 2 v b_{\alpha\beta}. \qquad \text{(A.13)}$$

Now, Eq. (A.9) becomes,

$$\dot{a} = 2aa^{\alpha\beta}(v_\beta|_\alpha + v_\alpha|_\beta - 2vb_{\alpha\beta}) = 2a(v^\alpha|_\alpha + vb^\alpha_\alpha), \qquad (A.14)$$

and

$$\dot{J} = J(v^\alpha|_\alpha + 2vH). \qquad (A.15)$$

Substituting Eq. (A.15) into Eq. (A.5) we obtain the surface transport equation:

$$\frac{d}{dt}\int_{\mathscr{S}} \rho_{\mathscr{S}} da = \int_{\mathscr{S}} \left[\frac{\partial \rho_{\mathscr{S}}}{\partial t} + (\rho_{\mathscr{S}} v^\alpha)|_\alpha - 2\rho_{\mathscr{S}} Hv\right] da \qquad (A.16)$$

Now, the first integral on the right of Eq. (A.1) is seperated into its components lieing in $\mathscr{R}^+$ and regions $\mathscr{R}^-$ and with the aid of Eq. (A.3) and and Eq. (A.16) becomes,

$$\int_{\mathscr{R}^+-\mathscr{S}} \frac{\partial \rho^+}{\partial t} dV + \int_{\mathscr{R}^--\mathscr{S}} \frac{\partial \rho^-}{\partial t} dV \qquad (A.17)$$

$$+ \int_{\partial\mathscr{R}^+-\mathscr{S}} \rho^+ u \cdot \hat{m} da + \int_{\partial\mathscr{R}^--\mathscr{S}} \rho^- u \cdot \hat{m} da$$

$$+ \int_{\mathscr{S}} \rho^+ u \cdot n^+ da + \int_{\mathscr{S}} \rho^- u \cdot n^- da$$

$$+ \int_{\mathscr{S}} \left[\frac{\partial \rho_{\mathscr{S}}}{\partial t} + (\rho_{\mathscr{S}} v^\alpha)|_\alpha - 2\rho_{\mathscr{S}} Hv\right] da = 0.$$

Now, with reference to Fig. A.2 we collapse the two regions $\mathscr{R}^+$ and $\mathscr{R}^-$ on to $\mathscr{S}$. The contributions from the volume integrals will vanish and the surface normal to $\partial\mathscr{R}^+$, $\hat{m}$ will become n^-. Now, after using $n = n^- = -n^+$ Eq. (A.17) becomes,

$$\int_{\mathscr{S}} (\rho^+ u \cdot n - \rho^- u \cdot n + \rho^- u \cdot n - \rho^+ u \cdot n) + \qquad (A.18)$$
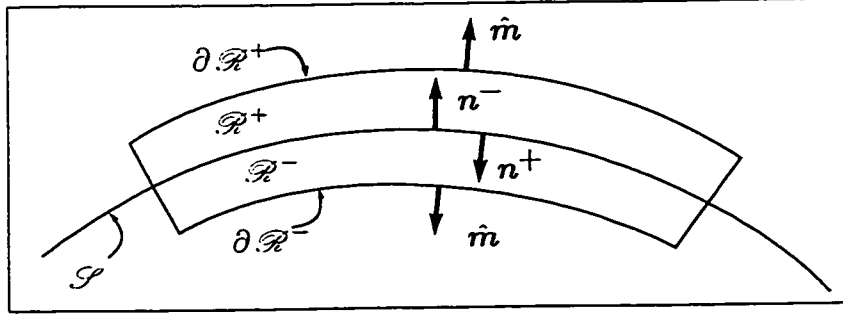
$$\left[\frac{\partial \rho_{\mathscr{S}}}{\partial t} + (\rho_{\mathscr{S}} v^\alpha)|_\alpha - 2\rho_{\mathscr{S}} Hv\right] da = 0$$

Figure A.2: The geometry near $\mathscr{S}$ as $\mathscr{R}$ is collapsed on to $\mathscr{S}$

The first four terms of the integral vanish. Using the localization theorem on the surface Eq. (A.18) we obtain the expression for mass conservation at a point on $\mathscr{S}$:

$$\frac{\partial \rho_{\mathscr{S}}}{\partial t} + (\rho_{\mathscr{S}} v^{\alpha})|_{\alpha} - 2\rho_{\mathscr{S}} Hv = 0 \qquad (A.19)$$

Conservation of momentum

In this section we will derive the jump condition on the surface which balance momentum in $\mathscr{R}$. In general the balance of a thermodynamic variable Ψ i n $\mathscr{R}$ is given by the relation,

$$\frac{d\Psi}{dt} = -\mathcal{W} + \mathcal{P} + \mathcal{R} \qquad (A.20)$$

where $\mathcal{W}$ represent the efflux of Ψ through the boundary $\partial\mathscr{R}$, $\mathcal{P}$, represents the production of Ψ in $\mathscr{R}$ and $\mathcal{R}$ represents the supply of Ψ through external actions such as body forces. In the previous sections we used an intuitive notion of mass conservation where we assumed there was no efflux of mass across the material boundaries or production of mass in the region of interest. Also, we assumed the body forces acting from afar had no effect.

To balance momentum we maust account for the efflux of momentum across $\partial\mathscr{R}$ and body forces. We will however assume there is no production of momentum in $\mathscr{R}$. For the balance of momentum we define

$$\Psi = \mathcal{F} = \int_{\mathscr{R}-\mathscr{S}} \rho u\, dV + \int_{\mathscr{S}} \rho_{\mathscr{S}} v\, da \qquad (A.21)$$

The efflux of momentum $\mathcal{W}$ is given by

$$\mathcal{W} = - \int_{\partial \mathcal{R} - \mathcal{S}} \mathbf{t}_{(n)} da - \int_{\partial \mathcal{S}} \mathbf{t}_{(\mathcal{S})} d\ell \qquad (A.22)$$

Here, $\mathbf{t}_{(n)}$ is the surface traction vector acting on a surface element and $\mathbf{t}_{(\mathcal{S})}$ is the traction per unit length acting on the boundary of $\mathcal{S}$. $\mathbf{t}_{(n)}$ is related to the Cauchy stress through $\mathbf{t}_{(n)} = \boldsymbol{\sigma} \mathbf{n}$. The boundary traction is related to the stress intrinsic to $\mathcal{S}$ through the analogous expression $\mathbf{t}_{(\mathcal{S})} = \mathbf{S} \boldsymbol{\nu}$. The outwardly directed unit vector $\boldsymbol{\nu}$ lies in the tangent plane of $\mathcal{S}$ and is normal to $\partial \mathcal{S}$.

The supply of momentum due to body forces is given by

$$\mathcal{R} = \int_{\mathcal{R} - \mathcal{S}} \rho \mathbf{g} dV + \int_{\mathcal{S}} \rho_{\mathcal{S}} \mathbf{f}_{\mathcal{S}} da \qquad (A.23)$$

where $\mathbf{g}$ and $\mathbf{f}_{\mathcal{S}}$ are the body forces acting on the fluids' volume and surface elements.

Substituting Eq. (A.21), Eq. (A.22) and Eq. (A.22) in Eq. (A.20) we obtain the general expression for the balance of momentum in $\mathcal{R}$

$$\frac{d\mathcal{F}}{dt} = \frac{d}{dt} \int_{\mathcal{R}^+ - \mathcal{S}} \rho^+ \mathbf{u} dV + \frac{d}{dt} \int_{\mathcal{R}^- - \mathcal{S}} \rho^- \mathbf{u} dV + \frac{d}{dt} \int_{\mathcal{S}} \rho_{\mathcal{S}} \mathbf{v} dV \qquad (A.24)$$

$$= \int_{\mathcal{R} - \mathcal{S}} \mathbf{t}_{(n)} da + \int_{\partial \mathcal{S}} \mathbf{t}_{(\mathcal{S})} d\ell + \int_{\mathcal{R} - \mathcal{S}} \rho \mathbf{g} dV + \int_{\mathcal{S}} \rho_{\mathcal{S}} \mathbf{g}_{\mathcal{S}} da \qquad (A.25)$$

Using the transport theorems given in Eq. (A.3) and Eq. (A.16) and substi-

tuting ρu in for ρ and $\rho_{\mathscr{S}} v$ for $\rho_{\mathscr{S}}$ we get,

$$\int\limits_{\mathscr{R}^+-\mathscr{S}} \left[\frac{\partial(\rho^+ u)}{\partial t} - \rho^+ \mathbf{g}\right] dV + \int\limits_{\mathscr{R}^--\mathscr{S}} \left[\frac{\partial(\rho^- u)}{\partial t} - \rho^- \mathbf{g}\right] dV + \qquad \text{(A.26)}$$

$$\int\limits_{\partial\mathscr{R}^+-\mathscr{S}} \left[\rho^+ u(u \cdot \hat{m}) - \mathbf{t}_{(n)}^+\right] da + \int\limits_{\partial\mathscr{R}^--\mathscr{S}} \left[\rho^- u(u \cdot \hat{m}) - \mathbf{t}_{(n)}^-\right] da +$$

$$\int\limits_{\mathscr{S}^+} \left[\rho^+ u(u \cdot n)\right] da + \int\limits_{\mathscr{S}^-} \left[\rho^- u(u \cdot n)\right] da +$$

$$\int\limits_{\mathscr{S}} \left[\frac{\partial(\rho_{\mathscr{S}} v)}{\partial t} + (\rho_{\mathscr{S}} v v^\alpha)|_\alpha - 2\rho_{\mathscr{S}} H v v - \rho_{\mathscr{S}} \mathbf{g}_{\mathscr{S}}\right] da +$$

$$\int\limits_{\partial\mathscr{S}} \mathbf{t}_{(\mathscr{L})} d\ell = 0$$

For regions which do not contain any portion of $\mathscr{S}$ the integrals in $\mathscr{R}^+$ or $\mathscr{R}^-$ become

$$\int\limits_{\mathscr{V}} \frac{\partial(\rho u)}{\partial t} - \rho \mathbf{g} dV + \int\limits_{\partial\mathscr{V}} \left[\rho u(u \cdot \hat{m}) - \mathbf{t}_{(n)}\right] da \qquad \text{(A.27)}$$

$$= \int\limits_{\mathscr{V}} \frac{\partial \rho u}{\partial t} - \rho \mathbf{g} dV + \int\limits_{\partial\mathscr{V}} \left[(\rho u \otimes u) - \sigma\right] \hat{m} da$$

$$= \int\limits_{\mathscr{V}} \left[\frac{\partial \rho u}{\partial t} + \operatorname{div}(\rho u \otimes u) - \operatorname{div} \sigma - \rho \mathbf{g}\right] dV.$$

For a given point in $\mathscr{V}$ the localization theorem gives

$$\frac{\partial \rho u}{\partial t} + \operatorname{div}(\rho u \otimes u) = \operatorname{div} \sigma + \rho \mathbf{g} \qquad \text{(A.28)}$$

Differentiating and using Eq. (A.4) gives

$$\rho \frac{\partial u}{\partial t} + \rho \operatorname{grad} u u + u \underbrace{\frac{\partial \rho}{\partial t} + \operatorname{div}(\rho u)}_{=0} = \operatorname{div} \sigma + \rho \mathbf{g} \qquad \text{(A.29)}$$

so that

$$\rho \dot{u} = \operatorname{div} \boldsymbol{\sigma} + \rho \mathbf{g}. \tag{A.30}$$

This is the spatial form of Cauchy's equation of motion valid in any portion of $\mathscr{R}$ which does not contain any part of $\mathscr{S}$.

Collapsing the integrals on to $\mathscr{S}$, using the same arguments used in Sec. A and invoking Greens theorem for a surface we arrive at the following integral over $\mathscr{S}$:

$$\int_{\mathscr{S}} \frac{\partial(\rho_{\mathscr{S}} v)}{\partial t} + \left(\rho_{\mathscr{S}} v v^{\alpha} \right) \big|_{\alpha} - 2\rho_{\mathscr{S}} H v v - \rho_{\mathscr{S}} \mathbf{f}_{\mathscr{S}} - \operatorname{div} S - \boldsymbol{\sigma}^{+} \boldsymbol{n} - \boldsymbol{\sigma}^{-} \boldsymbol{n} \, da \tag{A.31}$$

Now, using the same sign convention as in Sec. A $-\boldsymbol{\sigma}^{-}\boldsymbol{n} + \boldsymbol{\sigma}^{+}\boldsymbol{n} = -[\![\mathbf{t}_{(n)}]\!]$ where $[\![\quad]\!]$ denotes the jump in the quantity on $\mathscr{S}$. the sign is determined by the difference between the value of a quantity on the side to which the unit normal faces $\mathscr{R}^{+}$ and the value of the quantity in $\mathscr{R}^{-}$. The integral in Eq. (A.31) is rewritten as,

$$\int_{\mathscr{S}} \rho_{\mathscr{S}} \left(\frac{\partial v}{\partial t} + v\big|_{\alpha} v^{\alpha} \right) - \rho_{\mathscr{S}} \mathbf{f}_{\mathscr{S}} - \operatorname{div} S - [\![\mathbf{t}_{(n)}]\!] +$$

$$v \underbrace{\left[\frac{\partial \rho_{\mathscr{S}}}{\partial t} + \left(\rho_{\mathscr{S}} v^{\alpha} \right) \big|_{\alpha} - 2\rho_{\mathscr{S}} H v \right]}_{=0 \text{ by Eq. (A.19)}} da \tag{A.32}$$

which upon using the localization theorem becomes

$$\rho_{\mathscr{S}} \left(\frac{\partial v}{\partial t} + v\big|_{\alpha} v^{\alpha} \right) - \rho_{\mathscr{S}} \mathbf{f}_{\mathscr{S}} - \operatorname{div} S - [\![\mathbf{t}_{(n)}]\!] = 0. \tag{A.33}$$

This is the two-dimensional analogue of Cauchy's equation of motion valid on a surface which may be endowed with Reimann curvature.

The influence of surface tension is obvious when we calculate the divergence S in Eq. (A.33). Using identity Eq. (E.19) we expand the expression into,

$$\operatorname{div} S = \mathbf{a}^{\alpha} \otimes \mathbf{a}_{\alpha} \operatorname{grad} \gamma + \gamma \operatorname{div}(\mathbf{a}^{\alpha} \otimes \mathbf{a}_{\alpha}), \tag{A.34}$$

The first term on the right of Eq. (A.34) is transformed into the surface gradient since $\mathbf{a}^\alpha \otimes \mathbf{a}_\alpha \operatorname{grad} \gamma = (\mathbf{a}_\alpha \cdot \operatorname{grad} \gamma)\mathbf{a}^\alpha = \operatorname{grad}_{\mathscr{S}} \gamma$. With the identity given in Eq. (E.20) Eq. (A.34) becomes,

$$\operatorname{div} \mathcal{S} = \operatorname{grad}_{\mathscr{S}} \gamma + \gamma(\operatorname{grad} \mathbf{a}^\alpha) + \gamma \mathbf{a}^\alpha(\operatorname{div} \mathbf{a}_\alpha) \tag{A.35}$$

$$= \operatorname{grad}_{\mathscr{S}} \gamma + \gamma(\mathbf{a}^\alpha{}_{,\beta} \otimes \mathbf{a}_\beta)\mathbf{a}^\alpha + \gamma \mathbf{a}^\alpha[\operatorname{tr}(\operatorname{grad} \mathbf{a}_\alpha)].$$

$$= \operatorname{grad}_{\mathscr{S}} \gamma + \gamma \left[(-\Gamma^\alpha_{\gamma\beta}\mathbf{a}^\alpha + b^\alpha_\beta n) \otimes \mathbf{a}^\beta \right] \mathbf{a}_\alpha +$$

$$\left[\operatorname{tr}(\Gamma^\gamma_{\alpha\beta}\mathbf{a}_\gamma \otimes \mathbf{a}^\beta + b_{\alpha\beta}n \otimes \mathbf{a}^\beta) \right] \mathbf{a}^\alpha$$

$$= \operatorname{grad}_{\mathscr{S}} \gamma - \gamma \left(\Gamma^\alpha_{\gamma\alpha}\mathbf{a}^\gamma - \Gamma^\beta_{\gamma\beta}\mathbf{a}^\gamma - b^\alpha_\alpha n \right)$$

$$= \operatorname{grad}_{\mathscr{S}} \gamma + \gamma b^\alpha_\alpha n \tag{A.36}$$

Hence, we arrive at the final result:

$$\operatorname{div} \mathcal{S} = \operatorname{grad}_{\mathscr{S}} \gamma + 2\gamma H n. \tag{A.37}$$

This is the general form of the classic result relating the surface tension coefficient to the curvature of the surface. In this general form we see that the mean curvature affects the normal component of the stress and causes a force normal to the surface itself. Another force tangential to the surface is created by the presence of surface tension gradients.

Bibliography

P. Chadwick. *Continuum Mechanics.* John Wiley and Sons, New York, 1976.

APPENDIX B

MATERIAL DERIVATIVE OF THE SURFACE NORMAL

The material derivative of a surface's unit normal vector can be calculated with the aid of Nanson's relation ((Chadwick, 1976), p.61). This equation describes the deformation of a surface element from a reference to deformed configuration,

$$nda = J\mathbf{F}^{-T}\mathbf{N}dA. \tag{B.1}$$

$\mathbf{F}$ is the deformation tensor given by

$$\mathbf{F} = \frac{\partial x_i}{\partial X_j}\mathbf{e}_i \otimes \mathbf{E}_j, \tag{B.2}$$

where x_i are coordinates in the deformed configuration with Cartesian basis vectors $\mathbf{e}_i$. The coordinates X_j and basis vectors $\mathbf{E}_j$ are fixed in the reference configuration. The Jacobian J is defined by $J = \det \mathbf{F}$. Also, $\mathbf{N}$ is a unit vector normal to a reference surface element dA. The corresponding quantities in the deformed configuration are denoted by n and da.

The material derivative of $\mathbf{F}$ is

$$\dot{\mathbf{F}} = \frac{d}{dt}\left(\frac{\partial x_i}{\partial X_j}\right)\mathbf{e}_i \otimes \mathbf{E}_j = \frac{\partial u_i}{\partial X_j}\mathbf{e}_i \otimes \mathbf{E}_j = \frac{\partial u_i}{\partial x_k}\frac{\partial x_l}{\partial X_j}(\mathbf{e}_i \otimes \mathbf{e}_k)(\mathbf{e}_l \otimes \mathbf{E}_j) = \mathbf{LF} \tag{B.3}$$

so that

$$\mathbf{L} = \dot{\mathbf{F}}\mathbf{F}^{-1}. \tag{B.4}$$

Now, since $\mathbf{FF}^{-1} = \mathbf{I}$,

$$\mathbf{L} = \dot{\mathbf{F}}\mathbf{F}^{-1} = -\mathbf{F}\dot{\mathbf{F}}^{-1}. \tag{B.5}$$

Differentiating Eq. (B.1) materially gives

$$\dot{n}da + nd\dot{a} = \dot{J}F^{-T}NdA + J\dot{F}^{-T}NdA.$$ (B.6)

The material derivative of the Jacobian is

$$\dot{J} = J\,(\text{tr}\mathbf{L}).$$ (B.7)

With the aid of Eq. (B.5) the derivative of $\mathbf{F}^{-T}$ is rewritten in the form,

$$\dot{\mathbf{F}}^{-T} = (\dot{\mathbf{F}}^{-1})^{T} = -(\mathbf{F}^{-1}\mathbf{L})^{T} = -\mathbf{L}^{T}\mathbf{F}^{-T}.$$ (B.8)

Substituting Eq. (B.7) and Eq. (B.8) into Eq. (B.6) gives,

$$\dot{n}da + nd\dot{a} = \left(\text{tr}\mathbf{L} - \mathbf{L}^{T}n\right)J\mathbf{F}^{-T}NdA.$$ (B.9)

The dot product of n with Eq. (B.9) yields an expression for the rate of surface dilation;

$$\frac{d\dot{a}}{da} = \text{tr}\mathbf{L} - n \cdot \left(\mathbf{L}^{T}n\right) = \text{tr}\mathbf{L} - n \cdot \left(\mathbf{L}n\right),$$ (B.10)

where we have used $n \cdot n = 1$ and $\dot{n} \cdot n = 0$. Substituting Eq. (B.10) into Eq. (B.9) gives the material derivative of the surface normal,

$$\dot{n} = n \cdot \left(\mathbf{L}n\right) - \mathbf{L}^{T}n.$$ (B.11)

We can also calculate the material derivative of the surface normal vector n in terms of surface coordinates. This derivation is based on that which appears in Naghdi (1972).

The dot product of the surface normal and a vector lying in the tangent plane $a_\alpha \cdot n = 0$ is differentiated materially:

$$\frac{d}{dt}(a_\alpha \cdot n) = \dot{a}_\alpha \cdot n + a_\alpha \cdot \dot{n} = 0$$ (B.12)

so that

$$\dot{a}_\alpha \cdot n = -a_\alpha \cdot \dot{n}.$$ (B.13)

Since $\dot{a}_\alpha = v_{,\alpha}$ Eq. (B.13) can be multiplied by a^α and rewritten as

$$(a_\alpha \cdot \dot{n})\,a^\alpha = \dot{n} = (n \cdot v_{,\alpha})a^\alpha.$$ (B.14)

The derivative $v_{,\alpha} = (v^\alpha \mathbf{a}_\alpha)_{,\beta} + (v\mathbf{n})_{,\alpha}$ is calculated with the aid of Weingarten's equation,

$$n_{,\alpha} = b_\alpha^\gamma \mathbf{a}_\gamma, \qquad (B.15)$$

Substituting Eq. (B.15) and Gauss's equation,

$$\mathbf{a}_{\alpha,\beta} = \Gamma_{\alpha\beta}^\gamma + b_{\alpha\beta} \mathbf{n} \qquad (B.16)$$

$v_{,\alpha}$ becomes

$$v_{,\alpha} = (v^\lambda|_\alpha + b_\lambda^\alpha v)\mathbf{a}_\lambda + (v_\alpha + b_\alpha^\lambda v_\lambda)\mathbf{n} \qquad (B.17)$$

so that

$$\begin{aligned}
\dot{n} &= - \left[v_{,\alpha} - (b_\lambda^\alpha v^\lambda)\right] \mathbf{a}_\alpha \\
&= -v_\alpha \mathbf{a}_\alpha - b_\lambda^\alpha v_\gamma \left(\mathbf{a}^\lambda \cdot \mathbf{a}^\gamma\right) \mathbf{a}_\alpha \\
&= -v_{,\alpha} \mathbf{a}^\alpha - \left(b_\lambda^\alpha \mathbf{a}_\alpha \otimes \mathbf{a}^\lambda\right) v_\gamma \mathbf{a}^\gamma \\
&= -\text{grad}_{\mathscr{S}} v - \mathbf{b} v
\end{aligned} \qquad (B.18)$$

Bibliography

P. Chadwick. *Continuum Mechanics.* John Wiley and Sons, New York, 1976.

P. M. Naghdi. *S. Flugge's Handbuch der Physik*, volume VIa/2, chapter The theory of plates and shells, pages 425–640. Springer, Berlin, 1972.

Appendix C

Material description of vorticity

This appendix shows how the rate of change of an arbitrary deformation relates to the vorticity using a material description.

In this derivation we use $\mathscr{B}_r$ to represent the material body in its reference state and $\mathscr{B}_t$ for the transformed material body. Coordinates in the deformed configuration are given by x_i directed along the basis vectors e_i. Reference frame coordinates are X_i with basis vectors E_i. The deformation gradient tensor F is given by

$$F = \text{Grad}\, F = \frac{\partial x_i}{\partial X_j} e_i \otimes E_j. \tag{C.1}$$

Here, Grad indicates spatial derivatives forming the gradient taken with repect to the reference configuration.

The deformation gradient F is the fundamental kinematic quantity comparing sizes and shapes of material bodies in their reference and transformed states. F only gives information about the relative shapes of material elements, it does not provide us with any indication of the rate at which the element deforms. Knowledge of the deformation rate gives essential information for determining the viscous forces in a real fluids. More importantly we will also be able to deduce the vorticity by calcualting the rate which the principal axes of strain rotate.

To calculate the rate we take the time derivative of $\mathbf{F}$

$$\frac{d\mathbf{F}}{dt} = \dot{\mathbf{F}} = \frac{d}{dt}\left(\frac{\partial x_i}{\partial X_i}\right)\mathbf{e}_i \otimes \mathbf{E}_j \qquad (C.2)$$

$$= \frac{\partial}{\partial X_j}\left(\frac{dx_i}{dt}\right)\mathbf{e}_i \otimes \mathbf{E}_j \qquad (C.3)$$

$$= \frac{\partial}{\partial X_j}(u_i)\mathbf{e}_i \otimes \mathbf{E}_j \qquad (C.4)$$

$$= \frac{\partial u_i}{\partial x_l}\frac{\partial x_k}{\partial X_j}\delta_{kl}\mathbf{e}_i \otimes \mathbf{E}_j \qquad (C.5)$$

$$= \frac{\partial u_i}{\partial x_l}\mathbf{e}_i \otimes \mathbf{e}_l\frac{\partial x_k}{\partial X_j}\mathbf{e}_k \otimes \mathbf{E}_j \qquad (C.6)$$

$$= \operatorname{grad}\mathbf{u}\,\mathbf{F} = \mathbf{L}\mathbf{F} \qquad (C.7)$$

where $\mathbf{L} = \operatorname{grad}\mathbf{u}$ is the spatial gradient of velocity. Multiplying both sides of the last line of Eq. (C.2) by $\mathbf{F}^{-1}$ with the aid of Eq. (E.9) we have the required expression for the velocity gradient in terms of the time derivative of $\mathbf{F}$ and $\mathbf{F}$ itself in the form of its inverse.

$$\operatorname{grad}\mathbf{u} = \dot{\mathbf{F}}\mathbf{F}^{-1} \qquad (C.8)$$

The velocity gradient is the gradient of a vector, and as such, is a tensor with a unique *additive* decomposition

$$\mathbf{L} = \mathbf{D} + \mathbf{W} \qquad (C.9)$$

where

$$\mathbf{D} = \frac{1}{2}\mathbf{L} + \frac{1}{2}\mathbf{L}^{\mathrm{T}}$$

$$\mathbf{W} = \frac{1}{2}\mathbf{L} - \frac{1}{2}\mathbf{L}^{\mathrm{T}}.$$

For now we will refer to $\mathbf{D}$ and $\mathbf{W}$ as the symmetric and anti-symmetric or skew-symmetric components of $\mathbf{L}$.

To gain a deeper insight into the physical relevance of these tensors we write them in terms of the deformation gradient tensor Eq. (C.8)

$$\mathbf{D} = \frac{1}{2}\left[\dot{\mathbf{F}}\mathbf{F}^{-1} + (\dot{\mathbf{F}}\mathbf{F}^{-1})^{\mathrm{T}}\right] \qquad (C.10)$$

$$\mathbf{W} = \frac{1}{2}\left[\dot{\mathbf{F}}\mathbf{F}^{-1} - (\dot{\mathbf{F}}\mathbf{F}^{-1})^{\mathrm{T}}\right].$$

Now we write the deformation gradient in terms of its *multiplicative* decomposition,

$$F = RU \text{ or } F = VR, \tag{C.11}$$

where U and V are symmetric tensors representing a stretch along three mutually orthogonal (principal) axes. R is a rotation tensor so that if it acts on a line element dx, Fdx represents a rotation of dx. Thus, from Eq. (C.11) the deformation can be represented as either a rotation of three mutually orthogonal axes of deformation followed by a triaxial deformation or the deformation followed by a rotation.

Now we will substitute Eq. (C.11) into Eq. (C.8) and then use this result to evaluate D and, more importantly, W in Eq. (C.10). First,

$$\begin{aligned} L &= (\dot{RU})(RU)^{-1} \\ &= (\dot{R}U + R\dot{U})(U^{-1}R^{-1}) \\ &= \dot{R}UU^{-1}R^{-1} + R\dot{U}U^{-1}R^{-1} \\ &= \dot{R}R^{-1} + R\dot{U}U^{-1}R^{-1} \end{aligned} \tag{C.12}$$

Substituting Eq. (C.12) in Eq. (C.10) we find,

$$D = \frac{1}{2}\left[\dot{R}R^{-1} + (\dot{R}R^{-1})^T + R\dot{U}U^{-1} + (R\dot{U}U^{-1})^T\right]. \tag{C.13}$$

To simplify Eq. (C.13) we first note $R^{-1} = R^T$ since it is a rotation. Now $RR^{-1} = RR^T = I$ so that $\dot{R}R^T + (\dot{R}R^T)^T = 0$ and it follows $\dot{R}R^T$ is skew symmetric. With this result Eq. (C.13) reduces to,

$$D = \frac{1}{2}\left[R(\dot{U}U^{-1} + U^{-1}\dot{U})R^T\right]. \tag{C.14}$$

Where we have used the symmetric properties of U. A similar calculation for W gives,

$$W = \frac{1}{2}R\left(\dot{U}U^{-1} - U^{-1}\dot{U}\right)R^T + \dot{R}R^T, \tag{C.15}$$

where we see the skew symmetric tensor remains.

Now we suppose that the deformed configuration is passing through the reference state. At this point $F = I$ so that $U = R = I$ and D and W take on the simple forms,
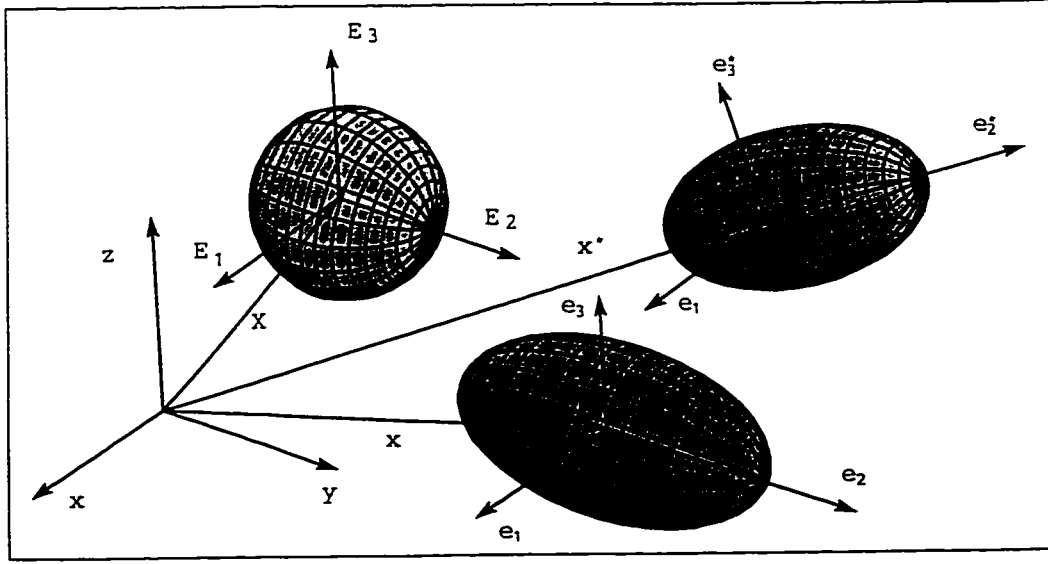
$$D = \dot{U} \text{ and } W = \dot{R}. \tag{C.16}$$

Figure C.1: An arbitrary deformation of a fluid element. Deformation of the element's centroid to x ($\mathscr{B}_t$) from X ($\mathscr{B}_r$) represents an irrotational motion. Deformation of the element from X to x* represents a rotational motion.

Since D is symmetric it also possesses three principal values λ_i directed along three mutually orthogonal axes r_i. As we pass through the reference state, we see that these principal values will coincide with the rate of the stretch along the principal axes.

We choose a material line element directed along a principal direction r_i to examine the effect of W. Calculating the material derivative gives

$$\dot{r}_i = Lr_i - \{r_i \cdot (Lr_i)\}r_i \tag{C.17}$$
$$= (D + W)r_i - \{r_i \cdot (D + W)r_i\}r_i$$
$$= \underbrace{\lambda_i r_i - r_i \cdot (\lambda_i r_i)r_i}_{=0} + Wr_i$$

$$= Wr_i = \Omega \times r_i = \frac{\omega}{2} \times r_i \tag{C.18}$$

Now

$$2\Omega = \omega = \operatorname{curl} v \tag{C.19}$$

In view of this result we see vorticity represents twice the rate of rotation of the principal axes of rate-of-strain. If we choose the deformed configuration

as it instantaneously passes through the reference configuration we see that for that instant the vorticity represents twice the rate of rotation of the principal axes of strain.

With this result, physical interpretation of the velocity gradient becomes clear. The rate-of-deformation or rate-of-strain tensor D represents the rate at which an element is stretching along three principal axes. The spin tensor W represents the rate-of-rotation of these axes.

An arbitrary motion in a continuum is composed of a translation, a stretch along three mutually-orthogonal axes and an instantaneous rotation of these axes. This is the Cauchy-Stokes decomposition of a motion and applies equally well to all media whether it is fluid or not.

APPENDIX D

THE THREE-DIMENSIONAL TRANSITION OF THE VORTICITY CREATED BY AN IMPACTING WATER DROP

ABSTRACT

A falling water drop impacting the free surface of a pool of water creates approximately circularly symmetric vorticity. This vorticity rolls up into a primary vortex ring and undergoes a transition to a three-dimensional structure. Under certain conditions, this characteristic large-scale structure is strikingly similar to an above-ground atomic blast. The range of parameters discussed here is of interest because the resulting vorticity is at a Reynolds number very near the transition Reynolds number, therefore the flow goes from laminar to turbulent to laminar again, allowing careful study of the transition process. The nature of the insta-. bility is discussed with particular regard to categorization. It is suggested that it is not the Widnall instability that is initially at work although it may play a role at later times.

D.1 Background

Photographic observations and ring convection velocity measurements have been reported for the transition to three-dimensionality of the vorticity created by a dyed water drop impacting a pool of water (Peck and Sigurdson, 1994). It was studied for a Weber number of 22–25 and a Froude number of 25–28. As the drop impacts the pool its impulse initially produces circularly symmetric vorticity which rolls up into a primary vortex ring. As this happens, some vortex filaments undergo an azimuthal instability (in what will be referred to as the transition region) resulting in stream-wise vortices which extend from the primary vortex ring to another ring of vorticity that appears and remains at the free-surface. The azimuthal instability continues to grow as the primary ring convects downward until the filaments escape the trapped orbits of the primary vortex ring and are 'shed'. (This has recently been shown to occur numerically by Chorin (1993) in a similar flow.) This results in three to five loops or 'petals' left behind the primary ring. Although photographs indicate that the initial instability at earlier times grows in a non-symmetric way, the petals which emerge tend to do so in an azimuthally symmetric fashion. The ring velocity does not vary significantly during this process (Peck and Sigurdson, 1995). After the petals are shed a relaminarized circular primary vortex ring continues to convect downward (relaminarized region).

D.2 Nature of the instability

D.2.1 Possible instabilities

There are two previously recognized instabilities of vortex rings which may be responsible for the transition observed in the present case. The first is the Widnall instability (Widnall et al., 1974; Widnall, 1975) (also sometimes called the Krutzsch instability) which consists of a waviness of the entire core which grows due to the imposed straining field from the circular geometry of the rest of the ring. The second is Rayleigh's centrifugal instability (Maxworthy, 1972) or a Taylor-Görtler type instability (Glezer and Coles, 1990) which are a more localized instability of the core itself which occur without the presence of an external straining field. It could therefore occur on a straight, infinitely long vortex as well as on a curved vortex. It requires that the absolute value of the circulation, Γ, decrease with radial distance at

some point in the flow.

Another possibility for the present case is that it involves an instability of the vortex sheet which rolls up to form the vortex ring itself. There is certainly evidence of instability as early as 7.5 ms when the vortex ring is still very much in the formation stage. This may couple with the Taylor-Görtler instability. It may be a result of a Bernal-Roshko type of instability (Bernal, 1981) occurring in the vortex sheet, amplified in a straining field between the primary vortex ring and the local ring that remains at the free surface.

D.2.2   Previous Discussion and current results

Dziedzic (1994) suggested a new classification scheme for vortex rings:

(a) laminar

(b) laminar, but with azimuthal waves on the core

(c) turbulence producing—rough surface, laminar core. turbulent wake

(d) turbulent—turbulent core, turbulent wake.

He concluded that a rough estimate for the transition between (b) and (c) is $Re = 1000$, and $Re = 2000$ for (d), where $Re =$ Reynolds number based vortex ring velocity and diameter. Maxworthy (1972) described three regimes:

(a) $Re < 600$, laminar, (b) $Re > 600$, waviness, (c) $Re > 1000$, turbulence.

In the present case, the Re is initially 320–390 for the relaminarized vortex rings, well within the laminar regime. Earlier, in the transition region (non-dimensional times less than 3.6 in Fig. D.1), the Re is higher, perhaps as high 600 as measured in the lab reference frame. (Due to the upward flow suggested by the free surface motion, the effective Re may be higher.) This could be high enough to produce some Widnall waviness, but the waviness would have very little time to grow before the Re dropped into the stable regime again. Also, the Widnall instability is based upon a waviness of the entire core (the most unstable mode is estimated to be three or four waves), whereas the instability observed in the present case appears to be initially a very high wave number instability (28 waves) which grows on an otherwise
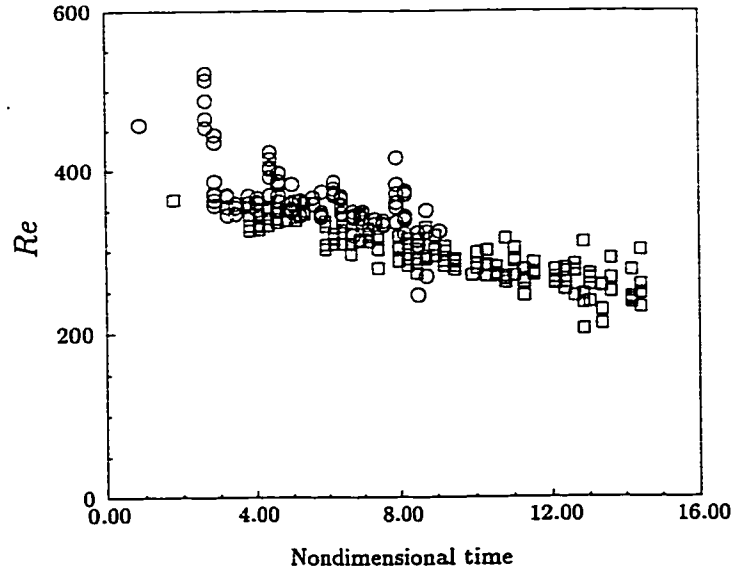
Figure D.1: Reynolds number versus non-dimensional time (Using data from Peck and Sigurdson (1995))

uniformly circular core. For these reasons it is concluded that the present instability is probably not the Widnall instability.

A much more likely candidate is a Taylor-Görtler type instability as suggested by Glezer and Coles (1990) for their turbulent vortex rings. This falls into the category of Rayleigh's centrifugal instabilities which was suggested by Maxworthy (1972). This may be the instability which is responsible for making Dziedzic's "turbulence producing" rings dimensional time have an apparent "rough surface", although the core remains laminar, at $Re = 1000$ (similarly for Maxworthy's regime c). In the present case the velocities involved before vortex ring formation is complete are also much higher than the resulting vortex ring velocity (perhaps three or four times as high) creating a Re comparable to that of the $Re = 1000$ vortex rings. (A Taylor-Görtler instability would scale not on the velocity of the ring and diameter directly, but rather the properties of the core alone.)

Maxworthy (1972) suggested that vorticity of opposite sign to the primary vortex ring is generated due to the induced flow of the vortex ring interact-

ing with the vortex generator. This can be transported to the outside of the ring creating a situation which is unstable by Rayleigh's criterion. As a Taylor-Görtler type instability is a centrifugal instability, this conjecture is not inconsistent with Glezer and Coles' comments. The present case does have vorticity of opposite sign present, first apparent within the reversing impact crater at 10 ms, and forming the base rings. It has already been suggested (Peck and Sigurdson, 1994) that some of the primary ring vorticity gets trapped with the base rings. Simultaneously, or conversely, some of the base ring may become trapped if the primary ring, leading to the situation Maxworthy envisaged. After the instability has grown and escaped the previously trapped orbits of the vortex ring, the Rayleigh criterion may no longer be satisfied and the appropriate Re may have dropped below critical, therefore the ring would remain laminar.

Another possibility is that the formation of the vortex ring (which involves an unknown unusual initial distribution of vorticity, a vortex sheet roll-up, and a slight diameter contraction) creates a situation which intensifies or couples with the Taylor-Görtier instability or offers the possibility for instability of the vortex sheet itself. This possibility would suggest an instability unique to this particular geometry. After the 'petals' have been shed the conditions leading to the instability would be absent, therefore no further instability would occur unless the resulting vortex ring Re was above critical for the Widnall instability.

Although the initial instability may not be the Widnall instability, the observed wave number drops into the range one might expect for this flow. This could indicate that a combination of the two instabilities is at work, the Taylor-Görtler first and then the Widnall.

D.2.3 Vortex dynamics geometry of the ring instability

From a vortex dynamics point of view, one possibility for the source of the transverse vorticity is tilting of the vortex lines present in the primary ring. A sequence of geometries for a representative vortex line is shown in

This figure indicates how an initial perturbation in a vortex line could grow and create the transverse rings which would then convect away from the core under their self-induction (Peck and Sigurdson, 1994, Fig. 6). This is similar to the instability directly Fig. 2 Representative vortex observed experimentally by Smith and Wei (1994). in colliding off-axis vortex rings, who draw a distinction between this and the Widnall instability. Chorin
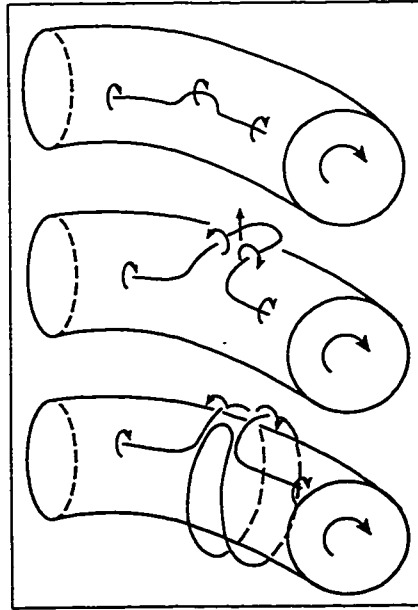
Figure D.2: Representative vortex line indicating nature of the instability

(1993) has shown numerically that small perturbations grow into loops which are shed behind a vortex ring. Lim (1989) discussed the presence of a similar geometry of bi-helical vortex lines in an experimental study of a vortex ring interacting with an inclined wall. The cause in that case is a variation in core size which causes the vortex line segments closer to the wall to wind around the vortex ring axis at a rate faster than those further away. This is not thought to be as strong an effect in the present case, but may be a contributing factor.

The instability may also be similar to that observed by Liepmann and Gharib (1992) in the early development of round jets. They concluded (Liepmann and Gharib, 1992, Pg. 65) that it is not a Widnall instability but do not discuss it further other than to note that the instabilities first appeared in the braid and not the primary ring. (The braid is the region between two successive rings.) This type of instability might be referred to as a Bernal-Roshko instability (Bernal, 1981).

D.2.4 Growth of the instability

The transverse axial pairs may undergo a merging process to reduce the number of waves from 21 to 3, 4 or 5. A similar process has been reported by Taneda (1977) for the growth of the boundary layer on an impulsively rotated cylinder which shows very similar structures. It can be qualitatively understood by considering that two suitably spaced vortex dipoles side by side will initially be attracted to one another, simply by considering their induced velocities from the Biot-Savart law.

D.3 Conclusions

The nature of the initial instability leading to the transition in the present case is most likely not the Widnall instability, but rather a Taylor-Görtler or Bernal-Roshko type of instability. The Widnall instability may play a role at later times.

Bibliography

Luis Bernal. *The coherent structure of turbulent mixing layers.* Phd, Caltech, 1981.

A.J. Chorin. Hairpin removal in vortex interactions ii. *J. Comp. Phys.*, 107: 1–9, 1993.

M. Dziedzic. *An experimental study of viscous vortex rings.* Phd, University of Toronto, 1994.

A. Glezer and D. Coles. An experimental study of a turbulent vortex ring. *J. Fluid Mech.*, 211:243–283, 1990.

Dorian Liepmann and Morteza Gharib. The role of streamwise vorticity in the near field entrainment of round jets. *J. Fluid Mech.*, 245:643–668, 1992.

T. T. Lim. An experimental study of a vortex ring interacting with an inclined wall. *Exp. in Fluids*, 7:453–463, 1989.

T. Maxworthy. The structure and stability of vortex rings. *J. Fluid Mech.*, 51(part 1):15–32, 1972.

Bill Peck and Lorenz Sigurdson. The three-dimensional vortex structure of an impacting water drop. *Phys. Fluids*, 6(2):564–576, February 1994.

Bill Peck and Lorenz Sigurdson. The vortex ring velocity resulting from an impacting water drop. *Exp. in Fluids*, 18:351–357, 1995.

Lorenz Sigurdson and Bill Peck. Three-dimensional transition of the vorticity created by an impacting warter drop. In V. R. Benzied, editor, *Advances in Turbulence*, pages 470–475. EuroMECH, Kluwer Academic, 1994.

G. B. Smith and T. Wei. Small-scale structure in colliding off-axis vortex rings. *J. Fluid Mech.*, 259:281–290, 1994.

S. Taneda. Visual study of unsteady seperated flows around bodies. *Prog. Aerosp. Sci.*, 17:287–348, 1977.

Sheila Widnall. The dynamics of vortex filaments. *Annu. Rev. Fluid Mech.*, 7:141–165, 1975.

Sheila Widnall, Donald B. Bliss, and Chon-Yin Tsai. The instability of short waves on a vortex ring. *J. Fluid Mech.*, 66:35–47, 1974.

Appendix E

Useful Formulae

E.1 Notational style

A comparison of two notations with a vector $\mathbf{a}$ and tensor $\mathbf{A}$.

$$\mathbf{A}\mathbf{a} = \mathbf{a} \cdot \mathbf{A} \quad \text{and} \quad \mathbf{A}^{\mathrm{T}}\mathbf{a} = \mathbf{A} \cdot \mathbf{a} \tag{E.1}$$

The Navier-Stokes equations can is written as

$$\frac{\partial \mathbf{u}}{\partial t} + \mathbf{L}\mathbf{u} = -\frac{\operatorname{grad} p}{\rho} + \nu \operatorname{div} \operatorname{grad} \mathbf{u}. \tag{E.2}$$

using the notation in this text. The notation $(\mathbf{u} \cdot \nabla)\mathbf{u}$ can often be found in the fluid mechanics literature to represent $\mathbf{L}\mathbf{u}$. Also ∇^2 or $\nabla \cdot \nabla\mathbf{u}$ is often used to represent $\operatorname{div} \operatorname{grad} \mathbf{u}$

E.2 Vector identities

For the arbitrary scalar ϕ, vectors (or first order tensors) $\mathbf{a}, \mathbf{b}, \mathbf{c}, \mathbf{d}$ and tensor $\mathbf{A}$ the following identities apply.

$$\phi(\mathbf{a} \times \mathbf{b}) = \mathbf{a} \times (\phi\mathbf{b}) \tag{E.3}$$

$$\mathbf{a} \times (\mathbf{b} \times \mathbf{c}) = (\mathbf{a} \times \mathbf{b}) + (\mathbf{a} \times \mathbf{c}) \tag{E.4}$$

$$\mathbf{a} \times \mathbf{b} = -\mathbf{b} \times \mathbf{a} \tag{E.5}$$

186

$$a \times (b \times c) = b \cdot (a \cdot c) - c \cdot (a \cdot b) \qquad (E.6)$$

$$(a \times b) \cdot (c \times d) = (a \cdot c)(b \cdot d) - (a \cdot d)(b \cdot c) \qquad (E.7)$$

$$(a \times b) \times (c \times d) = b[a \cdot (c \times d)] - a[b \cdot (c \times d)] \qquad (E.8)$$

$$AA^{-1} = I \qquad (E.9)$$

E.3 Gradient identities

The gradient operation increases the rank of a tensor by one. For example the gradient of a zeroeth order tensor (a scalar) is a vector; the gradient of a first order tensor(a vector) is a tensor.

$$\text{grad}(\phi a) = (\text{grad}\,\phi) \otimes a + \phi\,\text{grad}\,a \qquad (E.10)$$

$$\text{grad}(a \cdot b) = (\text{grad}\,a)b + (\text{grad}\,b)a + a \times \text{curl}\,b + b \times \text{curl}\,a \qquad (E.11)$$

E.4 Curl identities

$$\text{curl}(\text{grad}\,\phi) = 0 \qquad (E.12)$$

$$\text{curl}(\phi a) = \text{grad}\,\phi \times a + \phi\,\text{curl}\,a \qquad (E.13)$$

$$\text{curl}(a \times b) = (\text{grad}\,a)b - (\text{grad}\,b)a + a\,\text{div}\,b - b\,\text{div}\,a \qquad (E.14)$$

$$\text{curl}(\text{curl}\,a) = \text{grad}(\text{div}\,a) - \text{div}(\text{grad}\,a) \qquad (E.15)$$

E.5   Divergence identities

The divergence operator decreases the rank of a tensor by one. The divergence of a second order tensor is a vector (a first order tensor). The divergence of a vector is a scalar (a zeroeth order tensor).

$$\text{div}(\text{curl}\, a) = 0 \tag{E.16}$$

$$\text{div}(a \times b) = b \cdot \text{curl}\, a - a \cdot \text{curl}\, b \tag{E.17}$$

$$\text{div}(\text{grad}\, a) = \text{grad}(\text{div}\, a) - \text{curl}(\text{curl}\, a) \tag{E.18}$$

$$\text{div}(\phi A) = A\, \text{grad}\, \phi + \phi\, \text{div}\, A \tag{E.19}$$

$$\text{div}(a \otimes b) = (\text{grad}\, a)b + a\, \text{div}\, b \tag{E.20}$$

E.6   Transport Formulae

E.6.1   Scalar Transport formulae

$$\frac{d}{dt}\int_{\mathscr{C}_t} \phi\, da = \int_{\mathscr{C}_t} (\dot{\phi}dx + \phi L dx) \tag{E.21}$$

$$\frac{d}{dt}\int_{\mathscr{S}_t} \phi n\, da = \int_{\mathscr{S}_t} \left[(\dot{\phi} + \phi\, \text{tr}\, L)n - \phi L^T n\right] da \tag{E.22}$$

$$\frac{d}{dt}\int_{\mathscr{R}_t} \phi\, dv = \int_{\mathscr{R}_t} (\dot{\phi} + \phi\, \text{tr}\, L) dv \tag{E.23}$$

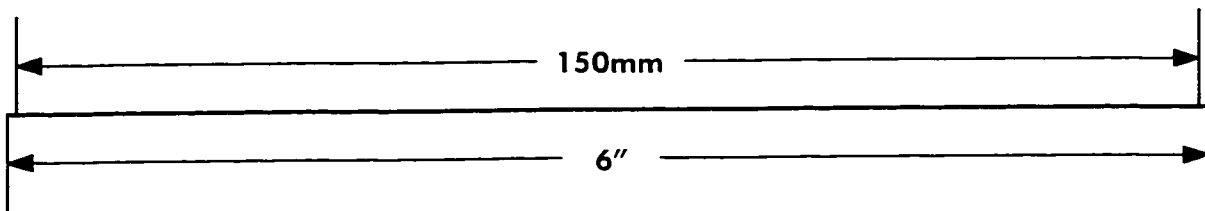### E.6.2   Vector Transport formulae

$$\frac{d}{dt}\int_{\mathscr{C}_t} a \cdot dx = \int_{\mathscr{C}_t} (\dot{a} + L^T a) \cdot dx \tag{E.24}$$

$$\frac{d}{dt}\int_{\mathscr{S}_t} a \cdot n da = \int_{\mathscr{S}_t} (\dot{a} + a\, \text{tr}\, L - La) \cdot n da \tag{E.25}$$

$$\frac{d}{dt}\int_{\mathscr{R}_t} a\, dv = \int_{\mathscr{R}_t} (\dot{a} + a\, \text{tr}\, L) dv \tag{E.26}$$

IMAGE EVALUATION
TEST TARGET (QA–3)

1.0

1.1

1.25

1.4

1.6

1.8

2.0

2.2

2.5

2.8

3.2

3.6

4.0

← 150mm →

← 6″ →
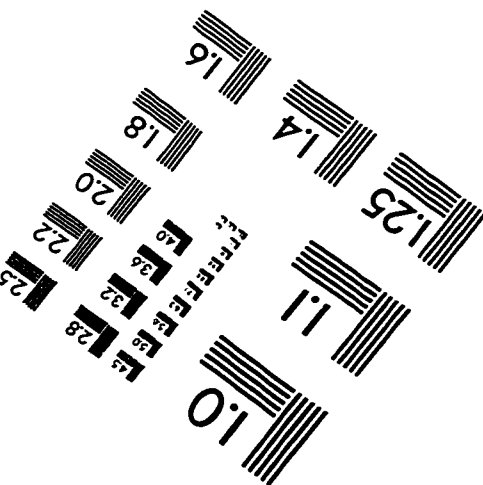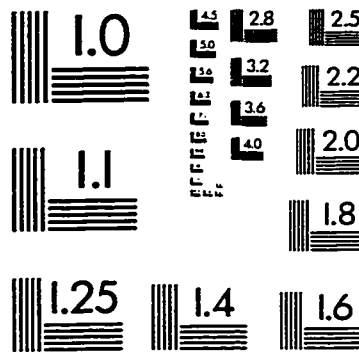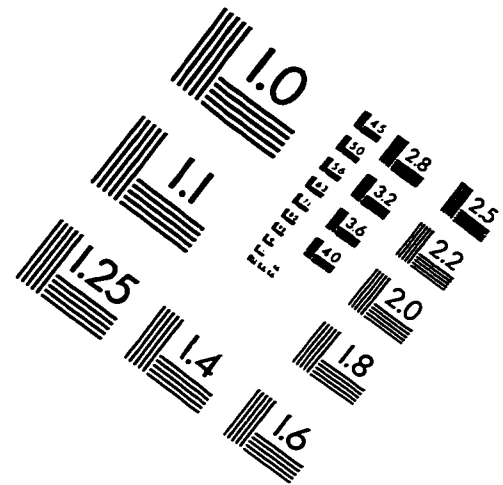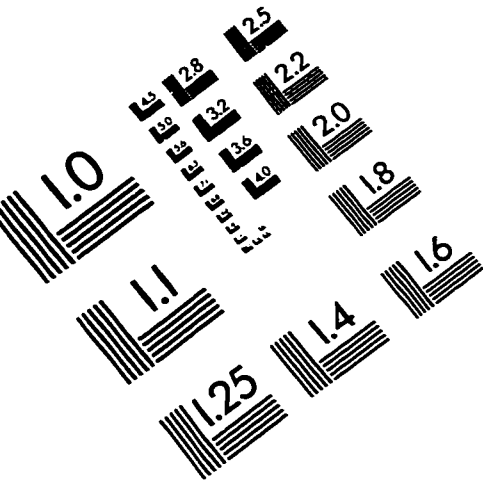
APPLIED IMAGE, Inc
1653 East Main Street
Rochester, NY 14609 USA
Phone: 716/482-0300
Fax: 716/288-5989